

AD-A267 757



The Pennsylvania State University
APPLIED RESEARCH LABORATORY
P.O. Box 30
State College, PA 16804

DTIC
ELECTE
AUG 1 1 1993
S C D

TRANSITION INDUCED BY FIXED AND
FREELY CONVECTING SPHERICAL PARTICLES
IN LAMINAR BOUNDARY LAYERS

by

H. L. Petrie
P. J. Morris
A. R. Bajwa
D. C. Vincent

Technical Report No. TR 93-07
August 1993

Supported by:
Office of Naval Research

L.R. Hettche, Director
Applied Research Laboratory

Approved for public release; distribution unlimited

391
207
93-18446



93 8 6 127

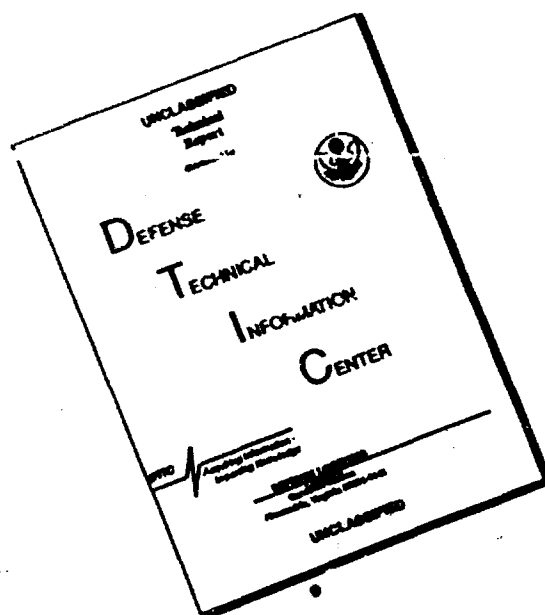
REPORT DOCUMENTATION PAGE

Form Approved
OMB No. 0704-0188

Public reporting burden for this collection of information is estimated to average 1 hour per response, including the time for reviewing instructions, searching existing data sources, gathering and maintaining the data needed, and completing and reviewing the collection of information. Send comments regarding this burden estimate or any other aspect of this collection of information, including suggestions for reducing the burden, to Washington Headquarters Service, Directorate for Information Operations and Reports, 1215 Jefferson Davis Highway, Suite 1204, Arlington, VA 22202-4302, and to the Office of Management and Budget, Paperwork Reduction Project (0704-0188), Washington, DC 20503.

1. AGENCY USE ONLY (Leave blank)		2. REPORT DATE 25 May 1993		3. REPORT TYPE AND DATES COVERED Final Technical Report	
4. TITLE AND SUBTITLE Transition Induced by Fixed and Freely Convecting Spherical Particles in Laminar Boundary Layers				5. FUNDING NUMBERS G-N00014-91-J-1646	
6. AUTHOR(S) H. L. Petrie, P. J. Morris, A. R. Bajwa, D. C. Vincent					
7. PERFORMING ORGANIZATION NAME(S) AND ADDRESS(ES) Applied Research Laboratory The Pennsylvania State University P.O. Box 30 State College, PA 16804				8. PERFORMING ORGANIZATION REPORT NUMBER TR#93-07	
9. SPONSORING / MONITORING AGENCY NAME(S) AND ADDRESS(ES) Office of Naval Research 800 North Quincy Street Arlington, VA 22217-5000				10. SPONSORING / MONITORING AGENCY REPORT NUMBER	
11. SUPPLEMENTARY NOTES					
12a. DISTRIBUTION / AVAILABILITY STATEMENT Approved for public release; distribution unlimited				12b. DISTRIBUTION CODE	
13. ABSTRACT (Maximum 200 words) An experimental and analytical study of aspects of transition induced by disturbances from spherical particles in laminar boundary layers is discussed. The generation of turbulent wedges by fixed spherical particles in a laminar boundary layer on or near the surface of a flat plate is considered experimentally using flow visualization with fluorescent dye and laser Doppler velocimetry. Turbulent spots generated by freely convecting spherical particles that are released in the freestream to fall into a flat plate laminar boundary layer and impact the plate are also discussed. A combination of dye flow visualization and a video based particle tracking technique was used to study the convecting particle problem. Although the Reynolds number at the critical condition for turbulent wedge generation by fixed particles and turbulent spot generation by convecting particles are similar, transition in these two situations appears to be fundamentally different. The development of a turbulent wedge near the critical condition is a relatively gradual process. In contrast, turbulent spots form relatively quickly after the convecting particles enter the boundary layer and impact the plate. Turbulent wedge formation downstream of a fixed particle results from the destabilization of the near wall flow by the vortical structures shed into particle wake. This shedding process is dominated by periodically shed loop shaped hairpin vortices. Observation of subharmonic oscillations at $\frac{1}{2}$ and $\frac{1}{4}$ of this shedding frequency suggest that a chaotic route to turbulence by a series of period doubling bifurcations is possible. Convecting particle wakes have little, if any, affect on turbulent spot generation. The disturbances to the flow near the wall due to the particle impact rapidly develop and spots begin to emerge at the particle in all cases. The analysis first predicts the trajectories of the convecting particles. The development of wave packets from disturbances at different locations is considered. For fixed or convecting particles, the stability of the particle wakes in a laminar boundary layer was analyzed with consideration given to the wake position, width and the velocity deficit. This provides the initial conditions for the development of a wave packet generated by a particle in a boundary layer. The development of the wave packets generated by the particles is then performed. This report describes the first items in the analysis and the remainder are presented in a doctoral thesis.					
14. SUBJECT TERMS laminar boundary layer, spherical particle, transition, turbulent wedges, flow visualization, experiment, turbulent spots hairpin vortices,				15. NUMBER OF PAGES 108	
				16. PRICE CODE	
17. SECURITY CLASSIFICATION OF REPORT Unclassified	18. SECURITY CLASSIFICATION OF THIS PAGE Unclassified	19. SECURITY CLASSIFICATION OF ABSTRACT Unclassified	20. LIMITATION OF ABSTRACT SAR		

DISCLAIMER NOTICE



THIS DOCUMENT IS BEST
QUALITY AVAILABLE. THE COPY
FURNISHED TO DTIC CONTAINED
A SIGNIFICANT NUMBER OF
PAGES WHICH DO NOT
REPRODUCE LEGIBLY.

Abstract

An experimental and analytical study of aspects of transition induced by disturbances from spherical particles in laminar boundary layers is discussed. The generation of turbulent wedges by fixed spherical particles in a laminar boundary layer on or near the surface of a flat plate is considered experimentally using flow visualization with fluorescent dye and laser Doppler velocimetry. Turbulent spots generated by freely convecting spherical particles that are released in the freestream to fall into a flat plate laminar boundary layer and impact the plate are also discussed. A combination of dye flow visualization and a video based particle tracking technique was used to study the convecting particle problem. Although the Reynolds number at the critical condition for turbulent wedge generation by fixed particles and turbulent spot generation by convecting particles are similar, transition in these two situations appears to be fundamentally different. The development of a turbulent wedge near the critical condition is a relatively gradual process. In contrast, turbulent spots form relatively quickly after the convecting particles enter the boundary layer and impact the plate. Turbulent wedge formation downstream of a fixed particle results from the destabilization of the near wall flow by the vortical structures shed into particle wake. This shedding process is dominated by periodically shed loop shaped hairpin vortices. Observation of subharmonic oscillations at $\frac{1}{2}$ and $\frac{1}{4}$ of this shedding frequency suggest that a chaotic route to turbulence by a series of period doubling bifurcations is possible. Convecting particle wakes have little, if any, affect on turbulent spot generation. The disturbances to the flow near the wall due to the particle impact rapidly develop and spots begin to emerge at the particle in all cases.

The analysis first predicts the trajectories of the convecting particles. The development of wave packets from disturbances at different locations is considered. For fixed or convecting particles, the stability of the particle wakes in a laminar boundary layer was analyzed with consideration given to the wake position, width and the velocity deficit. This provides the initial conditions for the development of a wave packet generated by a particle in a boundary layer. The development of the wave packets generated by the particles is then performed. This report describes the first items in the analysis and the remainder are presented in a doctoral thesis.

DTIC QUALITY INSPECTED 3

Accession For	
NTIS	CRA&I <input checked="" type="checkbox"/>
DTIC	TAB <input type="checkbox"/>
Unannounced <input type="checkbox"/>	
Justification	
By	
Distribution /	
Availability Codes	
Dist	Avail and/or Special
A-1	

Table of Contents

	Page
ABSTRACT	i
LIST OF FIGURES	iv
LIST OF TABLES	vi
PART I: LIST OF PARTICIPANTS, PRESENTATIONS AND PUBLICATIONS	1
Participants	2
Presentations	2
Journal Submissions	2
PART II: PARTICLE INDUCED TRANSITION EXPERIMENTS	3
Chapter 1. Transition Induced by a Fixed Spherical Particle in a Laminar Boundary Layer	4
1.1 Introduction	4
1.2 Objective	7
1.3 Experimental Apparatus and Approach	7
1.4 Results	9
1.4.1 Flow Visualization with a Surface Mounted Sphere	10
1.4.2 Flow Visualization with an Elevated Sphere	12
1.4.3 Horseshoe Vortex Velocity Profiles	15
1.4.4 Mean Velocity Profile Evolution in the Wakes	16
1.4.5 Velocity Fluctuation Intensity Profiles	17
1.4.6 Hairpin Vortex Shedding Frequencies	20
1.5 Summary and Conclusions	21
1.6 References	23
Chapter 2. Turbulent Spot Formation by Freely Convecting Spherical Particles in a Laminar Boundary Layer	38
2.1 Introduction	38
2.2 Objectives	40
2.3 Experimental apparatus and Procedures	40
2.4 Results	42

Table of Contents (Cont.)

	Page
2.4.1 Flow Visualzation Results	42
2.4.2 Impact Conditions	46
2.4.3 Conditions Generating Turbulent Spots	47
2.4.4 Pathline and Velocity History Data	50
2.5 Summary and Conclusions	55
2.6 References	57
PART III: PARTICLE TRAJECTORY AND TRANSITION ANALYSIS	67
3.1 Introduction	68
3.2 Particle Trajectory Calculations	69
3.2.1 Second-Order Boundary Layer Theory	70
3.2.2 Trajectory Calculations	71
3.2.3 Lift and Drag Terms	72
3.2.4 The Basset Term	73
3.3 Development of Wave Packets in a Laminar Boundary Layer	75
3.4 Numerical Simulation of Wave Packets	82
3.4.1 Initial Disturbance Due to a Particle	89
3.4.2 Further Work	90
3.5 Stability of a Wake in a Boundary Layer	90
3.5.1 Background	91
3.5.2 Governing Equations	92
3.5.3 Method of Solution	94
3.5.4 Results and Discussion	94
3.5.4.1 Wake Velocity Defect	94
3.5.4.2 Wake Width	97
3.5.4.3 Wake Height in the Boundary Layer	97
3.5.4.4 Viscous Effects	98
3.5.5 Future Work	100
3.5.6 Conclusions	100
3.6 References	100

List of Figures

Figure	Page
1.1 Diagram of open channel with test plate installed	25
1.2 Mean velocity profiles in undisturbed boundary layer compared with the Blasius profile	26
1.3 Side views of surface mounted sphere wake, $Re_d = 810$, $d/\delta = 0.55$;	
(a) $X = 0 - 80$	27
(b) $X = 64 - 130$	27
(c) $X = 176 - 215$	28
(d) $X = 361 - 410$	28
1.4 Side views of elevated particle wake, $Re_d = 690$, $k/\delta = 0.74$, and $d/\delta = 0.41$;	
(a) $X = 0 - 65$	29
(b) $X = 107 - 150$	29
(c) $X = 172 - 215$	30
(d) $X = 306 - 339$	30
1.5 Velocity fluctuation intensities upstream of surface mounted sphere, $X = -1.01$, $Re_d = 700$, $U = 23.3$ cm/s, $d/\delta = 0.46$	31
1.6 Mean velocity profiles in the surface mounted sphere wake	32
1.7 Mean velocity profiles in the wake of the elevated sphere	32
1.8 Shape factor, $H = \delta^*/\theta$, for a subcritical surface mounted sphere and the surface mounted and elevated cases of interest	33
1.9 Comparison of mean profiles in inner variables with Spalding's (196) law of the wall	33
1.10 Comparison of the surface mounted sphere wake mean velocity profile at $X = 240$ with turbulent boundary layer data from Purtell, et al. (1981)	34
1.11 Turbulence intensity profiles in the wake of the surface mounted sphere . . .	35
1.12 Turbulence intensity profiles in the wake of the elevated sphere	35
1.13 Hairpin vortex shedding frequency Strouhal numbers versus Reynolds number	36

List of Figures (Cont.)

Figure	Page
2.1 Flow visualization of $d = 5.56$ mm diameter polystyrene particle generated events;	
(a) $t = 0$ s	58
(b) $t = 0.66$ s	58
(c) $t = 1.33$ s	59
(d) $t = 2.0$ s	59
2.2 Impact of a subcritical $d = 3.97$ mm diameter polystyrene sphere;	
(a) $t = 0$ s	60
(b) $t = 1$ s	60
(c) $t = 2$ s	60
2.3 Events generated by impact of $d = 6.35$ mm diameter polystyrene particle at;	
(a) $t = 0$ s	61
(b) $t = 0.66$ s	61
(c) $t = 1.33$ s	61
2.4 Vertical impact velocity versus Reynolds number	62
2.5 Two component impact velocity magnitude, U_{∞} , versus Reynolds number . .	62
2.6 Estimated critical conditions for turbulent spot generation on a heated laminar flow control body at three heating conditions from Lauchle, et al. (1986)	63
2.7 Trajectories for particles #5, 7, and 9 on table 2.1	64
2.8 Velocity history for particle #5 on table 2.1, nylon with $d = 3.94$ mm	64
2.9 Velocity history of particle #7 on table 2.1, delrin $d = 7.89$ mm	65
2.10 Velocity history for particle #9 on table 2.1, delrin $d = 5.51$ mm	65
3.1 Lift and drag force vectors on a particle	73
3.2 Lift force on a particle ude to shear	76
3.3 Trajectories of particles with different specific gravities released form rest	77
3.4 Trajectories of particles with different sizes released from rest	78

List of Figures (Cont.)

Figure	Page
3.5 Time variation of the vertical velocity of particles with different specific gravities	79
3.6 Time variation of vertical velocity of particles with different sizes	80
3.7 Contours of initial vertical velocity in the xy-plane at $z = 0$	85
3.8 Contours of the vertical velocity in the xy-plane at $z = 0$ at time $t = 25$	86
3.9 Contours of the vertical velocity in the xz-plane at $y = 1.478$ at time $t = 25$	87
3.10 Contours of the vertical velocity in the xy-plane at $z = 0$ at time $t = 50$	88
3.11 Contours of the vertical velocity in the xz-plane at $y = 1.478$ at time $t = 50$	89
3.12 Mean velocity profiles	96
3.13 Variation of growth rates with change in wake-width in a boundary layer with $u_w = 0.5$, $y_w = 2.4$	97
3.14 Variation of growth rates with change in wake-height in a boundary layer with $u_w = 0.5$, $a_w = 3.243$	98
3.15 Variation of growth rates with change in wake-velocity defect in a hyperbolic tangent shear layer with $a_w = 3.243$ and $\beta = 1.0$ and 9.0	99

List of Tables

Table	Page
1.1 Observations based on the surface mounted sphere flow visualizations	37
1.2 Observations based on the elevated sphere flow visualizations	37
2.1 Impact conditions for all cases considered	66

PART I

List of Participants, Presentations and Publications

Participants:

Co-Principal Investigators:

Dr. P. J. Morris, Professor
233 Hammond Building
Aerospace Engineering Department
The Pennsylvania State University
University Park, PA

Dr. Howard L. Petrie, Senior Research Associate
P. O. Box 30
Applied Research Laboratory
The Pennsylvania State University
State College, PA 16804

Graduate Student Research Assistants:

A. R. Bajwa, Ph. D. candidate
Aerospace Engineering Department
The Pennsylvania State University
December 1993 degree date anticipated

D. C. Vincent, M. S. candidate
Aerospace Engineering Department
The Pennsylvania State University
December 1993 degree date anticipated

Presentations:

A. R. Bajwa and P. J. Morris, "Stability of a Wake Embedded in a Boundary Layer," 45th APS Division of Fluid Dynamics Meeting, Tallahassee, FL, November 22-24, 1992.

A. R. Bajwa and P. J. Morris, "The Stability of a Wake in a Boundary Layer," IMACS International Conference, Bangalore, India, December 7-11, 1992.

D. C. Vincent and H. L. Petrie, "Transition Induced by a Spherical Particle in a Laminar Boundary Layer," AIAA paper 93-2909, To be presented at 24th AIAA Fluid Dynamics Conference, Orlando, FL, July 6-10, 1993.

Journal Submissions:

D. C. Vincent and H. L. Petrie, "Transition Induced by a Fixed Spherical Particle in a Laminar Boundary Layer," Submitted to AIAA Journal.

D. C. Vincent and H. L. Petrie, "Turbulent Spot Generation by Freely Convecting Spherical Particles," To be submitted to AIAA Journal.

PART II

Particle Induced Transition Experiments

Chapter 1

Transition Induced by a Fixed Spherical Particle in a Laminar Boundary Layer

Abstract: The development of the wake of a fixed spherical particle mounted on the surface or elevated above the surface in a laminar boundary layer and the resultant downstream formation of a turbulent wedge has been studied experimentally. Hairpin vortices are shed periodically into the wakes of these particles in all critical cases and a horseshoe vortex is established when the particle is sufficiently close to the surface. Elevated particle wake data indicate the horseshoe vortex does not have a significant effect on turbulent wedge formation. The legs of the hairpin vortices play a significant role in the breakdown of the flow. Periodicity develops in these wakes at $\frac{1}{2}$ and $\frac{1}{4}$ of the hairpin vortex shedding frequency and a chaotic route to turbulence by a cascade of period doubling bifurcations is possible.

1.1 Introduction

Boundary layer transition from laminar to turbulent flow is an important aspect of fluid dynamics in numerous engineering applications. Natural transition in laminar boundary layers involves the selective amplification of small disturbances leading to the development of two dimensional instability waves. Secondary instabilities and three dimensionality develops and the flow rapidly breaks down and becomes turbulent. Alternate routes to turbulence involving bypass transition are possible. Bypass transition includes transition processes that bypass the 2D stage of natural transition and, typically, involves disturbances that are initially larger and more three dimensional than in the case of natural transition. Laminar flow control is an attractive technology for reducing skin friction and flow noise. Laminar flow can be maintained to unnaturally large Reynolds numbers by a variety of methods such as surface suction, surface heating (in liquids), and body shaping. The degradation of laminar flow control performance by sources of disturbance in the operating environment often involves bypass transition and defeats this technology.

Lauchle, et al., (1986) evaluated how sized particles seeded into the freestream degraded

the performance of a laminar flow control heated body in a water tunnel. Transition Reynolds numbers as large as 37×10^6 were achieved in a clean flow. However, freestream particles decreased the transition Reynolds number substantially. No minimum particle diameter threshold for performance degradation was observed but larger particles had a more substantial effect. In a similar heated body laminar flow control experiment examining particle degradation of performance by Ladd and Hendricks(1985), the estimated critical particle diameter Reynolds numbers based on the velocity in the undisturbed flow one particle diameter above the surface at the location turbulent spots were observed corresponds approximately to values reported of the critical Reynolds number by Hall(1967) for fixed spherical particles in laminar pipe flow. It was speculated by Ladd and Hendricks(1985) that the particles impact the body and momentarily stick.

Hall(1967) used flow visualization to establish conditions resulting in turbulent wedge formation downstream of a fixed spherical particle mounted on or near the wall in a developing laminar pipe flow. When a particle was positioned near the wall, the effective diameter was the distance from the wall to the top of the particle, k . The critical Reynolds number, $Re_{d, crit}$, varied from 585 to 665 for these near surface cases. The particle diameter Reynolds number is based on the velocity at the top of the particle in the undisturbed flow throughout this chapter of the report. Hall(1967) cited the data of Magarvey and Bishop(1961) to support the hypothesis that the shear layer shed from these fixed spheres is turbulent at the critical condition and this turbulence seeds a critical region of the boundary layer below $y/\delta = 0.4$ to cause the formation of a turbulent wedge. Magarvey and Bishop(1961) observed transition occurs at $Re_d \approx 600$ in the wake of a sphere in a uniform freestream. However, these results differ with other work cited in a survey of sphere wake data by Sakamoto and Haniu(1990).

Sakamoto and Haniu(1990) describe the intricate evolution of the wake of a sphere in a

uniform flow with increasing Reynolds number. Periodic shedding of hairpin vortices begins at $Re_d = 300 - 400$. The heads of these hairpin vortices are open round loops and not tight hairpins. This is the case for all of the vortices described as hairpins below. The vortex shedding orientation is random but remains fixed at these low Re_d . Irregularity of the shedding frequency and side to side motion of the hairpin vortices occurs intermittently for $420 < Re_d < 480$. As Re_d is increased above $Re_d = 480$, irregular periodic shedding and slow irregular rotation of the shedding orientation is observed. Above $Re_d = 650$, the Strouhal number based on the hairpin vortex shedding frequency drops from 0.21 to 0.19. Above $Re_d = 800$, smaller vortex loops appear in the shear layer shed from the sphere and the shedding frequency Strouhal number bifurcates into an upper and a lower frequency mode. Transition from a laminar to a turbulent wake is said to occur with the bifurcation at $Re_d = 800$.

Mochizuki(1961) studied the flowfield created by spherical particles on the surface in a laminar boundary layer with flow visualization. The structures in the wake were observed over a range of Reynolds numbers. As with Hall(1967), a turbulent wedge formed downstream of the particle when the Re_d reached a critical value and the wedge moved to the sphere as the Reynolds number was increased. The critical Reynolds increased from approximately $Re_{d\text{ crit}} = 670$ to 1000 as the Reynolds number based on the distance of the particle from the leading edge, Re_l , and freestream velocity was decreased from 220,000 to below 50,000. Based on these data and Hall's(1967) data, the dependence of $Re_{d\text{ crit}}$ on Re_l is small above $Re_l \approx 100,000$. It was speculated that the hairpin vortex heads do not affect turbulent wedge formation and that the horseshoe vortex formed by the flow separation upstream of the sphere and the legs of the hairpin vortices play a key role in the transition process.

Acarlar and Smith(1987) and Klebanoff, Cleveland, and Tidstrom(1992) examined the wake of a hemispherical bump in a flat plate laminar boundary layer. The interaction between

the horseshoe and hairpin vortices and between successive hairpin vortices was believed lead to the development of secondary vortices and, subsequently, to turbulent wedge formation.

1.2 Objective

Quantitative information in the wakes of surface mounted spheres and hemispheres that generate a turbulent wedge is limited and the mechanisms leading to development of a turbulent wedge are poorly understood. The case of a fixed elevated sphere in a laminar boundary layer has hardly been considered. The objective of the present fixed spherical particle study was to investigate the evolution of the wakes of fixed spherical particles on or near the surface in a laminar boundary layer for subcritical to supercritical conditions to gain a greater understanding of the details of these wake flows and the processes leading to formation of a turbulent wedge. Another objective of these fixed particle turbulent wedge data deals comparison to the convecting particle results in Chapter 2 of this report. It was desired to determine whether these phenomena of turbulent wedge and spot formation by spherical particles appears to be fundamentally the same or whether they are distinctly different. This last point is discussed in Chapter 2.

1.3 Experimental Apparatus and Approach

Experiments were conducted in a low speed closed loop open channel. The laminar boundary layer developed on a flat plate mounted above the floor of this channel was used for this transition study. Figure 1.1 is diagram of the channel and of the test plate. The plenum of the channel is supplied through a diffuser containing series of 7 perforated plates which aid in breaking up large structures. This is followed by a 15 cm thick section of 3.2 mm cell size honeycomb and the 1:5.88 contraction nozzle. The flat plate leading edge was a 12:1 ellipse. The channel test section dimensions are a 75.9 cm span and a 3.66 m length with a 50 cm depth. The plate span is 2cm less than the channel span with a 1 cm gap at the sidewalls. This sidewall gap could be adjusted with movable slats at the bottom of the plate to affect a bleed with which

sidewall contamination effects might be controlled. These slats were set so that the gaps were closed for the present study. Observations were limited to the upstream portion of the test section to avoid sidewall contamination. The sidewalls of the test section were glass for optical access.

Flow visualization was achieved by seeping a concentrated solution of fluorescein disodium salt, a fluorescent dye, into the flow. Walker(1987) provides details about the performance of the fluorescein. An inclined slit in the surface of the plate located upstream of the fixed particle location and a strategically placed wand located in the plenum were used to add the dye to the flow. Two ultraviolet 'black' lights emitted enough radiation in the range of the absorption spectrum of the dye, which peaks at 490 nm wavelength, to produce fluorescence effectively without lighting up the background or the plate surface. The flow visualizations were videotaped for later analysis.

Velocity profile measurements were made with a one component Helium-Neon laser based fringe mode forward scatter LDV system with frequency shift in one of the two laser beams. A TSI model 1980b digital frequency counter and a PC computer were used to process the Doppler signals and sample LDV data. Vincent(1993) provides further details about the instrumentation and the facility.

Velocity profiles of the streamwise component were measured on the centerplane upstream of a surface mounted particle in the horseshoe vortex system that forms when the approach flow separates. The wakes of surface mounted and elevated particles were surveyed from $X = 1$ to as far as $X = 240$ radii downstream of the particle. X is the streamwise distance from the particle normalized with the particle radius. Y is the vertical distance from the plate similarly normalized with the particle radius. Near critical cases generating a turbulent wedge were emphasized and representative cases are discussed herein. Multiple sets of LDV data were taken for estimating velocity fluctuation power spectra using the Discretized Lag Product method

discussed by Mayo, et al.(1974). Surveys in the wakes of spheres in the uniform freestream were made for comparison purposes. Vincent(1993) presents additional velocity survey data not included in this report. This includes limited vertical component profiles and Reynolds shear stress profiles.

Spherical particles were mounted in position on or above the surface at $x = 0.838$ m downstream of the leading edge of the test plate using 0.25 mm diameter wire. The wire extended from the plate to the particle when the particles were on or near the surface. This was the case for the two cases detailed in this Chapter and the wire alone was not shedding a vortex street due to the low local Reynolds number. The wire extended through the particle to a support above the free surface for particles further from the surface. A Questar QM1 long range microscope with a graduated reticle eyepiece and a translation stage with a 0.025 mm position readout was used to evaluate the position of the particles relative to the wall.

1.4 Results

Figure 1.2 compares the measured mean velocity profiles on the centerline of the channel to the Blasius profile for the freestream velocities used of the cases detailed in the discussion below. The 99% thickness is denoted as δ and y is the distance from the surface. There is a slight favorable pressure gradient in the channel due to an inclined flap at the trailing edge of the test plate and a section of honeycomb above the working surface at the exit of the test section. The tail flap and honeycomb created a slight negative angle of attack at the nose of the test plate to avoid unsteady separation on the working surface. The freestream turbulence intensity measured by the LDV system was 0.39%. The actual intensity is probably less since the He-Ne based LDV signals processed by a digital counter are expected to be noisy relative to, say, a hot-wire.

1.4.1 Flow Visualization with a Surface Mounted Sphere

A particle sufficiently near the surface separates the approach flow and a horseshoe vortex system is formed. The horseshoe vortex wraps around the particle and the legs of the vortex form two streamwise oriented counter-rotating vortices that extend downstream into the wake of the particle. When dye is seeped into the flow at the wall upstream of the particle, the separation line at the edge of the horseshoe vortex is well defined because none of the surface injected dye is entrained past this separation line into the horseshoe vortex. The dye laden surface flow is not lifted but is diverted spanwise around the horseshoe vortex system. A distinct keyhole shaped dye shadow results and defines the perimeter of the horseshoe vortex well downstream into the wake. The dye on the surface is drawn towards the centerplane of the particle wake slightly downstream of the particle as the flow converges in the region of hairpin vortex formation. Dye seeped into the flow from a wand in the plenum is needed to visualize the horseshoe and hairpin vortices in the wake of the particles.

The present estimates of the critical Reynolds number for surface mounted particles are consistent with the values and trends observed by Mochizuki(1961) and Hall(1967). A continuous turbulent wedge was observed in the present study at $Re_{d \text{ crit}} = 630$ to 700 with $Re_l = 129,000$. $Re_{d \text{ crit}}$ is based on the particle diameter and the velocity at the top of the particle in the undisturbed flow. Mochizuki(1961) observed a wedge forming at $Re_{d \text{ crit}} = 685$ and $Re_l = 122,000$. Defining when a continuous turbulent wedge forms is subject to some personal bias because the wake is irregular appearing before the wedge is clearly present. Below $Re_d = 480$ to 500 , the hairpin vortices do not lift.

Frames of the video recorded flow visualizations were digitized with a frame grabber and contrast enhanced because the images are dim. Figure 1.3 is a series of these images showing side views at successive streamwise positions for a $d = 6.33$ mm diameter sphere on the surface

with $U_\infty = 14.3$ cm/s, $d/\delta \approx 0.55$, $Re_i \approx 129,000$ and $Re_d \approx 810$. A turbulent wedge develops downstream of the sphere for this case. The displacement thickness Reynolds number at the sphere position in the undisturbed flow was $Re_{\delta^*} \approx 540$.

A slight side to side oscillation of the hairpin vortex heads develops in the wake. This cannot be detected in the side views of figure 1.3 but is observed from above the plate. Each successive vortex head moves away from the vertical centerplane in a direction opposite to the adjacent heads. A similar motion is seen in the wakes of spheres in a uniform flow, see Sakamoto and Haniu(1990).

Figure 1.3a shows the region from approximately $X = 0$ to 80. The flow moves from left to right. The hairpin vortices begin forming near $X = 5$ and begins to rise near $X = 10$. The legs of the hairpin vortices descend to near the surface at $X = 25$. The vortex legs draw closely together as they extend to the surface. Depending on the position of filaments of dye, narrow fountains or jets of dye can occasionally be seen lifting vertically between the legs immediately upstream of the vortex heads. The vortex heads are round open loops. Table 1.1 lists the height of the hairpin tops at various streamwise locations and brief observations from the flow visualizations. By $X = 50$, the tops of the heads have lifted past the edge of the boundary layer in the undisturbed flow.

The legs of the hairpin vortices away from the wall are inclined at steeper angles as they move downstream. The inclination of the straight segment of the legs increases from 30° to 35° initially after formation to 45° in figure 1.3a. Fluctuations can be detected near the wall in figure 1.3a after the vortex legs descend to the wall. This development continues in figure 1.3b, $X = 64$ to 130. The fluctuations near the surface where the vortex legs are present are more turbulent appearing in the close-up view further downstream in figure 1.3c, $X = 176$ to 205. Given that the dye filaments retain a history of fluid motions, the flow may not be as irregular as it appears.

However, the velocity profile data presented below support that an increased level of fluctuation is developing near the wall. The hairpin heads appear to separate from the legs of the vortices and begin to look like isolated vorticity rings. The flow becomes increasingly irregular at the wall and the heads of the hairpins appear to have little to do with this irregularity as speculated previously by Mochizuki(1961) and Acarlar and Smith(1987).

Figure 1.3d shows that the third vortex head from the right side is descending towards the surface and a bulge of turbulent appearing fluid is apparent immediately upstream of this downward moving vortex. A definite periodic pattern develops with every fourth hairpin drawn towards the surface.

1.4.2 Flow Visualization with an Elevated Sphere

Moving the sphere away from the surface results in a wake flow that develops with the same general features as the surface mounted case but there are differences. The wall has a stabilizing influence on the hairpin vortices; the vortices are shed with fixed orientation so that the heads lift directly away from the plate and not with a random irregular orientation. For the critical conditions of interest, the hairpins vortices move noticeably from side to side with some slight rotation about an axis through the sphere. This rotation increases and becomes irregular as the distance between the sphere and the surface is increased. The sphere in a uniform flow condition is approached with further elevation of the particle. Also, the horseshoe vortex that forms upstream of the surface mounted particle diminishes in size and strength as the sphere is moved away from the wall until it is no longer evident in the surface flow visualizations. Exactly when the horseshoe vortex system is lost as the particle is elevated was not systematically studied but for the cases considered the vortex diminishes quickly as the gap between the surface and the bottom of the sphere was increased beyond $0.15d$ and the horseshoe vortex is not detected with the flow visualization with gaps larger than $0.25d$ to $0.35d$.

Figure 1.4 shows side views of the wake of a $d = 4.72$ mm diameter sphere located above the plate at the same streamwise position and freestream velocity as the surface mounted case in figure 1.3. $Re_d \approx 690$ for this elevated particle and a continuous turbulent wedge forms near $X = 100$ in the wake. The bottom of the sphere is at $y/\delta = 0.33$ and the top is at $k/\delta = 0.74$ with $d/\delta \approx 0.41$; k is the distance from the wall to the top of the particle. The gap between the bottom of the sphere and the plate was $0.8d$ and the horseshoe vortex could not be detected.

Figure 1.4a shows that the hairpin vortex heads lift away from the surface more quickly than with the surface mounted case. The legs of the hairpin vortices extend to the near the surface at $X = 30$ which is further downstream than the surface mounted case. The hairpin heads grow in size and the inclination of the legs varies further downstream in figure 1.4b. As with the surface mounted case, the legs of the hairpin vortices are inclined at 30° to 35° initially but this angle does not increase quickly to 45° . Well away from the wall, the legs kink and are nearly vertical. The heads of the vortices are further away from the wall than with the surface mounted case considered above and this draws the legs up into a region of low mean shear. Table 1.2 summarizes observations from the flow visualization.

Fluctuations near the wall begin to move away from the surface and some of the hairpin heads move down towards the wall with a repeating pattern; every fourth vortex head in figure 1.4c is slightly lower than the other vortices. Further downstream, the lower frequency periodicity observed with the surface mounted case at $1/4$ the shedding frequency is readily apparent for this elevated particle case. The more obvious appearance of this $1/4$ shedding frequency cycle compared to the surface mounted case may result from the diminution of the stabilizing influence of the wall on wake as the particle is elevated above wall.

Figures 1.4c and 1.4d show that every fourth hairpin deforms and moves towards the wall and turbulent bulges of lifting fluid appear immediately upstream of the descending vortex

heads. Details such as the shape, size, and intensity distribution of the dye in the vortex heads repeats with amazing regularity in the region covered by figure 1.4d. The hairpin heads blend together between the lifting turbulent bulges of fluid and it appears that the outward motion of the bulges is accompanied by an inward rush of fluid that pulls the vortex heads together and towards the surface. The cycle is similar to the cycle of bursting and sweeps observed in the near wall region of a turbulent boundary layer by Corino and Brodkey(1969) but these turbulent bulges are also reminiscent of the low Reynolds numbers turbulent boundary layer flow visualizations by Falco(1977) showing similar coherent motions in the outer flow.

The transition of the wake of cylinders was studied by Karniadakis and Triantafyllou(1992) and Tomboulides, et al.(1992), with a Navier-Stokes equation simulation. Period doubling bifurcations were observed in these simulations after the vortex street develops secondary instabilities. The flow alternates between two preferred states and the limit cycle in phase space branches into two connected cycles. The first period doubling is the result of half wavelength shifts of the spanwise modulation of the flow. A cascade of period doubling bifurcations with increased Re_d occurs and leads, apparently, to a chaotic route to turbulence.

Although the wakes of spheres cannot support a spanwise flow modulation as with a cylinder, the orientation of the hairpin vortex head about the axis of the sphere could be considered as an analogous component or degree of freedom. The side to side rotational motion of the hairpin vortex heads at half the shedding frequency observed in the present flow visualizations is a case of the flow alternating between two preferred states. The regular motion of every forth hairpin vortex head towards the surface could also be another period doubling bifurcation. A rapid breakdown of the flow follows as suggested by the emergence of the turbulent bulges.

1.4.3 Horseshoe Vortex Velocity Profiles

Velocity profiles were measured at 10 streamwise locations upstream of a surface mounted sphere from $X = -1.01$ to -3.56 for $Re_d = 700$ with a particle diameter, $d = 3.91$, a freestream velocity, $U_\infty = 23.3$ cm/s, and $Re_{\delta^*} = 710$ where δ^* is the displacement thickness. The flow visualizations in figure 1.2 used a larger particle and a lower freestream velocity. The conditions used for these velocity profile measurements result in $d/\delta = 0.46$ which nearly matches the elevated particle case in figure 1.4. The Re_d values are nearly matched too. However, Re_{δ^*} is lower for the elevated case, $Re_{\delta^*} \approx 540$.

The intensity of the fluctuations in the horseshoe vortex region upstream of the sphere, based on the freestream velocity, reaches a peak value of 9.2% at $y/k = 0.5$ or $Y = 1$ immediately upstream of the sphere at $X = -1.01$ as shown in figure 1.5 where $k = d$ for this surface mounted case. This measurement location is close to the stagnation point. This intensity peak near $y/k = 0.5$ decreases to under 3% at $X = -1.26$. These fluctuations probably result from the periodic shedding and not a horseshoe vortex oscillation. The dye flow visualizations show that the incoming flow is divided and drawn into the horseshoe vortex for $y/k < 0.5$ or passes around the sphere for $y/k > 0.5$ similar to the findings of Mochizuki⁷. Therefore, the largest expected horseshoe vortex diameter is comparable to the radius of the sphere.

The velocity fluctuation intensity normalized with U_∞ increases near the surface in the profile at $X = -1.01$ in figure 1.5. This near wall peak in fluctuation intensity increases moving upstream away from the sphere with a maximum values from 5% to 5.5% at $X = -1.26$ to -1.51 . By $X = -2.53$, the fluctuation intensities near the surface are similar to the levels near the wall with no particle. Mean reverse flow near the surface was detected as far upstream as $X = -2.02$ with a maximum observed magnitude of $0.06U_\infty$ at $X = -1.51$. This is the general location of maximum fluctuation intensity near the wall.

1.4.4 Mean Velocity Profile Evolution in the Wakes

The development of the wake and turbulent wedge generated by the surface mounted sphere ($d = 3.91$ mm, $U_\infty = 23.3$ cm/s, $Re_d \approx 700$, $d/\delta = 0.46$) was evaluated by measuring velocity profiles on the centerplane at $X = 1.01, 3, 5, 10, 20, 50, 100, 150, 200$, and 240 . Select mean profiles are shown in figure 1.6. Inflections due to the presence of the sphere and hairpin vortices decay and move away from the surface as the profile gradually takes a form similar to a turbulent boundary layer. Figure 1.7 is a similar set of mean profiles for the elevated particle case ($d=4.72$ mm, $U_\infty = 14.3$ cm/s, $Re_d \approx 690$, $y/\delta = 0.41$, $k/\delta = .74$) that was considered in figure 1.4. The dashed lines on the figures indicates the location of the top and the bottom of the sphere. Figures 1.6 and 1.7 show data that are averaged over many vortex shedding periods without regard to the phase of the shedding cycle. As a result, these mean profiles and the profiles discussed below may differ substantially from instantaneous profiles.

The influence of the hairpin vortices and the momentum deficit of the sphere on the velocity profiles is more pronounced for the elevated case in figure 1.7 than the surface mounted case in figure 1.6. The wake of the elevated sphere initially has a local velocity minima near the particle center as is the case for a sphere in the freestream. The hairpin vortices extend further from the surface for the elevated case than the surface mounted case and this influences the velocity profiles further away from the wall and for a greater streamwise distance than the wall mounted case. The elevated sphere profile at $X = 100$ is the solid line on figure 1.7 and exhibits a step near $U/U_\infty = 0.7$. Apparently, during the point by point sequence of data taking during the survey, the turbulent wedge moved from upstream of this location to downstream of it. As a result, the profile is turbulent like below $U/U_\infty = 0.7$ and laminar like at the larger velocity values further from the wall.

Figure 1.8 shows the development of the shape factor, $H = \delta^*/\theta$, for the two cases

considered in figures 1.6 and 1.7 and a subcritical surface mounted particle case that shed hairpins that do not lift. The Blasius value is $H = 2.59$. The shape factor trend is similar to that observed by Schubauer and Klebanoff(1955) for a transitional boundary layer. The elevated sphere wake develops more quickly than the surface mounted case even though Re_d and d/δ are similar for the two cases and Re_{δ^*} is larger for the surface mounted case.

An estimate of the friction velocity, u^* , was made at the most downstream stations using a procedure similar to Chang and Blackwelder(1990). Spalding's law of the wall is fit to the profile data using u^* as the free parameter. Only data near the wall are used to avoid the hairpin distortions to the mean profile away from the wall. The resultant mean profiles are plotted in inner variables where $u^+ = U/u^*$ and $y^+ = yu^*/\nu$. These profiles are compared with Spalding's(1961) law of the wall in figure 1.9. The profiles have a log region and are turbulent-like in most respects. The wake region of the elevated particle boundary layer profile is still appreciably distorted. The surface mounted particle velocity profile at $X = 240$ is replotted in outer variables and compared with a low Reynolds number turbulent profile from Purtell, et al.(1981) in figure 1.10. The data below $y/\delta^* = 3$ suggests the flow is still developing. Considering the periodic structures observed in the flow visualizations in figures 1.3 and 1.4 at these downstream stations, the similarity with turbulent profiles is noteworthy.

1.4.5 Velocity Fluctuation Intensity Profiles

Figures 1.11 and 1.12 show the evolution of freestream velocity normalized turbulence intensity profiles at select locations for the surface mounted and elevated spheres considered in figures 1.6 and 1.7. There are two peaks in the fluctuation intensity profiles beginning at $X = 10$ and continuing downstream until the outer peak is lost. The outer peak corresponds to the heads of the hairpin vortices and moves away from the surface and decays with increasing streamwise distance. This is similar to results for a hemispherical bump wake in Acarlar and

Smith(1987) and Klebanoff, et al.(1992). For the surface mounted case, the inner and outer intensity peaks are about the same at $X = 50$ but this matching of inner and outer intensity peaks is estimated to occur near $X = 25$ to 30 for the elevated particle case. At $X = 100$, both cases still have an outer turbulence intensity peak even though the mean profiles show no obvious feature at $X = 100$. The elevated particle intensity peak is almost twice as far from the wall as the surface mounted case. The outer peak is not distinct at $X = 200$ in either case and is beyond the upper limit of the survey for the elevated particle.

For the surface mounted case, the outer turbulence intensity peak is 30% to 32% at $X = 1$ and 3 and it decreases to 28% and 18 % at $X = 5$ and 10. For the elevated particle case, the outer peak intensities near the particle are slightly larger; 47%, 37%, 24.4%, and 15.6% at $X = 1, 3, 5$, and 10, respectively. Although these intensity levels are high, they meet the 10% to 18% levels mentioned by Morkovin(1969) for self sustaining turbulence, and the mean profiles undergo inflections associated the hairpin heads, the distance of these disturbances from the surface, their frequency and their range of scales are such that instability mechanisms are not directly activated as suggested by their decay.

For comparison purposes, the wakes of spheres in a freestream were surveyed at various Reynolds numbers including $Re_d = 700, 760$, and 1000 at $X = 1, 2, 3, 5, 10$ and 20. The conditions $Re_d = 700, 760$, and 1000 span a range comparable to the near critical cases considered and, therefore, are of some interest. Two distinct intensity peaks due to the shear layer shed from the sphere were observed off the centerline of these freestream spheres at $Re_d = 700$ and above. The intensity levels were 35% to 45% at $X = 1, 2$, and 3 in this Re range. At $X = 5$, the peaks move towards the centerline and decay to levels near 25%. By $X = 10$, the intensity maxima associated with the hairpin vortices are flat across the wake at levels near 12% and this decreases to near 6% at $X = 20$. This flat intensity profile does not occur for the

near surface spheres because the orientation of the shed vortices is fixed. The intensities observed with the surface mounted particle are initially lower than observed with the freestream particles but the decay in the intensities near and just downstream of where the hairpins form, $X = 10$, is less than with the freestream particles. The intensity peaks for the elevated particle associated with the hairpin vortex heads mimic those seen with the freestream particles. In a limited sense, the presence of the wall and boundary layer have little apparent effect on the hairpin vortex heads other than to suppress the randomness of shedding orientation.

The near wall peak in the fluctuation intensity first appears at $X = 10$ for both the surface mounted and the elevated particle cases. This intensity peak slowly grows in vertical extent and level with increasing downstream distance as shown in figures 1.11 and 1.12. The intensities gradually approach turbulent boundary layer levels but the peak does not move to the wall until downstream of $X = 100$ in both cases. This is where the turbulent wedge develops. At $X = 10$, the near wall peak is 8% and is located at $y/d = 0.27$ for the surface mounted case. The level at $X = 10$ for the elevated particle case was 5% and the peak is located at $y/k = 0.25$, approximately. Acarlar and Smith(1987) observe a similar double peaked intensity profile as near as $X = 4$ downstream of a hemispherical bump but the near wall peak is further from the wall relative to the distance to the top of the particle, at $Y = 0.5$.

Activity near the wall upstream of where the near wall turbulence intensity maxima are first detected, $X = 10$, does not appear to be a significant factor. At $X = 1, 3$, and 5 the fluctuation intensity profiles decrease monotonically as the wall is approached for both surface mounted and elevated cases and no features of obvious importance are observed. The fluctuation levels near the wall at these locations are different for the two cases because the elevated particle data near the wall were taken below the particle and outside of the particle wake. However, both cases still develop a fluctuation peak near the wall by $X = 10$ that is not seen at $X = 5$. The

flow visualizations indicate $X = 10$ is about where the hairpin heads have clearly formed and begin lifting but the legs of the vortices still extend back to near the top of the spheres rather than towards the wall. As noted for a hemispherical bump, the hairpins form downstream of a region of flow convergence behind the particles. The circulation induced by the vortex tubes forming the hairpin lifts low speed fluid near the wall and can create periodically varying inflectional velocity profiles. This lifted low speed fluid and the pressure gradients in the hairpin formation region may be key to the emergence of the disturbances at $X = 10$.

The movement of the particle away from the wall weakens the horseshoe vortex and the flow visualizations indicate that the horseshoe vortex was not present for the elevated case considered. Given that the development of the surface mounted and elevated particle wakes near the wall is generally the same, the role of the horseshoe vortex in the wake development and turbulent wedge formation process is probably not significant.

1.4.6 Hairpin Vortex Shedding Frequencies

Velocity fluctuation power spectra were determined for surface mounted spheres on a limited basis. The LDV probe volume was positioned near hairpin vortex head passage locations in an effort to determine the hairpin vortex shedding frequency. The data were taken at $Y = 3$ and 4 and at $X = 20$ and 36 with 3.21 mm and 3.91 mm diameter particles and between $X = 10$ and 16 at $Y = 3$ with a 5.51 mm diameter particle over a range of Reynolds numbers. At the lower Reynolds numbers consider, $Re_d < 800$, the spectra were flat versus frequency, except for narrow spikes due to the shedding frequency. At $X = 20$ and 36 and $Re_d = 1000$ to 1500 , the spectra began to broaden and fill near the shedding frequencies. This suggests the shedding process is becoming more complex or that variations in the interactions between the wake structures occur to cause cycle to cycle phase shifts.

Figure 1.13 plots Strouhal numbers, $St = fd/U_\infty$, of distinct peaks in the spectra of

surface mounted spheres versus Re_d . These data are clustered into linear bands illustrated by the line segments on figure 1.13. The two bands at lower Strouhal values are similar to the high and low frequency shedding modes that appear with a sphere in a uniform flow described in Sakamoto and Haniu(1990). The high frequency mode results are at slightly greater St than for a hemispherical bump where St is based on the radius of the bump in Acarlar and Smith(1987). The two higher frequency bands on figure 1.13 are, apparently, harmonics of the high frequency mode. There are only two data points in the highest frequency band so it is difficult to determine much about these data.

The $\frac{1}{4}$ shedding frequency subharmonic development of turbulent bulges, observed well downstream for the near critical Reynolds number cases considered above, are not detected in figure 1.13 even at higher Re_d . The low Strouhal number band of data is at or near $\frac{1}{2}$ the shedding frequency and may be a subharmonic associated with the side to side motion of the vortex heads. The low frequency shedding mode Strouhal number data in Sakamoto and Haniu(1990) for a sphere in a uniform flow deviate from this type of behavior and are nearly constant with values close to 0.2 in range $600 < Re_d < 2000$.

1.5 Summary and Conclusions

The development of the wakes of surface mounted and elevated particles in a laminar boundary layer was studied using flow visualization and laser Doppler velocimetry. The wake of a surface mounted particle that generated a turbulent wedge developed more gradually than an elevated particle wake at matched conditions. However, the elevated particle wake development was generally similar to the surface mounted particle wake. This suggests that horseshoe vortex that forms with the surface mounted particle does not play a significant role in the wake development and turbulent wedge formation process. A thin layer of irregular fluctuating fluid emerges close to the wall near $X = 10$ for both surface mounted and elevated particle cases.

This X position is where the hairpin vortices have formed and begin lifting fluid away from the surface. This fluctuating layer near the wall grows in the vertical extent of the flow it includes and its intensity level grows with increasing streamwise distance. Eventually the intensity levels approach turbulent boundary layer levels and the fluctuation intensity peak moves to the wall as the turbulent wedge develops. The legs of the hairpin vortices appear to play a role in the development of secondary structures in this layer.

The hairpin vortices shed by the spheres oscillate side to side at one half of the shedding frequency and periodic ejections of turbulent bulges occur further downstream at one quarter of the shedding frequency. These subharmonic motions were more pronounced with the elevated particle case. This may indicate a relaxation of the effects of the wall on the particle wake as the particle is elevated above the surface and may explain the more rapid development of the elevated particle wake. The development of these periodicities at double and quadruple the shedding period suggests that a chaotic route to turbulence by a cascade of period doubling bifurcations is possible.

1.6 References

- Acarlar, M. S., and Smith, C. R., 1987, "A Study of Hairpin Vortices in a Laminar Boundary Layer. Part 1. Hairpin Vortices Generated by a Hemisphere Protuberance," *JFM*, V175, pp. 1-41.
- Chang, S. and Blackwelder, R. F., 1990, "Modification of Large Eddies in Turbulent Boundary Layers," *JFM*, V213, pp. 419-442.
- Corino, E. R. and Brodkey, R. S., 1969, "A Visual Investigation of the Wall Region in Turbulent Flow," *JFM*, V37, pp. 1-30.
- Falco, R. E., 1977, "Coherent Motions in the Outer Region of Turbulent Boundary Layers," *Phys. Fluids Suppl.*, V20, N10, pp. s124-s132.
- Hall, G. R., 1967, "Interaction of the Wake from Bluff Bodies with an Initially Laminar Boundary Layer," *AIAA J*, V5, N8, pp. 1386-1392.
- Karniadakis, G. and Triantafyllou, G. S., 1992, "Three Dimensional Dynamics and Transition to Turbulence in the Wake of Bluff Bodies," *JFM*, V238, pp. 1-30.
- Klebanoff, P. S., Cleveland, W. G., and Tidstrom, K. D., 1992, "On the Evolution of a Turbulent Boundary Layer by a Three-Dimensional Roughness Element," *JFM*, V237, pp. 101-187.
- Ladd, D. M., and Hendricks, E. W., 1985, "The Effect of Background Particulates on the Delayed Transition of a Heated 9:1 Ellipsoid," *Exp. in Fluids*, N3, pp. 113-119.
- Lauchle, G. C., Petrie, H. L., and Stinebring, D. R., 1986, "Effects of Particulates on the Delayed Transition of a Heated Body," Applied Research Laboratory Technical Memorandum 86-213.
- Magarvey, R. H. and Bishop, R. L., 1961, "Wakes in Liquid-Liquid Systems," *Phys. Fluids*, V4, N7, pp. 800-805.
- Mayo, W. T., Shay, M. T., and Riter, S., 1974, "Digital Estimation of Turbulent Power Spectra from Burst Counter LDV Data," *Proc. 2nd Int. Workshop on Laser Anemometry*, Purdue University, pp. 16-24.
- Mochizuki, M., 1961, "Smoke Observation on Boundary Layer Transition Caused by a Spherical Roughness Element," *J. Phys. Soc. of Japan*, V16, N5, pp. 995-1007.
- Morkovin, M. V., 1969, "On the Many Faces of Transition," in *Viscous Drag Reduction*, C. S. Wells, editor, Plenum Press, New York, pp. 1-31.
- Purtell, L. P., Klebanoff, P. S., and Buckley, F. T., 1981, "Turbulent Boundary Layer at Low Reynolds Number," *Phys. Fluids*, V24, N5, pp. 802-811.

- Sakamoto, H., and Haniu H., 1990, "A Study on Vortex Shedding From Spheres in a Uniform Flow," *JFE*, V112, pp. 386-392.
- Schubauer, G. B., and Klebanoff, P. S., 1955, "Contributions on the Mechanics of Boundary Layer Transition," NACA TN 3489.
- Spalding, D. B., 1961, "A Single Formula for the Law of the Wall," *J. Appl. Mech.*, V28, pp. 455-458.
- Tomboulides, A. G., Triantafyllou, G. S., and Karniadakis, G. E., 1992, "A New Mechanism of Period Doubling in Free Shear Flows," *Phys. Fluids A*, V4, N7, pp. 1329-1332.
- Vincent, D. C., 1993, "Transition Induced by Fixed and Freely Suspended Spherical Particles in Laminar Boundary Layers," Masters thesis, Aerospace Engineering Department, The Pennsylvania State University.
- Walker, D. A., 1987, "A Fluorescence Technique of Measurement of Concentration in Mixing Liquids," *J. of Phys. E: Sci. Instr.*, V20, pp. 217-224.

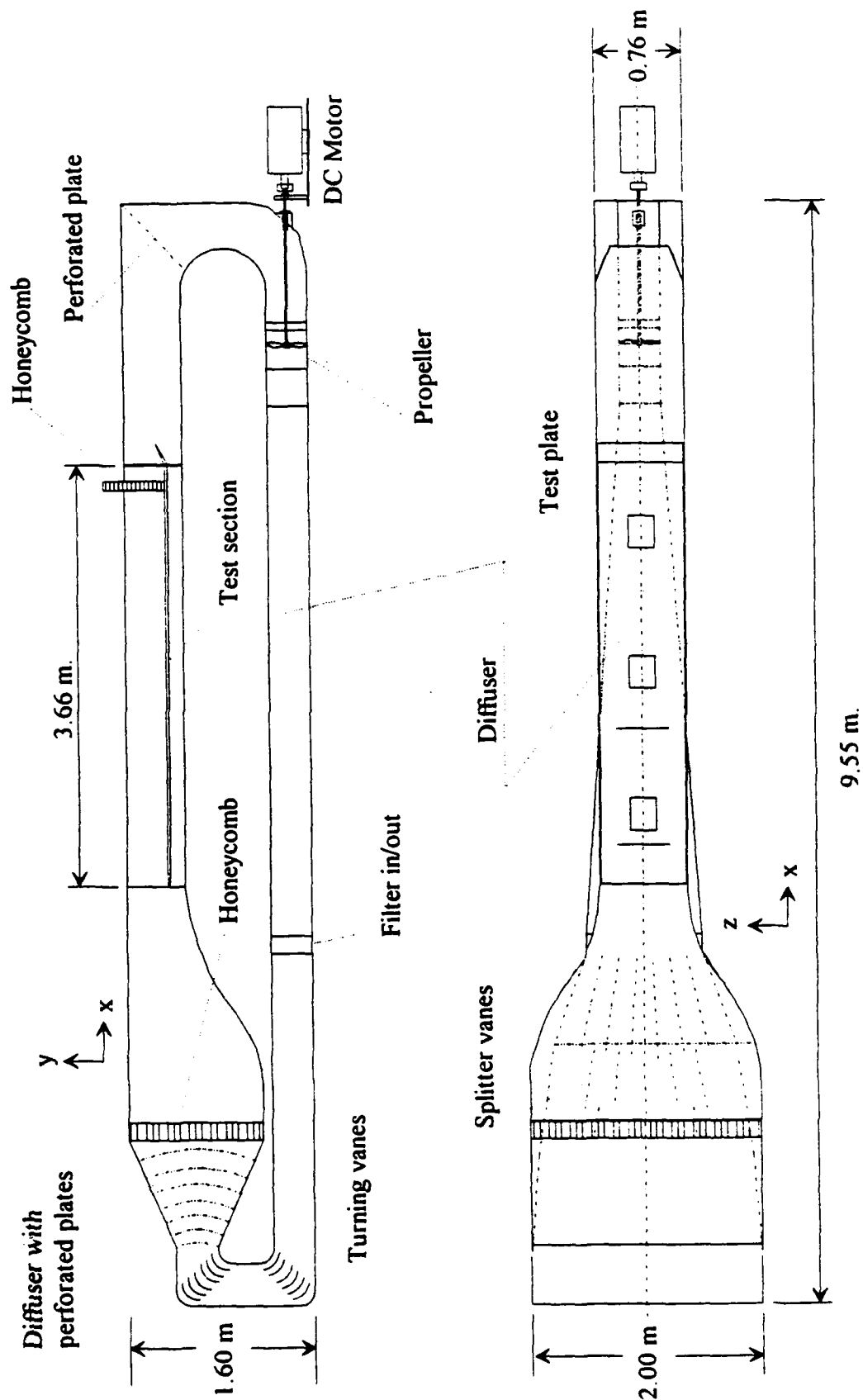


Figure 1.1 Diagram of open channel with test plate installed.

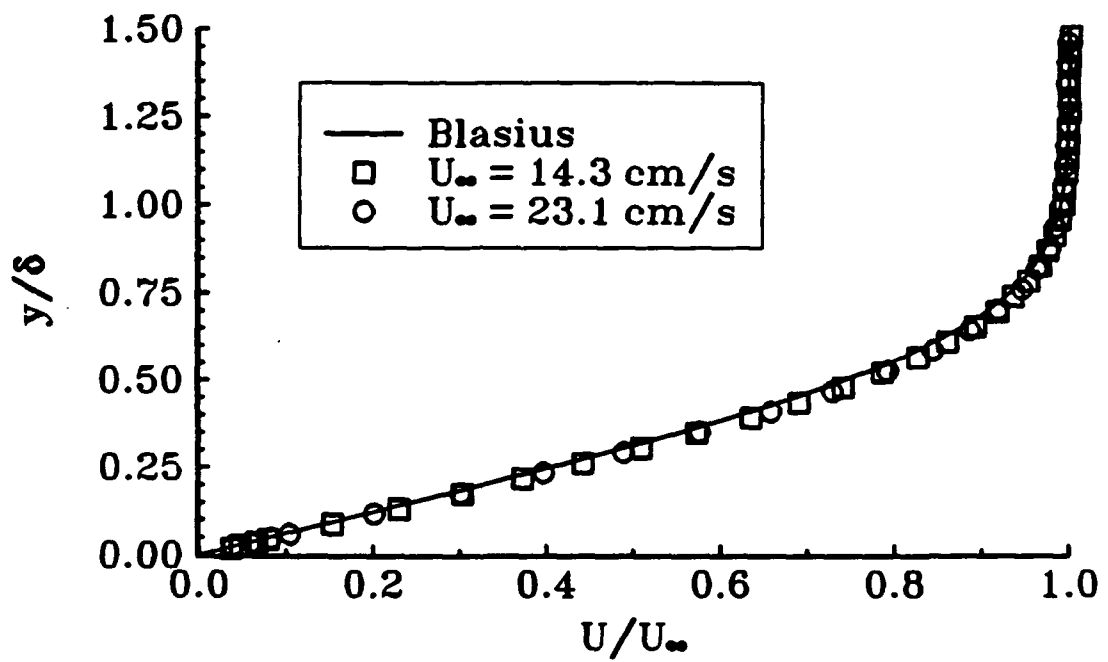


Fig. 1.2 Mean velocity profiles in undisturbed boundary layer compared with the Blasius profile.

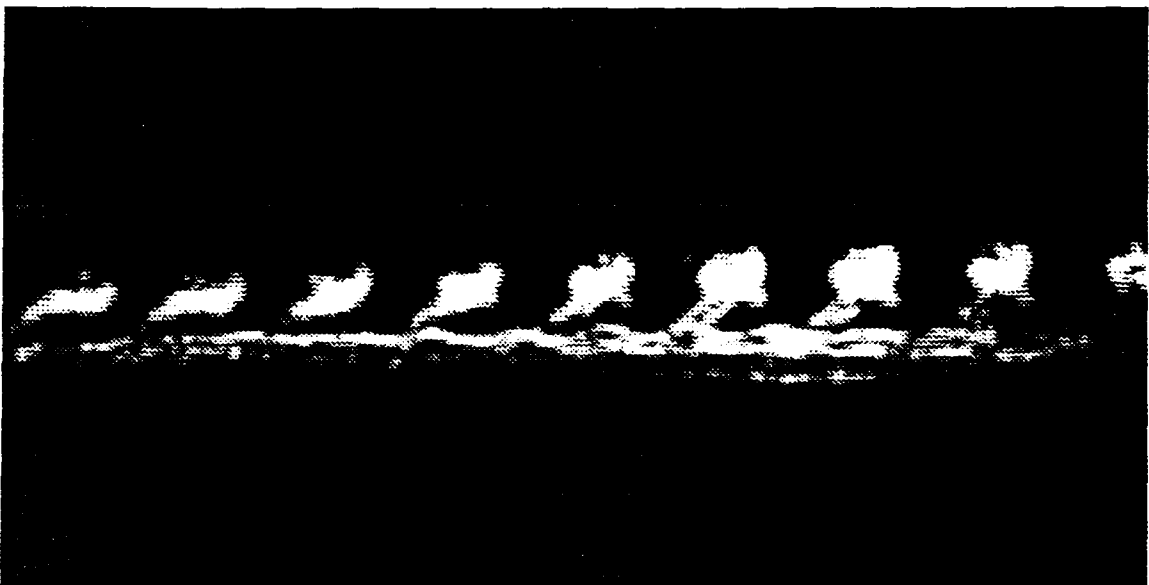


Fig. 1.3 (a) top and (b) bottom. See next page for caption.



Fig. 1.3 (c) top and (d) bottom. Side views of surface mounted sphere wake, $Re_d = 810$, $d/\delta = 0.55$. (a) $X = 0 - 80$, (b) $X = 64 - 130$, (c) $X = 176 - 215$, and (d) $X = 361 - 410$.

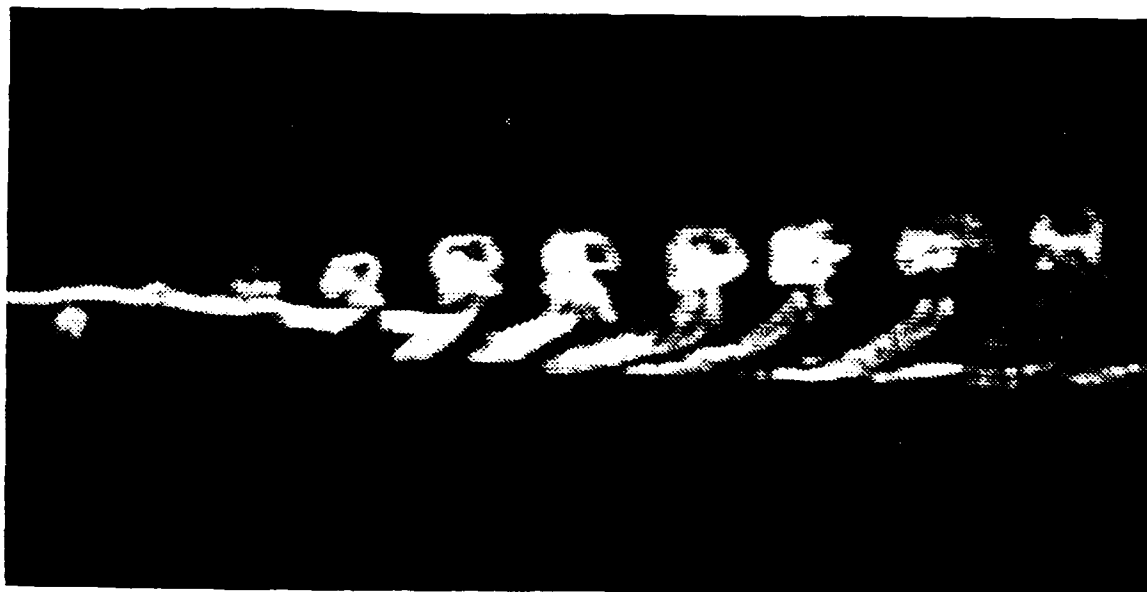


Fig. 1.4 (a) top and (b) bottom. See next page for caption.



Fig. 1.4 Side views of elevated particle wake, $Re_d \approx 690$, $k/\delta = 0.74$, and $d/\delta = 0.41$. (c) top and (d) bottom. (a) $X = 0 - 65$, (b) $X = 107 - 150$, (c) $X = 172 - 215$, (d) $X = 306 - 339$.

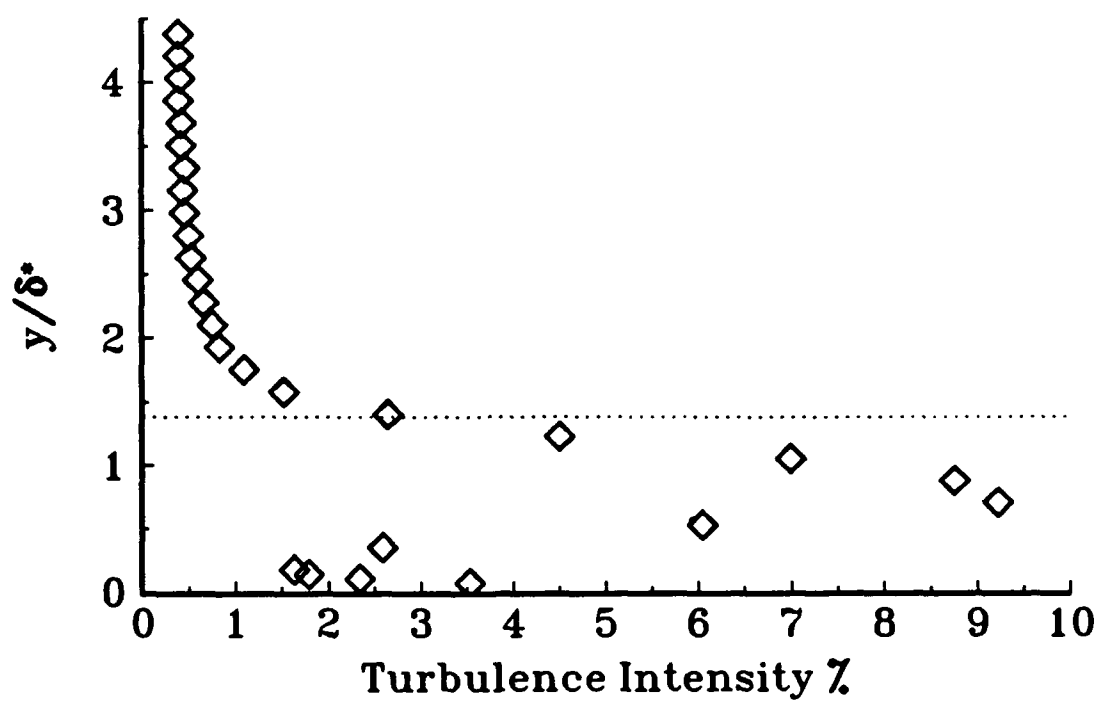


Fig. 1.5 Velocity fluctuation intensities upstream of surface mounted sphere, $X = -1.01$, $Re_d \approx 700$, $U = 23.3$ cm/s, $d/\delta = 0.46$. Dotted line indicates position of top of sphere.

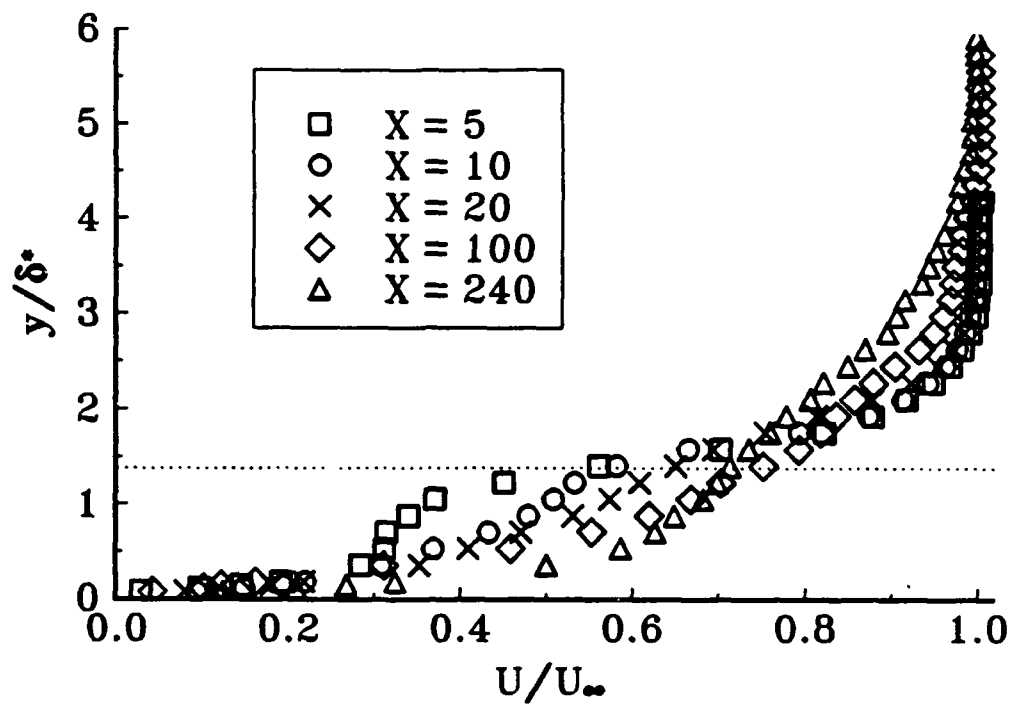


Fig. 1.6 Mean velocity profiles in the surface mounted sphere wake.

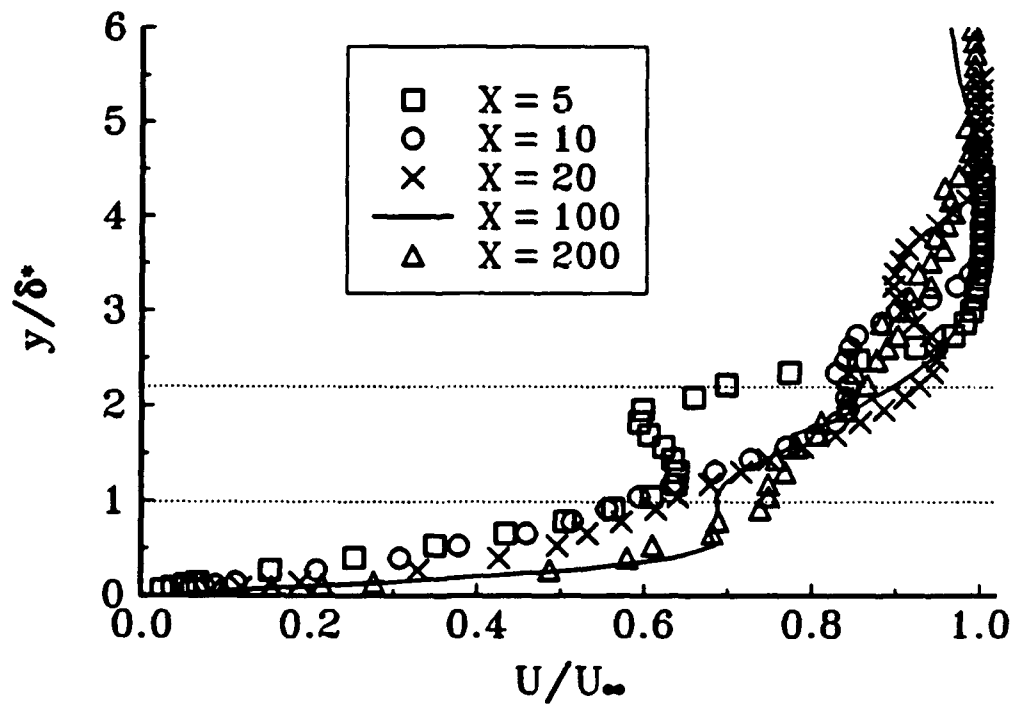


Fig. 1.7 Mean velocity profiles in the wake of the elevated sphere.

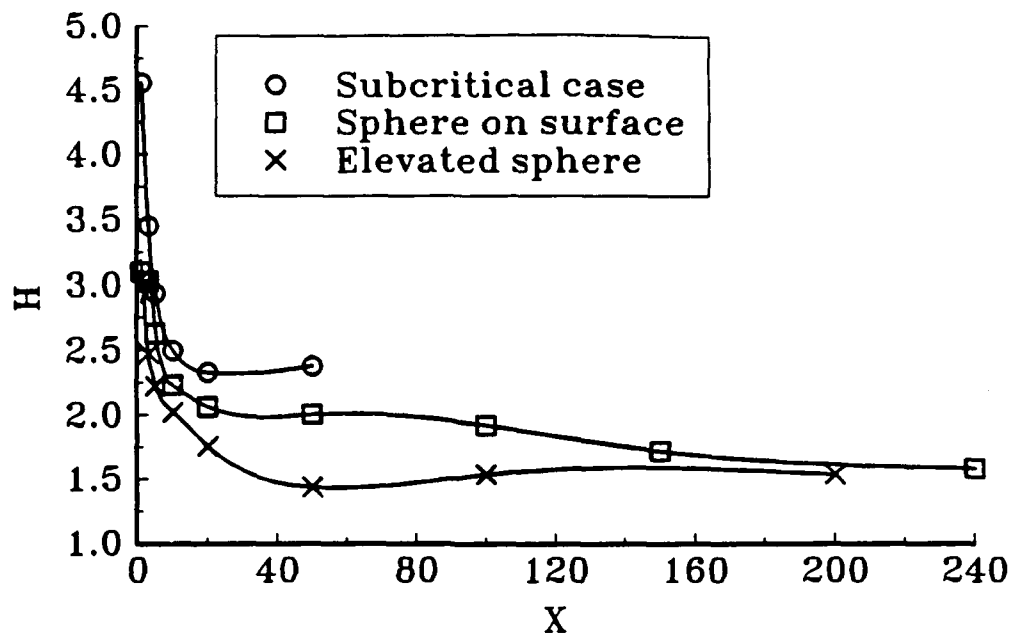


Fig. 1.8 Shape factor, $H = \delta^*/\theta$, for a subcritical surface mounted sphere and the surface mounted and elevated cases of interest.

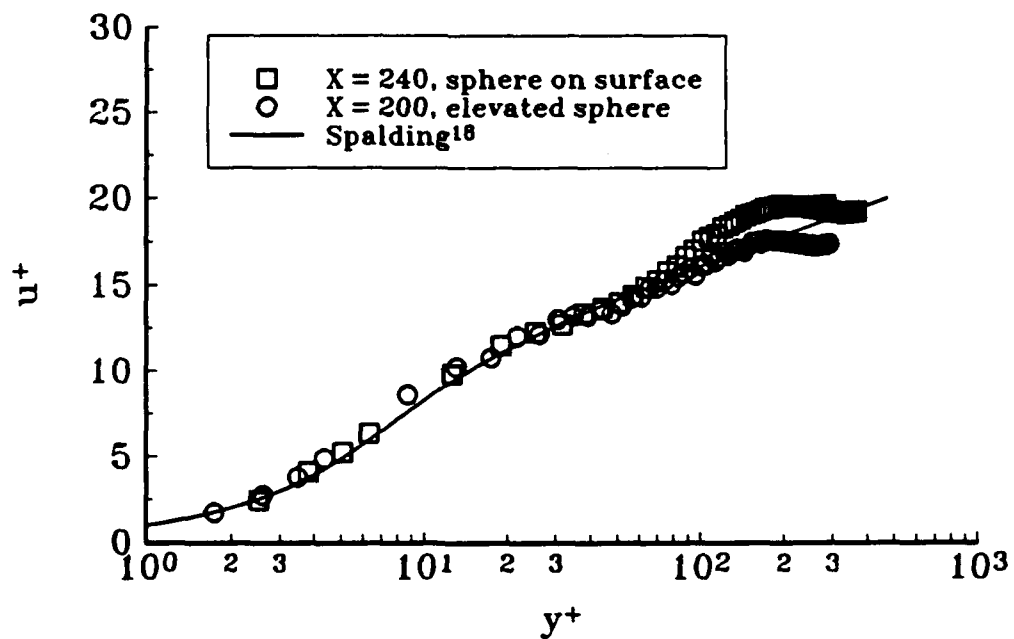


Fig. 1.9 Comparison of mean profiles in inner variables with Spalding's (1961) law of the wall.

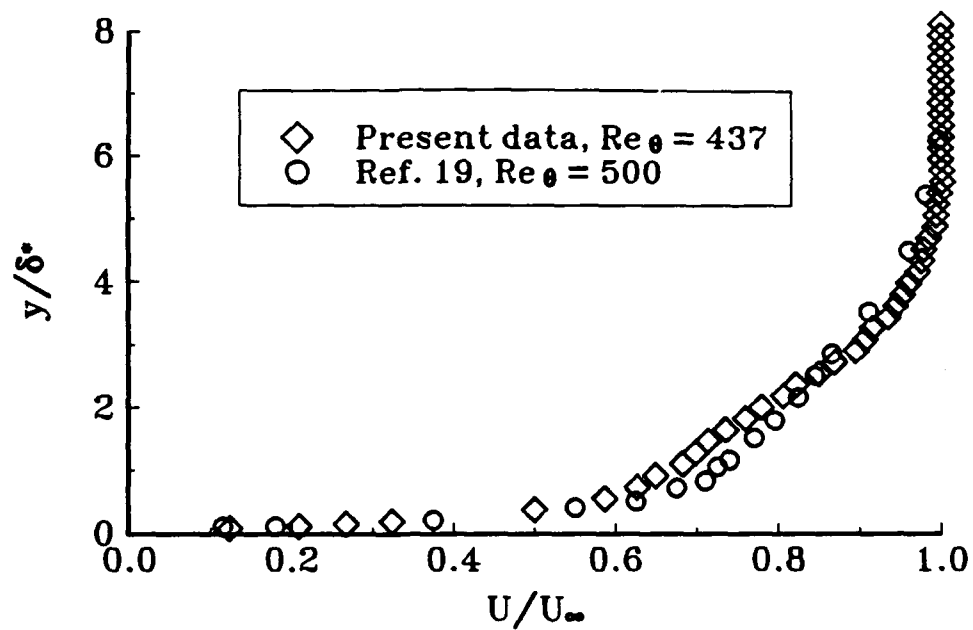


Fig. 1.10 Comparison of the surface mounted sphere wake mean velocity profile at $X = 240$ with turbulent boundary layer data from Purtell, et al(1981).

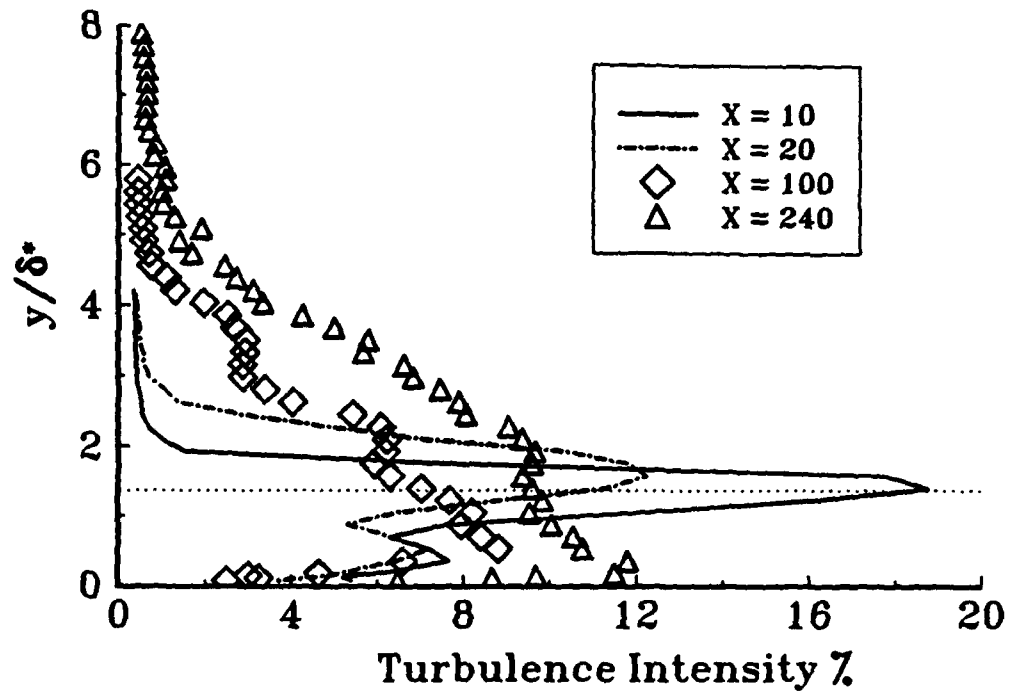


Fig. 1.11 Turbulence intensity profiles in the wake of the surface mounted sphere.

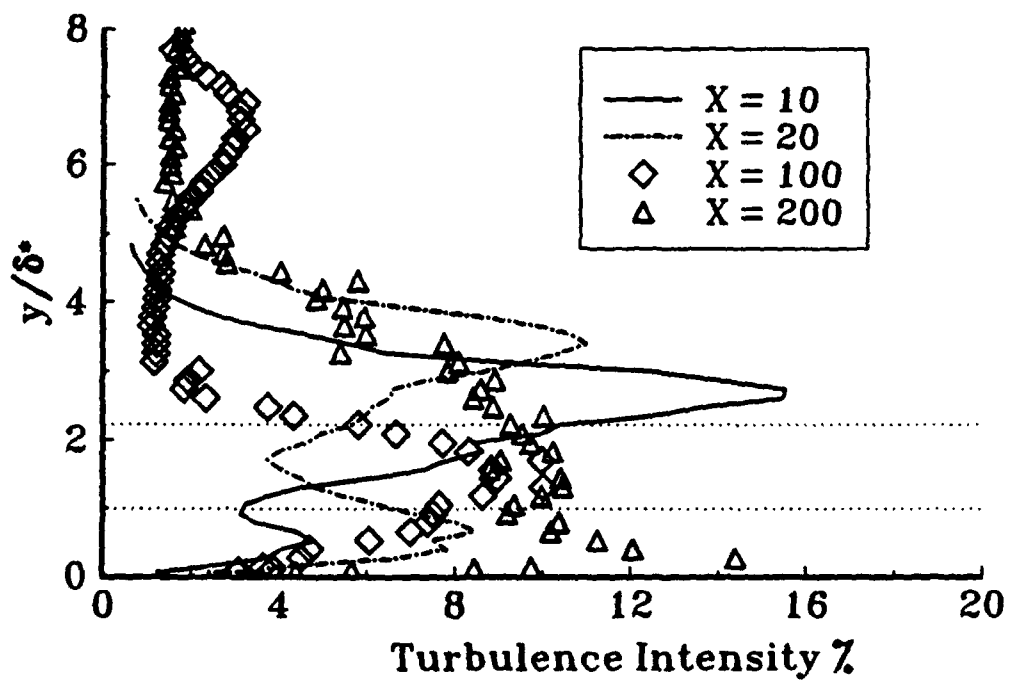


Fig. 1.12 Turbulence intensity profiles in the wake of the elevated sphere.

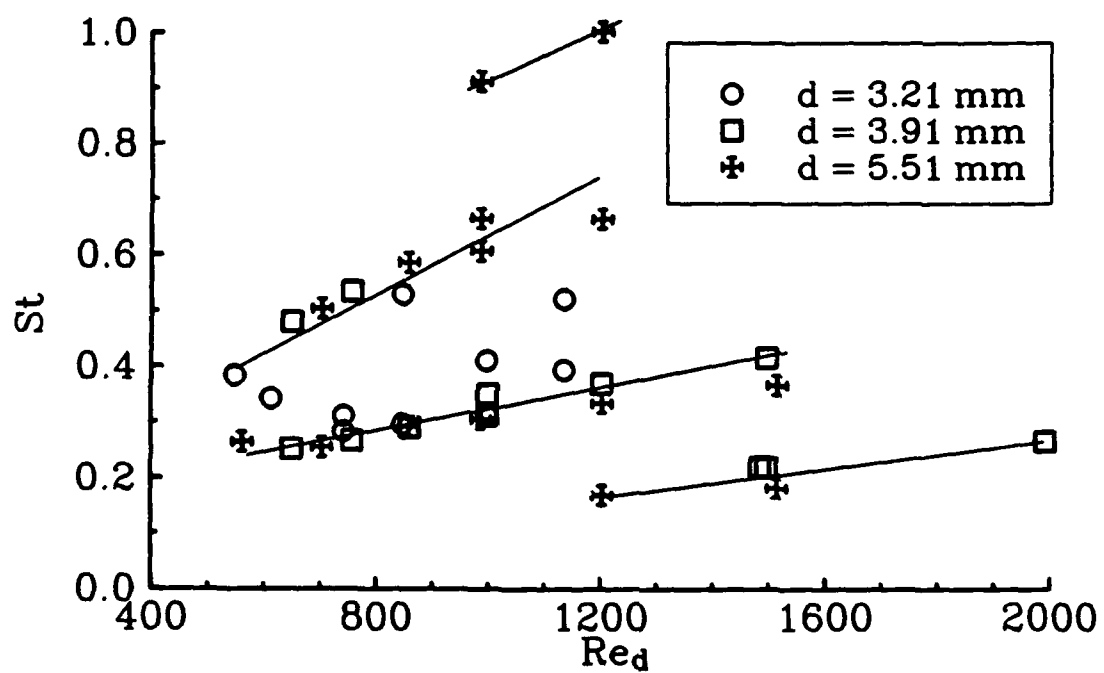


Fig. 1.13 Hairpin vortex shedding frequency Strouhal numbers versus Reynolds number.

Table 1.1 Observations based on the surface mounted sphere flow visualizations.

X	Top of Hairpin, y/δ	Comments
1	----	no hairpin vortices
3	----	no hairpin vortices
5	----	vortex roll up starting
10	0.46 - 0.50	hairpin vortices form
20	0.80	hairpin vortices rising, boundary layer orderly near wall
50	1.16	disturbances near the wall, hairpin legs reattach to surface and flatten
100	1.40	hairpin legs beginning to break up
150	1.60	intermittent turbulent activity near wall
240	1.60	turbulent bulges, every 4th hairpin head moves toward plate

Table 1.2 Observations based on the elevated sphere flow visualizations.

X	Top of Hairpin, y/δ	Comments
1	----	no horseshoe vortex, no hairpin vortices
3	----	1.5d separation bubble attached to sphere
5	0.87	hairpin heads begin to form and rise
10	1.13	hairpin heads rising, legs at height of bottom of sphere and moving toward plate
20	1.30	hairpin legs approach plate, heads rising
50	1.74	hairpin legs reattach to plate surface at $X = 30$, hairpin heads rising
100	2.17	boundary layer irregular near wall, turbulent bursts evident, every 4th vortex head is low
200	2.18	boundary layer chaotic, turbulence bulges affect hairpin heads, periodic pattern

Chapter 2

Turbulent Spot Formation by Freely Convecting Spherical Particles in a Laminar Boundary Layer

Abstract: The generation of turbulent spots from disturbances created by spherical particles that fall freely into a laminar boundary layer was studied experimentally using flow visualization and a video based particle tracking technique. Turbulent spots formed when the particle velocity Reynolds number exceeded 700. Although turbulent wedges form at a similar critical Reynolds number in the wake of fixed surface mounted spheres, the two processes are not the same. Turbulent spots, when they occur, emerge soon after the disturbance generating particle impacts the surface and the spots emerge in the immediate vicinity of the particles. Turbulent wedges form downstream of fixed spherical particles after a gradual development and growth of disturbances near the wall in the wake of the particles. Features such as periodically shed hairpin vortices, observed with fixed particles, are not observed in the freely convecting particle cases.

2.1 Introduction

Laminar flow control technology has the potential to reduce skin friction and flow noise for marine and aeronautical applications. Laminar flow can be maintained to unnaturally large Reynolds numbers by a variety of methods such as surface suction, surface heating(in liquids), and body shaping to maintain a favorable pressure gradient. However, the degradation of laminar flow control performance on a body by the generation of turbulent spots due to surface roughness, by disturbances generated by particles suspended in the freestream flow, and by freestream turbulence defeats this technology in anything but a clean fluid dynamic environment typical to a laboratory. The practicality of this technology for field applications is limited as a result.

The generation of the turbulent patches on a laminar flow surface from environmental disturbances often involves bypass transition. Bypass transition refers to processes that bypass the linear amplification of 2D waves of natural transition and, as discussed by Morkovin(1969), may include numerous paths to turbulence. Similar bypass transition problems can affect turbomachinery applications. Mayle(1991) discusses how bypass transition induced by a variety of disturbances can be a significant factor affecting the performance and design of turbomachinery.

Lauchle and Gurney(1984) quantified the performance of a laminar flow control heated body in a water tunnel. Lauchle, et al.(1986) studied how seeding the freestream with sized particles degraded this performance. Transition Reynolds numbers as large as 37×10^6 , based on the surface arc length on the body and the approach flow velocity, were achieved in a clean flow. However, freestream particles decreased the transition Reynolds number substantially. No minimum particle diameter threshold for performance degradation was observed but larger particles had a more substantial effect. Details of the mechanisms leading to breakdown of laminar flow were not determined. In a similar heated body laminar flow experiment, Ladd and Hendricks(1985) observed that the Reynolds numbers based on the diameter of particles seeded into the freestream and the estimated velocity a distance one particle diameter above the surface at the streamwise position where turbulent spots formed on the body, $Re_{d, crit}$, corresponds approximately to the Reynolds numbers that Hall(1967) observed transition induced by fixed spherical particles on or near the surface in a developing laminar pipe flow. Ladd and Hendricks(1985) speculated that the particles producing the turbulent spots impact the body and momentarily stick.

Chen, Goland and Reshotko(1979) modelled the capture of freestream suspended particles into the boundary layer of a laminar flow body and predicted the rate of turbulent spot generation. Spot generation rate prediction was based on an empirically based particle size criteria since the actual mechanisms are not known. For a given particle size distribution and a fixed specific gravity, the turbulent spot generation rate could be predicted as a function of the freestream velocity.

Vortical structures in the wake of fixed particles mounted on or near the surface in a laminar boundary layer developed gradually into a turbulent wedge at the critical Reynolds number as discussed in Chapter 1. Although strong disturbances are created in the form of hairpin vortices in the near wake of these fixed particles, these disturbances decay. These observations support the speculation by Mochizuki(1961) that the heads of the hairpin vortices have little to do with turbulent

wedge formation in the wakes of surface mounted spheres. The results in Chapter 1 support that the horseshoe vortex formed by the flow separation upstream of surface mounted spheres did not have an effect on turbulent wedge formation. The legs of the hairpin vortices and the disturbances near the wall appear to cause the turbulent wedge to develop. Whether these fixed particle experiments are relevant to the case of a freestream particle crossing streamlines and impacting the surface of a laminar flow control body has not been determined. Ladd and Hendricks(1985) suggestion that the particles momentarily stick at the surface to cause a turbulent spot suggests that this is the case.

A small part of the experiments performed by Hall(1967) in a developing laminar pipe flow included pulling tethered spherical particles into the wall. Particles that were too small to generate a turbulent wedge when fixed at the wall could cause a turbulent spot when pulled to the wall with sufficient velocity.

2.2 Objectives

A series of experiments were performed to provide a qualitative evaluation of the types of disturbances generated near the surface by freely falling particles that enter a laminar boundary layer and impact the surface and to quantitatively determine the conditions resulting in turbulent spot formation. The present effort is not intended to be an exhaustive and definitive study but, given the lack of knowledge of the phenomena involved, is a first step towards gaining a detailed understanding of the mechanisms of spot generation by impacting suspended particles.

2.3 Experimental Apparatus and Procedures

The experiments were conducted in the low speed, closed loop, open channel facility described in Chapter 1 and in Vincent(1993) using the laminar boundary layer that develops on a test plate mounted above the floor of the channel test section. Particles were released from rest to fall from a location 14 cm above the plate and 22.5 cm downstream of the leading edge of the plate. At the fixed freestream velocity used for all of the experiments, $U_{\infty} = 14.3$ cm/s, the particles impact

the plate at locations between 30 and 60 cm downstream of the leading edge. This is as much as twice the distance the fixed particles were located downstream from the leading edge in Chapter 1 but, as mentioned in Chapter 1, the effect on the critical Reynolds number of increasing Re_l in the range used is small.

The probe holding a given particle at the release point was a 2.1 mm outside diameter stainless steel tube with a beveled tip to support the particle. The probe was clamped in position and pierced the free surface of the open channel flow. A vacuum was drawn on a 250 ml flask with a hand pump and this evacuated flask was connected to the support probe by a piece of flexible plastic tubing. A valve was opened to relieve the slight vacuum holding the particle on the end of the probe to allow the particle to fall away from the probe. The cylindrical probe Reynolds number was 323 and the probe sheds a vortex street. This vortex street could affect the particle paths after release. However, the aim of the experiment is to achieve a range of conditions at impact and observe the results. Therefore, the potential effects the probe may have on the particle path are not necessarily significant complications. The particle paths were smooth almost linear arcs with no obvious probe effects in most cases.

The vertical component of velocity of the particles at impact with the test plate is a function of the particle diameter and the particle specific gravity for the fixed release location and freestream velocity. Polystyrene, nylon, and delrin spheres 3.1 mm to 7.9 mm in diameters with nominal specific gravities of 1.05, 1.17, and 1.41 were used to achieve a range of impact conditions. The sphericity and diameter tolerance of the spheres was ± 0.001 " and ± 0.002 ". The diameters of individual spheres used were measured with a micrometer.

Visualization of the disturbances created at the wall during and after particle impact was achieved by seeping a fluorescent dye solution, fluorescein disodium salt, through a narrow inclined slot at the surface of the plate. Walker(1987) discusses aspects of using fluorescein. Visualizations

were done for a range of conditions and videotaped from above the plate to determine which cases produced a turbulent spot. The whole process was repeated and videotaped from the side to determine velocity and pathline histories. Since all of the particles paths are influenced by their unsteady wake, some variation in the conditions at impact between the top and side view replications is likely and some latitude for this variation must be granted when interpreting the results.

The sideviews of the particle paths were analyzed frame by frame. After digitizing the particle positions in a frame by frame play back of the video tape to obtain the paths, velocity histories were obtained by differentiating the paths. Since the process of differentiation of data is susceptible to errors from uncertainty in the pathline data, a cubic spline least squares algorithm with smoothing was applied to the pathline data to estimate the velocity histories.

2. Results

Table 2.1 lists information pertaining to the particles used, the impact conditions and location, whether or not a turbulent spot is generated after impact. Estimates of the terminal vertical velocities are listed for each particle. These terminal velocities are estimated using an empirical drag coefficient given in White(1974) and presented below. One trial for each case and viewing orientation was recorded. Analysis of the video was done frame by frame with human analysis at each step. This process was slow and the number of trials was limited as a result.

2.4.1 Flow Visualization Results

In addition to determining if a turbulent spot is formed, the flow visualizations show details of the disturbances at the wall throughout the process of a particle impacting and then moving along the plate. Typical illustrative examples are presented in this section. In all cases, the particles rolled on the surface after settling from impact but it was not determined whether there was slippage with this rolling motion. The majority of the particles considered bounced at impact. Figure 2.1 shows a sequence of images taken with a 5.56 mm diameter polystyrene particle. The first image, figure

2.1a, is approximately at impact. The flow moves from left to right and $d/\delta \approx 0.62$ and $d/\delta^* \approx 1.85$ at impact. This case corresponds to particle #16 in table 2.1. The Reynolds number based on the two component velocity magnitude of the particle, U_{∞} , at impact is between 1000 and 1100.

A scar in the dye begins forming at the wall just prior to impact and near impact, figure 2.6a, dye has been gathered up into two streamwise oriented tubes or streaks with the particle in between. The source of light is from the bottom of the figures and the particle can be detected from the shadow it leaves. The particle convects faster after impact than the dye laden flow near the surface so that the dye streaks aligned with the freestream flow are left on the upstream side of the particle in its wake. After impact, the U component particle velocity decreases from near U_{∞} to near $0.75U_{\infty}$ in time period of about 0.25s. The velocity in the undisturbed boundary layer is approximately $0.85U_{\infty}$ at the top of the particle, assuming the particle is on the surface. The resultant slip velocity at the top of this moving particle is only $0.1U_{\infty}$ and the resulting slip velocity Reynolds number is only about 85. Spanwise oscillations in the dye streaks are readily apparent on the upstream side of the particle in figures 2.1a near impact and 2.1b 0.66s after impact. Initially, these oscillations may have something to do with the one noticeable bounce after impact but the oscillations continue after impact and could indicate a disturbance amplification stage. Although the velocity of the particle relative to the fluid is low at the top of the particle, this is not the case near the wall where the fluid velocities are lower. Disturbances on the downstream side of the particle are detected in figure 2.1b and these develop quickly into what begins to look like an emerging turbulent spot next to the particle in figure 2.1c which is 1.33 s after impact. The delayed appearance of what looks like instabilities followed by a rapid breakdown of the flow does fit the general scenario described by Breuer and Landahl(1990) for localized strong disturbances. The spot is fully formed 2.0 s after impact and figure 2.1d shows this spot. Notice the streaks left behind the spot on the upstream side of the particle straighten out in figures 2.1c and 2.1d but spanwise oscillation of the streaks are visible in the turbulent spot. This is

can be seen in previous flow visualizations of turbulent spots, see Elder(1960) for example. In this particular case, the particle convects with the spot at the trailing edge of the spot.

Smaller particles were observed to lag the spot they generated and did not generate additional spots or a turbulent wedge. Larger particles moved with the spots, often staying near the leading edge of the spots. The difference in this convective velocity, presumably, is that the particles convect with a velocity that increases with size due to the effect of the velocity gradient.

Figures 2.2a, b, and c show the flow visualization of a subcritical 3.97 mm diameter polystyrene particle at impact and 1 s and 2 s after impact. The particle leaves a dark dye shadow on its upstream side and two bright dye streaks extend downstream of the particle. This case corresponds to sphere #18 on table 2.1. At impact, $d/\delta \approx 0.42$ and $d/\delta^* \approx 1.26$ and the velocity at the top of the particle in the undisturbed boundary layer is about $0.67U_\infty$. The U velocity of the particle slows to, roughly, $0.3U_\infty$ shortly after impact. This corresponds to a velocity below $y/\delta = 0.2$ in the undisturbed boundary layer. Since the dye streaks are moving faster than the particle, they are probably lifted farther from the wall than $y/\delta = 0.2$. The slip velocity at the top of the particle is actually larger than the case considered in figure 2.1 and the Reynolds number based on this slip velocity is about 225. At this Re_d , based on the results in Chapter 1, the particle is probably not be shedding hairpin vortices periodically but if vortices are shed, they do not lift.

Figure 2.3a shows a $d = 6.35$ mm polystyrene particle, #15 on table 2.1, just after estimated impact. The scar formed in dye layer at the surface is wishbone shaped with streaks at oblique angles. Figure 2.8b is 0.66 s later and after the particle has landed from the bounce on impact. The half angle of the oblique streaks in the dye is 25° . This angle is larger than the half angle enclosing the area passed over by a growing turbulent spot. The typical maximum half angle subtended by a spot from its virtual origin is 10° , see Wignanski, et al.(1976). The dye patterns and disturbances generated by the double impact of this bouncing larger particle are complex enough that more subtle

features that might be present such as the spanwise oscillation of the streamwise streaks noticed in the case for figure 2.1 are not detected. A spot begins to emerge about 1 s after impact and figure 2.3c shows the emerging spot 1.33 s after impact. The spot might be considered slightly more developed than the case considered in figure 2.1. However, some of the disturbances in figure 2.3c at the spanwise edges of the emerging spot appear to be artifacts of the impact disturbance and not part of the spot. The edges of what looks like the emerging spot are within a 10° wedge extending from near the point of impact.

The time required after impact for the spot to begin emerging in the cases considered is $tU_\infty/\delta \approx 15$ to 20 or $tU_\infty/\delta^* \approx 45$ to 60. In the simulation of the evolution of strong localized disturbances by Breuer and Landahl(1990), the magnitude of u'/U_∞ was 0.05 after $tU_\infty/\delta^* = 43$ but rapid growth was not observed until $tU_\infty/\delta^* = 117$ and after. The present disturbances are not what was simulated and the development into a spot is rapid in comparison.

The dye streaks formed at various stages of the events in figures 2.1 - 2.3 could be the result of shear layers, waves, or tubes of vorticity above the dye layer at the wall. This exact nature of these disturbances is difficult to judge because the dye at the wall does not show structural features that may be present away from the wall unless the dye is first lifted from the wall. The dye is not lifted significantly until a spot begins to emerge. The blocking effect of the wall on the fluid that the approaching particle displaces may result in the initial scar formation for the larger faster falling particles such as shown in figure 2.3a. It is significant that the dye is not lifted appreciably until the spot forms. Anything as vigorous as the hairpin vortices associated with the fixed particle case in Chapter 1 is not likely. The trailing wake left by these particles as they fall is not expected to have a large effect near the wall either. The polystyrene particles used in the cases considered in figures 2.1 - 2.3 were all in near equilibrium with the U component of velocity for much of the freefall time period prior to impact. The trailing wake should extend above the particle along a vertical line at

impact and convect with the freestream velocity. The spots emerge from near the surface immediately adjacent to the particle for critical cases.

2.4.2 Impact Conditions

The observed trends in the conditions at impact are generally consistent but there are variations. These variations are probably due to the unsteady and random character of these falling particle wakes with increasing particle Reynolds number. The wake of the probe near the release point could possibly affect the particle trajectory and the resulting conditions at impact. Errors in the measured values are possible contributors to this variation of the impact velocity data also. The uncertainty in the measured particle velocities is estimated as no more than 10% of the freestream velocity. Vincent(1993) provides an error analysis.

To estimate the scatter typical to the measurements of the impact velocities, consider the polystyrene particle data in table 2.1. The polystyrene particles come into near equilibrium with the streamwise velocity of the freestream flow before impacting the plate. The polystyrene particles are lighter and fall more slowly than the other materials. Therefore, they accelerate from rest to the freestream velocity more quickly than the other materials and they have more time to approach equilibrium before impacting the plate because they fall more slowly than the denser particles. The six impact U component velocities for the polystyrene particles are all near the freestream velocity with a standard deviation from the freestream velocity of 4% and the largest deviation is 7.7%. Note that the seventh polystyrene particle, #19 on table 2.1 did not impact the plate in the field of view.

The streamwise velocity at impact with nylon and delrin particles shows the largest variations in results with some values low relative to the rest; particles 1, 6, 7, and 9 are examples of this type of deviation. In all cases, the vertical velocity at impact listed on table 2.1 is less than the terminal velocity estimate for a sphere in a still fluid. The smaller lighter particles are closest to terminal vertical velocity.

2.4.3 Conditions Generating Turbulent Spots

A velocity associated with the particle at impact should scale with the size of the resultant disturbance and, therefore, correlate with turbulent spot generation. Certainly, if the particle U velocity were in near equilibrium with the freestream flow prior to impact, the vertical velocity at impact, V_{im} , might be expected to scale well with the resulting disturbance since it is the only velocity component out of equilibrium with the flow. Figure 2.4 plots the ratio V_{im}/U_{∞} versus $Re_{dV_{im}}$, the Reynolds number based on the vertical impact velocity. The solid symbols on the figure did not generate a turbulent spot. A few points on figure 2.4 do not fit the trends. For example, particle #17 on table 2.1 has low V_{im} and $Re_{dV_{im}}$ values. The trend in the data indicates that the critical values of $Re_{dV_{im}}$ increase with increasing V_{im}/U_{∞} . This increase in the critical Reynolds number with disturbance strength was not expected. Based on other transitional flow situations, it is expected that a threshold critical Reynolds number may exist as with boundary layers or sphere wakes or that the critical Reynolds number might decrease with increasing disturbance strength similar to roughness element effects. This unexpected behavior suggests that V_{im} alone does not scale with the strength of the disturbances leading to spot formation. It is possible that pathline differences affect the outcome but this view is not favored. The heavier particles produce the larger V_{im}/U_{∞} and have a steeper impact angle than the smaller lighter particles. The difference in the inclination angle for the subcritical conditions nearest to the critical state varies from 27° to 50° going from polystyrene to delrin.

The two component slip velocity based on the difference between the impact velocity and the freestream velocity was considered to correlate critical events with impact conditions. The slip velocity magnitude is $\Delta U = [(U_{im} - U_{\infty})^2 + V_{im}^2]^{1/2}$. However, the U component of the slip velocity is not large for the near critical cases of interest and the resulting trends are similar to those in figure 2.4 with V_{im} .

The Reynolds numbers based on the slip velocities, V_{im} or ΔU , characterize the state of the particle wake at impact. The findings of fixed spherical particle study in Chapter 1 suggest that even large disturbances generated away from the wall but in the boundary layer have little, if any, direct effect on the generation of a turbulent wedge. Disturbances near the wall, detected by fluctuation intensity peaks below $y/\delta = 0.25$ in Chapter 1, appear to lead to flow break down in the fixed particle wakes. This is supported by the present flow visualizations that show the spots emerge from the surface and this appears to be the result of disturbances at or below $y/\delta = 0.2$. There is no clear reason to expect that the wakes trailing a convecting particle would affect turbulent spot generation.

The slip velocities mentioned above do not quantify the size of the disturbance the particle generates near the wall at impact. The combined two component impact velocity magnitude, $U_{tot} = (U_{im}^2 + V_{im}^2)^{1/2}$, where U_{im} is the streamwise component of the particle velocity at impact and not a slip velocity, should scale well with the size of the disturbances generated near the wall by the particles at impact. The reasoning is that near wall fluid velocities are low and the data indicate the particle does not slow noticeably just prior to impact. Figure 2.5 shows the impact velocity magnitude versus the Reynolds number based on U_{tot} . The conditions generating turbulent spots near the critical condition tend to cluster but this is difficult to judge given the coarseness of the data grid achieved with the various diameter particles and specific gravities that were used. Actual values of Re_{tot} are listed in table 2.1. The sparse data matrix and the uncertainty in the values means that identifying critical Reynolds number trends accurately is not possible unless there are reasonably large and consistent variations over the range of conditions and this is not the case. The critical Reynolds number is constant within the ability to ascertain the trend. Allowing for a 10% uncertainty, the range for the critical condition that overlaps for the three materials is $Re_{tot} = 700$ to 800 . It appears that particle size relative to the boundary layer thickness and the size of the disturbance, U_{tot}/U_{∞} has

little effect and Re_{∞} is constant. This is supported by the heated body experiment by Lauchle, et al.(1986).

The influence of the size of particles seeded into the freestream on the performance of a laminar flow control heated body was considered in experiments by Lauchle, et al(1986). The Reynolds number based on the approach flow velocity and particle diameter was plotted versus d/δ^* where δ^* is the displacement thickness at the upstream most location that spots emerged on the body. These critical condition data collapsed and the trend is shown in figure 2.6 which is reproduced from Lauchle, et al.(1986). Data include 3 heating conditions from 27 to 75 kW input to heat the body. In the present experiment, the Reynolds number based on U_{∞} is felt to be equivalent of the approach flow based value. The d/δ^* values in the present experiment span a range from 1.1 to 3.5, approximately, with the conditions straddling the critical state spanning $d/\delta^* = 1.1$ to 1.85. In Lauchle, et al,(1986) the values spanned a range from $0.03 < d/\delta^* < 0.7$ and it was observed that for $d/\delta^* > 0.5$, the critical freestream based Reynolds number was constant, within the data scatter, with values in the range $690 < Re_{d\text{ crit}} < 770$, see figure 2.6. As noted above, the estimated critical Reynolds number in the current experiment is similar.

The observed transition Reynolds number for these convecting particles is similar to the $Re_{d\text{ crit}}$ values based on the velocity in the undisturbed flow at the top of the particle that were observed with fixed particles in Chapter 1 which are $630 < Re_{d\text{ crit}} < 700$. The transition of the wake of spheres in a uniform flow occurs at Re_d near 800, see Sakamoto and Haniu(1990). The near agreement between these three sets of critical Reynolds numbers may be fortuitous. The fixed particle transition discussed in Chapter 1 appears to depend on the lifting of low speed fluid by the vortices in the wake and the interaction of the legs of hairpin vortices. At the critical condition a turbulent wedge develops slowly as the disturbances caused by the fixed particle grow. Transition in the case of a sphere in a uniform freestream involves a free shear layer instability. The impacting particles

generate a turbulent spot by a mechanism that does not appear to involve either hairpin vortices or the instabilities in shear layer shed into the wake of the falling particle.

2.4.4 Pathline and Velocity History Data

Although the pathline and velocity history data prior to impact may not directly affect turbulent spot generation, these data are interesting and are considered below. The pathlines traced by the particles as they fell to the surface were usually mild arcs that were nearly straight lines. The arcs are concave downward indicating the V velocity is increasing relative to the U velocity as is expected for a particle in freefall. Figure 2.7 contains an example of a typical particle pathline, particle #5 on table 2.1 which is a $d = 3.94$ mm diameter nylon particle. Figure 2.8 is the corresponding U and V velocity data versus the time from release for particle #5. The variables figure 2.7 are the horizontal and vertical distance from the release point normalized with the distance the particle could fall. A small bounce is indicated in the figures and one or two bounces were typical to most of the particles. These trajectory and velocity history data are similar to the computed results in Part III of this report but the computed trajectories consistently impact the plate upstream of the observed impact locations. There are other differences between the observed and computed trajectories which are commented on in the following discussion.

The bounce of the particles after impact obviously affects the disturbances generated at the surface and possibly turbulent spot formation. However, for the cases near the critical condition, there is no definite indication that spot formation is affected. For the polystyrene particles, a turbulent spot was observed with particle #17 on table 2.1 but not with #18; neither particle bounced detectably. The nylon particle #5 had a small bounce and generated a spot. Nylon particle #6 may have bounced but this was small enough that it was difficult to detect and no spot was formed. The two delrin particles straddling the critical condition, #11 and #12, both bounced quite noticeably. Thus, all combinations of bouncing and not bouncing subcritical and supercritical particles were

observed. When spots did form, they emerged 1 s to 1.33 s after impact in all cases and there is no clear indication the bounce had an effect on spot formation.

Some of the particle velocity histories exhibited oscillatory behavior that was not predicted in the computations in Part III. Figures 2.9 and 2.10 are velocity histories of some of these more unusual cases, particles #7 and #9 on table 2.1. The pathlines for these two cases are the delrin data shown on figure 2.7 and the pathline slope is increasingly negative as impact is approached. This trend in the pathlines indicates that the U component of velocity is decreasing substantially in the last stages of the trajectory relative to the V velocity and this is the case in figures 2.9 and 2.10. The velocity history for sphere #7 shows an overshoot of the freestream velocity of about 20% followed by an undershoot of U_∞ by 30%. Sphere #9 overshoots U_∞ by almost 40% then undershoots it by almost 50% at impact. This behavior is typical to the delrin particles. There were similar variations for the smallest two delrin particles which overshoot and then undershoot U_∞ by 25% and 30% but then relaxed back to a velocity near U_∞ at impact.

The larger diameter nylon sphere data were similar to the delrin data with noticeable velocity over and undershoots. The smaller nylon spheres and the larger polystyrene spheres were similar to particle #5 data shown in figures 2.7 and 2.8 with the U velocity data consistently exceeding U_∞ by as much as 15%. The smaller polystyrene data accelerated to a velocity within 10% of U_∞ with both positive and negative deviations from U_∞ ; this behavior corresponds with the estimated accuracy of the measurement. Thus, there is a consistent trend of an increasing propensity for large velocity oscillation with increasing particle diameter and increasing specific gravity. The smallest and lightest particles produced the expected results which includes a monotonic trend in the velocity history with no deviations of the streamwise component of velocity with the freestream velocity that are larger than the expected error as the particle approaches equilibrium prior to impact.

The vertical velocities all rapidly increase to near the impact value in 25% or less of the time between release and impact for all diameters and materials. Assuming the vertical velocity is the impact velocity is reasonably accurate for the purpose of discussion. Also, most of the particles have U velocities within 25% of U_{∞} for the majority of their trajectories. Assuming this for the purpose of a general discussion, the slip velocity Reynolds numbers typical to most of a particle's trajectory can be estimated from impact velocities. The smaller polystyrene particles had Reynolds numbers based on the two component slip velocity below 330. Based on fixed sphere data described by Sakamoto and Haniu (1990), these particles are shedding hairpin vortices periodically with a fixed orientation. The next two larger polystyrene particles, #14 and #15, the smaller 3 nylon particles, #4, 5, and 6, and the smallest 2 delrin particles, #11 and 12 had slip velocity Reynolds numbers from 370 to 840. The wake may not be turbulent but the orientation of the hairpin vortices shed by these spheres is likely to be increasingly irregular with increasing Reynolds number in these cases. The largest polystyrene particle, the larger nylon particles and most of the delrin particles had Reynolds numbers near 1000 or larger and a turbulent hairpin vortex shedding process with an irregular and random orientation is expected. The acceleration of the spheres in the present experiment involves both the speed and direction and this may change the character of the wake development from these fixed particle observations of Sakamoto and Haniu(1990) but it is expected the fixed particle behavior is a useful guideline.

The unsteady particle wake produces unsteady forces on the particle that could affect its path. It is expected that the conditions for which fixed spheres are shedding hairpin vortices regularly with a fixed orientation would produce the least scatter in the pathline and velocity history data. This apparently occurs for the smaller and lighter particles like the polystyrene spheres. Irregular shedding with random orientations and finally, turbulent shedding with an unstable shear layer shed from the sphere should increase the spread in the pathline and velocity history data.

The computed particle trajectories and velocity histories in Part III do not show the variations and oscillations observed in the experiments. The model used in Part III does account for the transient nature of the particle release but only in an averaged sense. The unsteady character of the wake, particularly when the wake is expected to have a random and irregular influence on the drag force on the particle, is not incorporated into the computations. Consider a simple example that the computed model would fail to handle. Spherical particles released from rest in a water filled isothermal tank with no flow will not typically strike the bottom of the tank at a point exactly below the release point when the conditions are generally similar to the experiments; transitional and turbulent wakes with specific gravities from 1.05 to 1.41. The mean impact position on the tank bottom for a large number of trials should be directly below the particle release point and it is the mean that the model in Part III predicts.

The potential exists for velocity overshoots and undershoots if the unsteady wake can have a significant affect on the particle path and there is an appropriate time lag for the wake to adjust to the changes in the flow conditions. The low frequency mode Strouhal number for the hairpin vortex shedding frequency of a fixed sphere in a uniform flow due the the instability of the averaged wake is about 0.2 for $700 < Re_d < 3000$ where $St = fd/U$, see Sakamoto and Haniu(1990). Using the slip velocity and this value of the Strouhal number, shedding frequencies range from 5 to 10 Hz for the nylon and delrin particles with the lower values for the larger particles. The polystyrene particle shedding frequencies are less than 3 Hz. The time from release to impact spanned a range from 0.6 s to 0.8 s for delrin particles to 2.0 s to 2.3 s for the polystyrene particles. The various particles shed 4 to 10 vortices in time span between release and impact based on these estimates from steady flow fixed sphere data. Since the process of shedding one vortex effects the development of the next, a wake adjustment time to the changing particle velocity of two shedding cycles may be reasonable. In

the typical case, the particle travels 30% of its path in this time. This adjustment time is comparable to the time span of the swings in the U component velocity associated with the over and undershoots.

The vertical velocity data do exhibit irregularity but this is not like the low frequency oscillations seen in the streamwise particle velocity histories. The vertical velocity changes are generally smaller and at higher frequency. Abrupt changes in the acceleration in the vertical velocity, indicated by changes in the slopes of the velocity histories, see figures 2.8, 2.9, and 2.10, are typical. The terminal velocities for a particle in a still fluid listed in table 2.1 all exceed the impact velocity but the particles appear to be accelerating very slowly in the last half of the trajectories prior to impact in all cases. This almost asymptotic approach to the terminal velocity is similar to the vertical velocity histories computed in Part III.

The U component particle velocity is influenced directly by the unsteady fluid dynamic forces on the particle but the vertical velocity is influenced directly by the constant gravitational pull and as well as the drag forces. The relative magnitudes of the fluid dynamic and gravitation forces change with particle diameter and material. Consider a middle size particle, $d = 5.51$ mm, fixed in a flow with the freestream velocity prior to release, $Re_d = 847$. As a simple approximation, an empirically based drag coefficient can be used to estimate the drag force on the sphere for a uniform steady flow. From White(1974), $C_d = F/(1/2\rho U^2 A) \approx (24/Re_d) + \{6/(1 + Re_d^{1/4})\} + 0.4 = 0.628$ for the $d = 5.51$ mm particle fixed in the freestream. The drag force is $F \approx 1.53 \times 10^{-4}$ Newtons. This is the largest drag force expected on the particle and estimates conditions at release. The gravitational force is 4.28×10^{-5} , 1.46×10^{-4} , and 3.51×10^{-4} Newtons for polystyrene, nylon, and delrin particles. The gravitational force approximately equals or exceeds by a factor of 2 the largest fluid dynamic drag force expected with nylon and delrin for this middle size case. For the largest particles the gravitational forces are relatively larger and for the smaller particles it is relatively smaller. Given that the gravitational force is able to accelerate all of the particles to close to the impact velocity in

only 25% of the of the time from release to impact, it seems reasonable that unsteady fluid dynamic forces, which can be comparable in magnitude to the gravitational force, could cause the over and undershoots of the freestream velocity. These force estimates also indicate that it is probably the character of the wake and not the ratio of the gravitational to fluid dynamic drag that is important in the present cases. The particles with the relatively larger gravitational forces have the most irregular behavior and the turbulent wakes.

Other possible explanations for the U velocity history oscillations have been sought simply because the observed U velocity variations were not expected. Certainly there is concern that errors in the procedure could be a contributing factor. In light of the fact that the particles with low Re_d behaved as expected and the faster higher Re_d particles behaved unexpectedly, this seems unlikely. The displacement between video frames is larger for the faster particles and the relative uncertainty in estimation of this displacement decreases as a result. Repeated trials would have helped to define the range of variation which is not known based on the current experiments. Thus, it is not possible to judge how extreme some of the variations observed really are. Undetected defects in the particles, attached small bubbles that were not noticed, or the influence of the release process and the probe wake are other possible explanations for the U component velocity oscillations. The topic of pathline and velocity history irregularity for falling spheres in a uniform quiescent freestream requires further study.

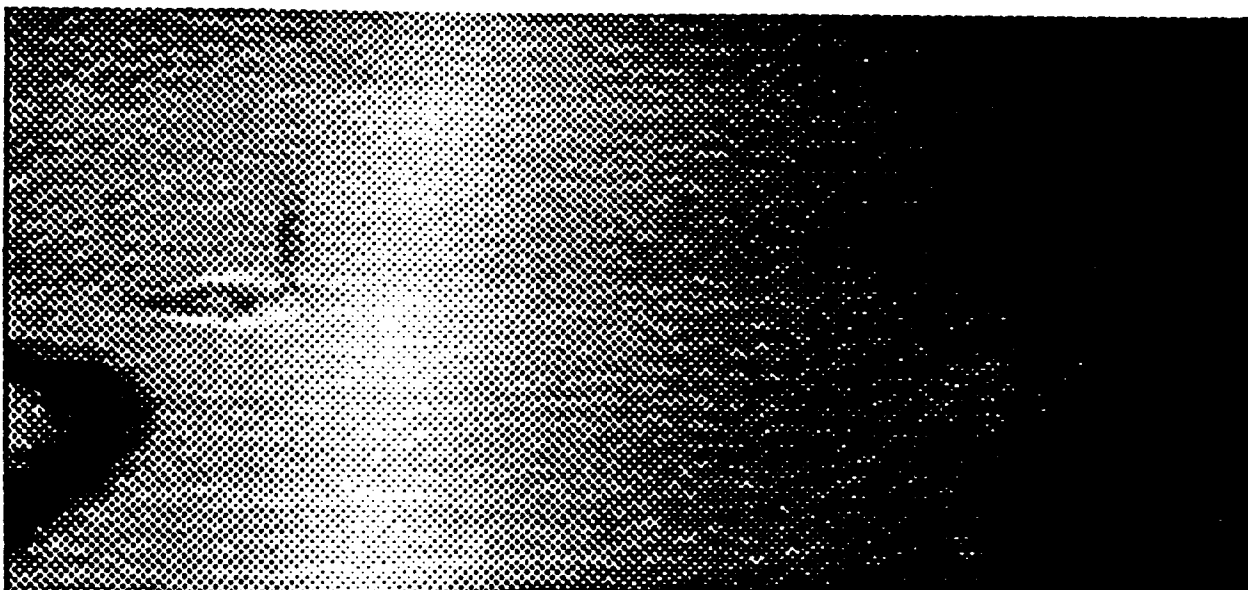
2.5 Summary and Conclusions

Flow visualization and particle tracking have been used to study turbulent spot generation by spherical particles that fall freely into a laminar boundary layer. The critical Reynolds number based on the velocity of the particle at impact and the particle diameter is approximately 700 to 800. This is in agreement with results on a laminar flow control heated body by Lauchle, et al(1986) and supports, for values of $1.85 > d/\delta^* > 0.5$, that the critical Reynolds number is constant. Although

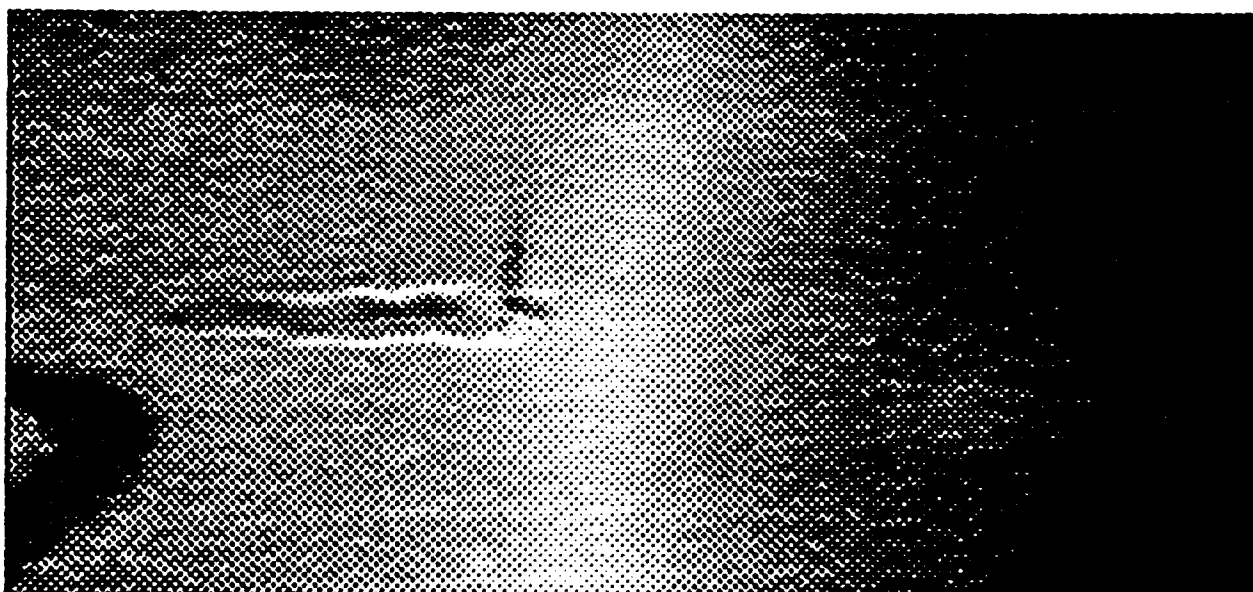
this is similar to the critical Reynolds number that fixed surface mounted spheres generate turbulent wedges, the processes involved do not appear to be similar. In all cases, the turbulent spots emerge in the immediate vicinity of the convecting particles and it appears that this is a result of disturbances created by the particle near or below $y/\delta \approx 0.2$. The larger particles convected downstream on the surface with the turbulent spots they generated but the smaller particles rolled on the surface of the plate at lower velocity than the spots they generated. In no case were particles observed to generate more than one turbulent spot or to create a turbulent wedge after impact. The spots begin to emerge within a time from impact of $45 < tU_\infty/\delta^* < 60$, approximately, and the spots emerge with approximately 25 particle diameters the impact location. Turbulent wedges form in the wake of a fixed sphere 50 to 75 particle diameters downstream of the particles at the critical condition. In some of the convecting particle cases with less complicated and smaller appearing disturbances at impact, spanwise oscillations are observed after impact and prior to the emergence of a turbulent spot. These oscillations may indicate a process of selective amplification but the short time span between the particle impact and the emergence of a turbulent spot suggests this amplification stage is nonlinear and a bypass transition process is active.

2.6 References

- Breuer, K. S. and Landahl, M. T., 1990, "The Evolution of a Localized Disturbance in a Laminar Boundary Layer. Part 2. Strong Disturbances," *JFM*, V220, pp. 595-621.
- Chen, C. P., Goland, Y., and Reshotko, E., 1979, "Generation Rate of Turbulent Patches in the Laminar Boundary Layer of a Submersible," *Viscous Flow Drag Reduction, Progress in Astronautic and Aeronautics*, V72, G. R. Hough editor, AIAA, pp. 73-89.
- Elder, J. W., 1960, "An Experimental Investigation of Turbulent Spots and Breakdown to Turbulence," *JFM*, V9, pp. 235-246.
- Hall, G. R., 1967, "Interaction of the Wake from Bluff Bodies with an Initially Laminar Boundary Layer," *AIAAJ*, V5, N8, pp. 1386-1392.
- Ladd, D. M., and Hendricks, E. W., 1985, "The Effect of Background Particulates on the Delayed Transition of a Heated 9:1 Ellipsoid," *Exp. in Fluids*, N3, pp. 113-119.
- Lauchle, G. C. and Gurney, G. B., 1984, "Laminar Boundary Layer Transition on a Heated Underwater Body", *JFM*, V144, pp. 79-101.
- Lauchle, G. C., Petrie, H. L., and Stinebring, D. R., 1986, "Effects of Particulates on the Delayed Transition of a Heated Body," Applied Research Laboratory Technical Memorandum 86-213.
- Mayle, R. E., 1991, "The Role of Laminar-Turbulent Transition in Gas Turbine Engines," *JFE*, V113, pp. 509-537.
- Mochizuki, M., 1961, "Smoke Observation on Boundary Layer Transition Caused by a Spherical Roughness Element," *J. Phys. Soc. of Japan*, V16, N5, pp. 995-1007.
- Morkovin, M. V., 1969, "On the Many Face of Transition," in *Viscous Drag Reduction*, C. S. Wells, editor, Plenum Press, New York, pp. 1-31.
- Sakamoto, H., and Haniu H., 1990, "A Study on Vortex Shedding From Spheres in a Uniform Flow," *JFE*, V112, pp. 386-392.
- Vincent, D. C., 1993, "Transition Induced by Fixed and Freely Suspended Spherical Particles in Laminar Boundary Layers," Masters thesis, Aerospace Engineering Department, The Pennsylvania State University.
- Walker, D. A., 1987, "A Fluorescence Technique of Measurements of Concentration in Mixing Liquids," *J. Physics E: Sci. Instr.*, V20, pp. 217-224.
- White, F. M., 1974, *Viscous Fluid Flow*, McGraw-Hill, 1st edition, New York, p. 209.
- Wynagnanski, I., Sokolov, M., and Friedman, D., 1976, "On a Turbulent Spot in a Laminar Boundary Layer," *JFM*, V78, pp. 785-819.

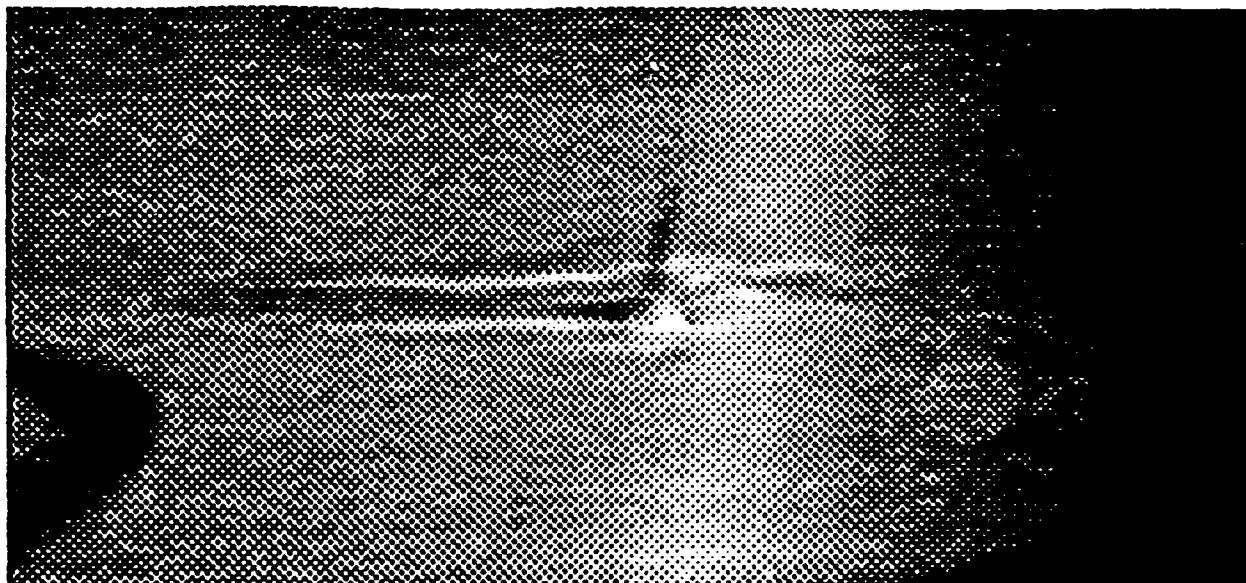


(a)



(b)

Fig. 2.1 Flow visualization of $d = 5.56$ mm diameter polystyrene particle generated events.
(a) $t = 0$ s, (b) $t = 0.66$ s

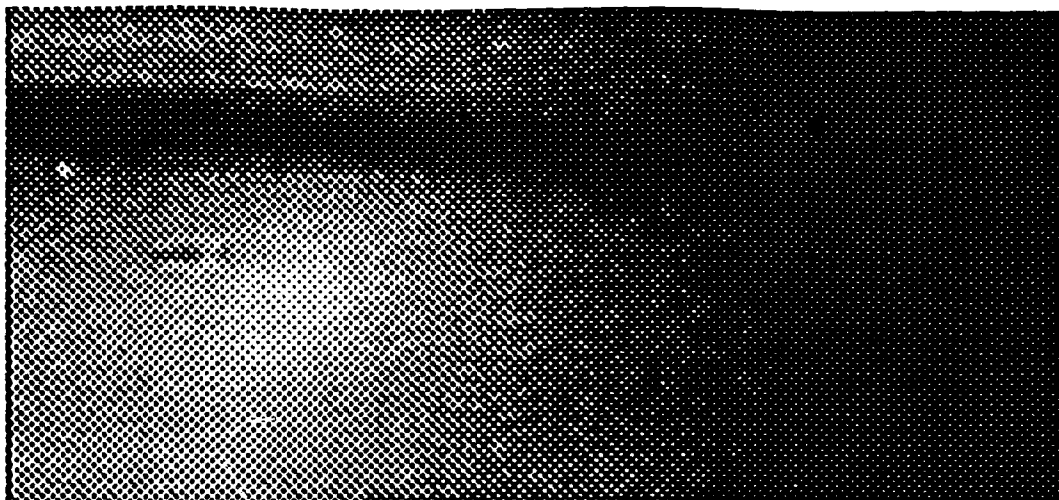


(c)

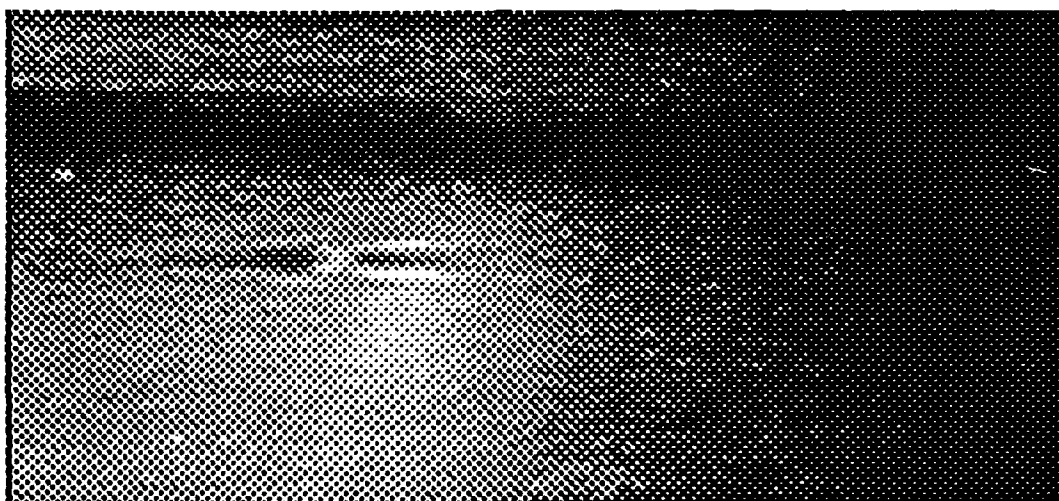


(d)

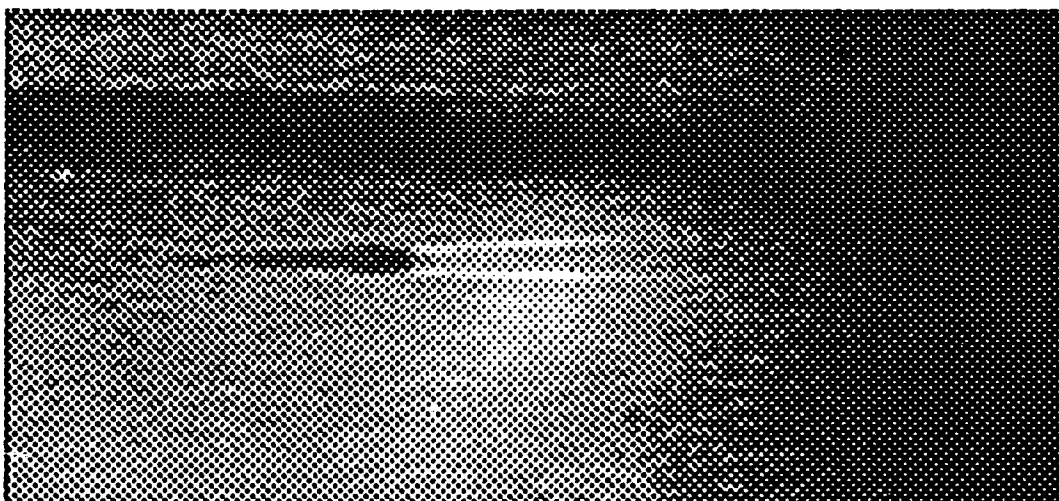
Fig. 2.1 Flow visualization of $d = 5.56$ mm diameter polystyrene particle generated events.
(c) $t = 1.33$ s, (d) $t = 2.0$ s



(a)

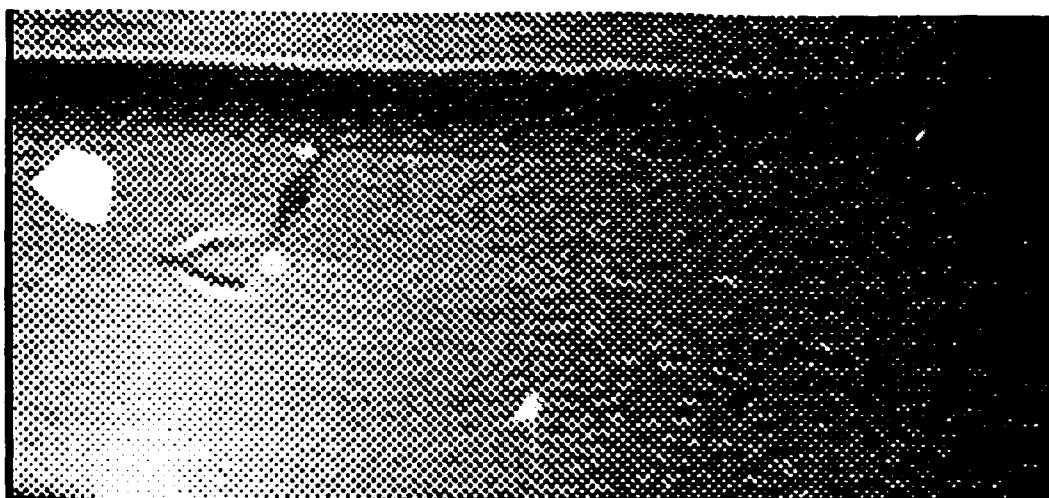


(b)

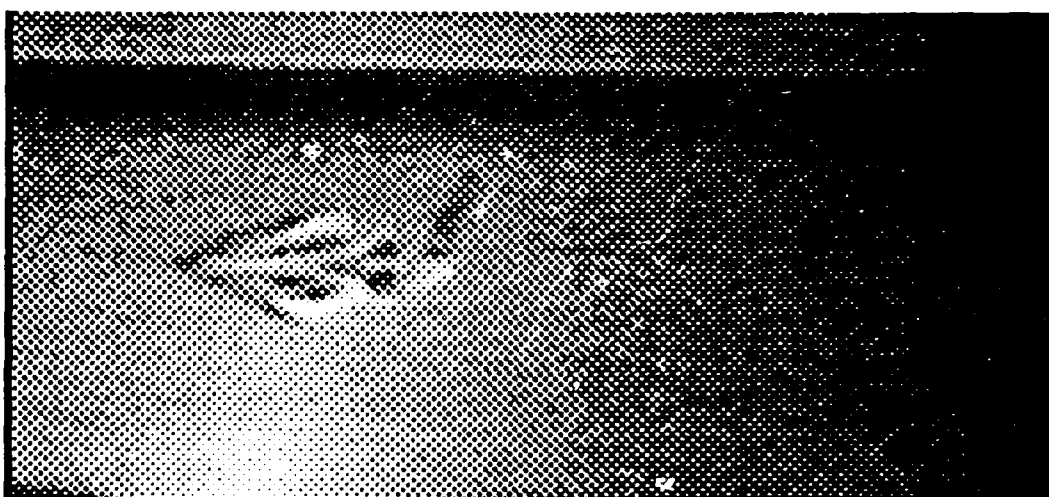


(c)

Fig. 2.2 Impact of a subcritical $d = 3.97$ mm diameter polystyrene sphere. (a) $t = 0$ s, (b) $t = 1$ s, (c) $t = 2$ s.



(a)



(b)



(c)

Fig. 2.3 Events generated by impact of $d = 6.35$ mm diameter polystyrene particle at (a) $t = 0$ s, (b) $t = 0.66$ s, and (c) $t = 1.33$ s.

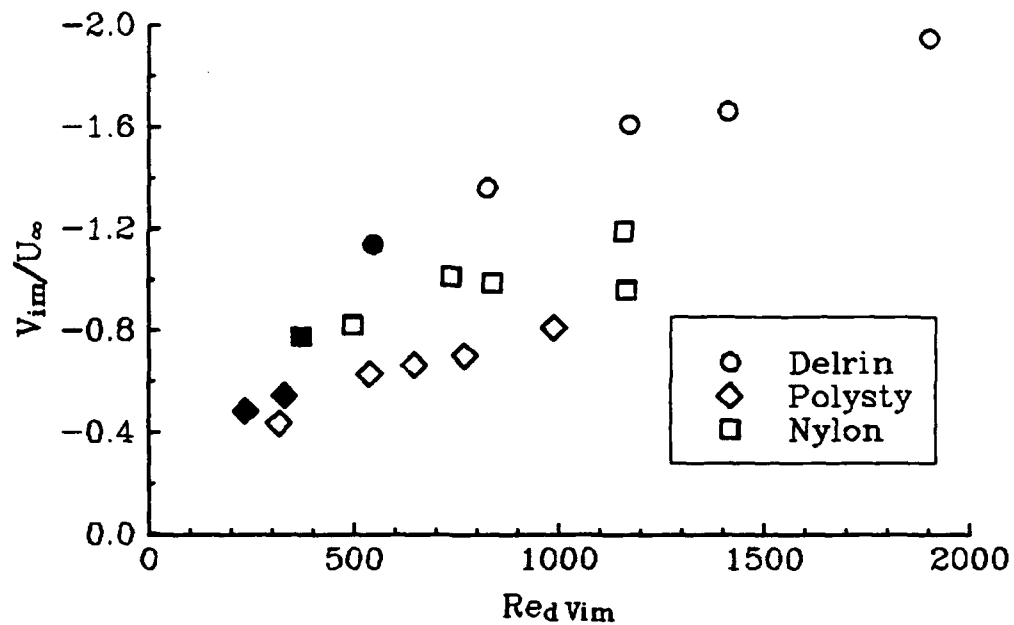


Fig. 2.4 Vertical impact velocity versus Reynolds number. Solid symbols are conditions not generating a turbulent spot.

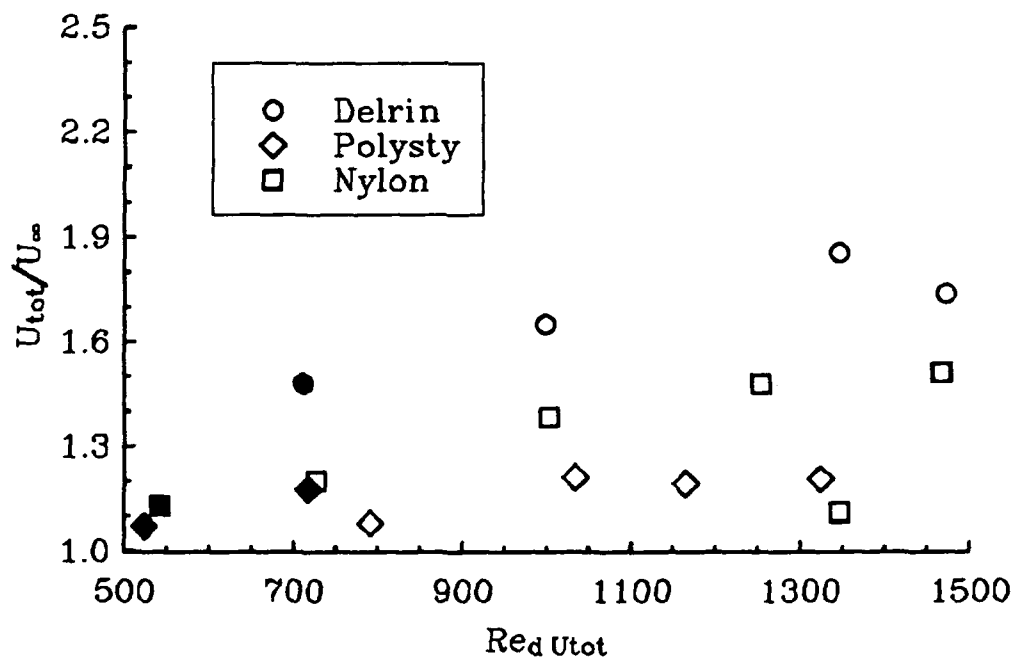


Fig. 2.5 Two component impact velocity magnitude, U_{tot} , versus Reynolds number. Solid symbols are conditions that did not generate a turbulent spot.

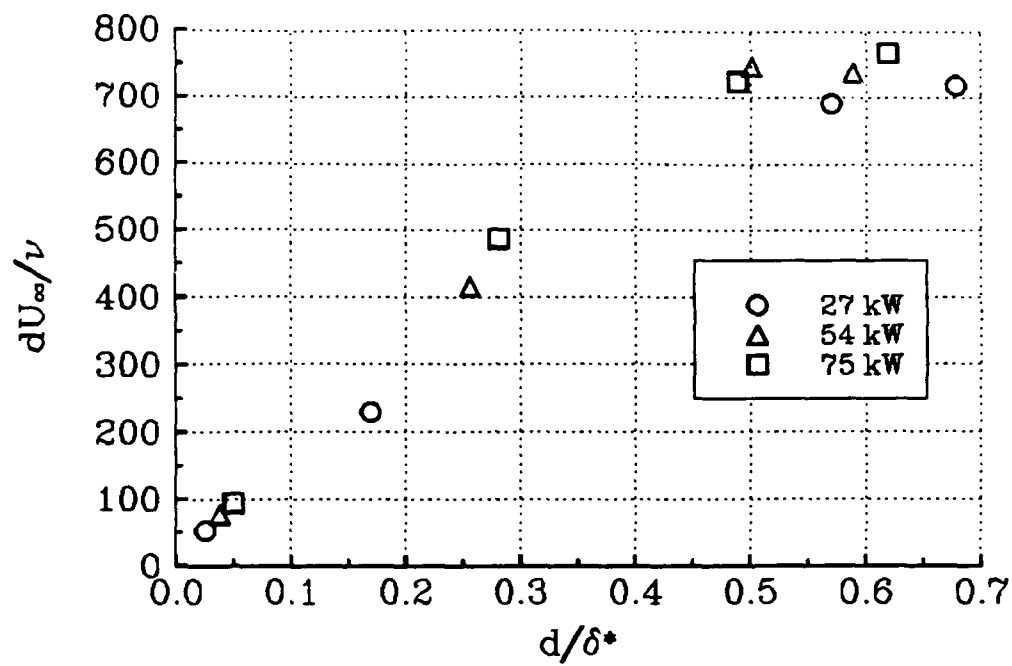


Fig. 2.6 Estimated critical conditions for turbulent spot generation on a heated laminar flow control body at three heating conditions from Lauchle, et al.(1986).

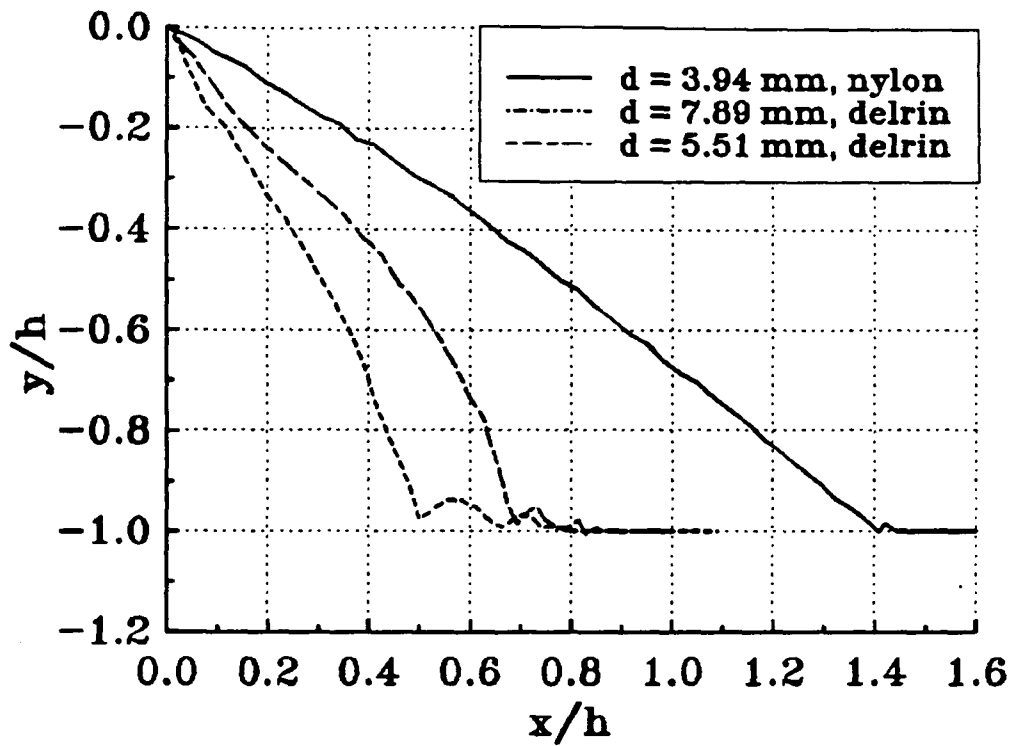


Fig. 2.7 Trajectories for particles #5, 7, and 9 on table 2.1. h is the distance the particle can fall from the release point.

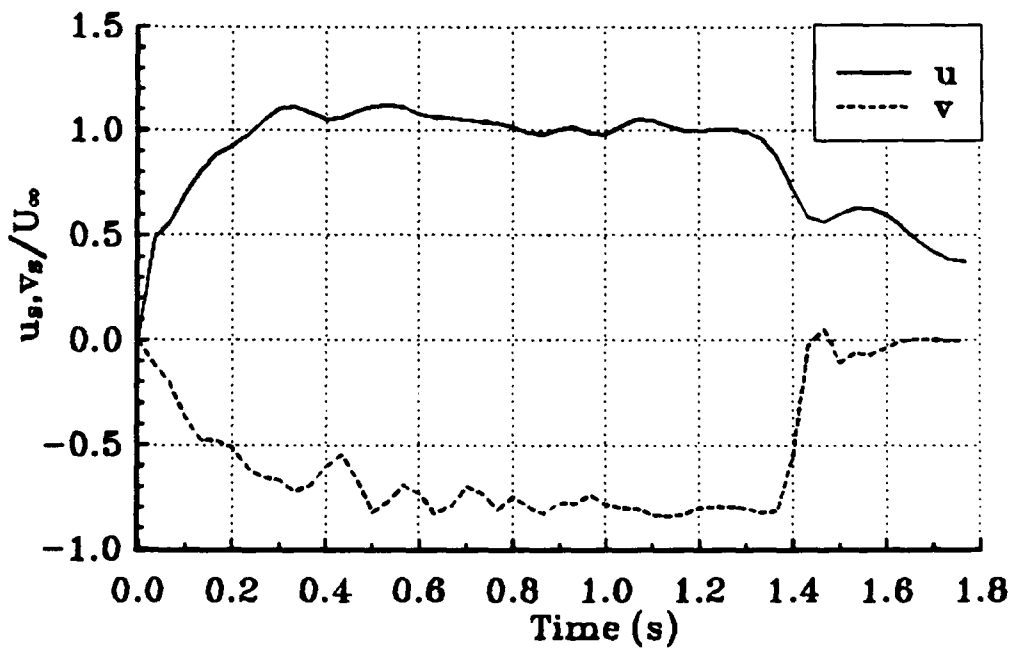


Fig. 2.8 Velocity history for particle #5 on table 2.1, nylon with $d = 3.94$ mm.

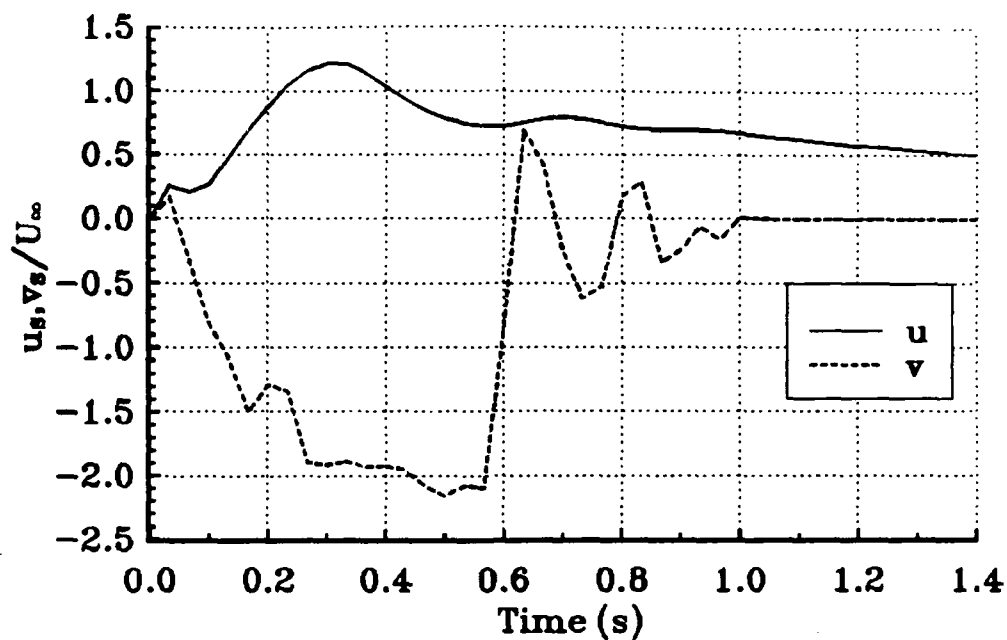


Fig. 2.9 Velocity history of particle #7 on table 2.1, delrin $d = 7.89$ mm.

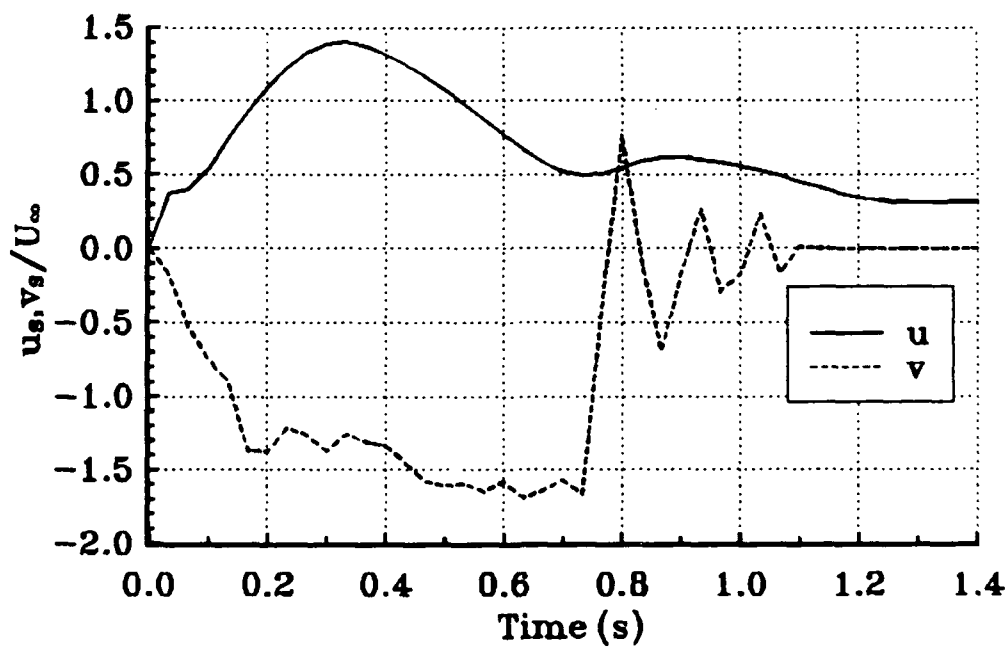


Fig. 2.10 Velocity history for particle #9 on table 2.1, delrin $d = 5.51$ mm.

Table 2.1 Impact conditions for all cases considered.

#	d (mm)	Material	d/δ at Impact	U_{im}/U_{∞}	V_{im}/U_{∞}	Re_{vis} at impact	Re_{vis} at impact	Estimated terminal velocity, v_t/U_{∞}	Spot on impact
1	7.89	Nylon	1.03	0.56	-0.96	1170	1350	-1.74	yes
2	6.31	Nylon	0.80	0.93	-1.19	1160	1470	-1.58	yes
3	5.51	Nylon	0.69	1.10	-0.99	837	1250	-1.55	yes
4	4.72	Nylon	0.58	0.94	-1.01	736	1060	-1.36	yes
5	3.94	Nylon	0.48	0.88	-0.82	496	726	-1.29	yes
6	3.12	Nylon	0.37	0.82	-0.77	371	542	-1.14	no
7	7.89	Delrin	1.16	0.73	-2.10	2550	2700	-2.97	yes
8	6.31	Delrin	0.86	1.12	-1.96	1900	2190	-2.58	yes
9	5.51	Delrin	0.77	0.49	-1.67	1410	1470	-2.38	yes
10	4.72	Delrin	0.64	0.92	-1.61	1170	1350	-2.29	yes
11	3.94	Delrin	0.54	0.93	-1.36	824	998	-1.95	yes
12	3.12	Delrin	0.42	0.95	-1.14	547	711	-1.59	no
13	7.94	Polystyrene	0.92	1.08	-0.81	987	1640	-0.98	yes
14	7.14	Polystyrene	0.82	0.98	-0.70	769	1320	-0.92	yes
15	6.35	Polystyrene	0.71	0.99	-0.66	646	1160	-0.85	yes
16	5.56	Polystyrene	0.62	1.03	-0.63	537	1030	-0.78	yes
17	4.76	Polystyrene	0.51	0.99	-0.43	317	791	-0.71	yes
18	3.97	Polystyrene	0.42	1.04	-0.54	330	787	-0.63	no
19	3.18	Polystyrene	—	0.96	-0.48	235	523	-0.54	no

PART III

Particle Trajectory and Transition Analysis

1. Introduction

The analytical and computational approach taken in this research program has been guided by the results of the parallel experiments. In the originally proposed technical approach it was planned to determine the trajectory of small freely-suspended particles. The wave-packets generated by these particles were to be simulated by moving point disturbances using the method developed by Breuer and Haritonidis (1990). In this method, the linearized equations of motion are transformed in space and marched in time. The physical flow field at any time is recovered by an inverse transformation. This approach avoids some of the difficulties of a normal mode or eigenfunction expansion technique in the description of the initial conditions. In the proposed calculations, both for the particle trajectory and wave-packet development, the basic flow was taken to be the Blasius boundary layer; however, the accompanying experiments indicated that the mean velocity defect, found in the particle's wake, was significant and played an important role in the determination of the initial disturbance and its subsequent development. Thus, it was decided to include this effect in the analysis and computations.

To this end, the stability of the wake of a body suspended in a boundary layer has been examined. This has involved several steps. First, the stability characteristics of a two-dimensional wake in a Blasius boundary layer have been examined. The role of the wake position, width, and velocity defect and the relative importance of viscous and inviscid or dynamic instability have been studied. As a second step, the same problem is being solved with a perturbation analysis. In this analysis, the small parameter is the strength of the mean shear that surrounds the wake. This analysis leads to the third problem: the stability of the wake of a sphere embedded in a shear flow. Through the use of a perturbation analysis this problem may be solved to leading order as an axisymmetric wake in a uniform flow. The effects of the shear flow are included at higher order as corrections to the axisymmetric problem. This approach avoids the need to solve a non-separable boundary problem for the stability of an axisymmetric wake in a plane shear flow. The results of the final part of this analysis provide the initial conditions for the development of a wave-packet generated by a particle suspended in or traversing a boundary layer. In addition, the problem is related closely to the experimental configuration and direct comparisons between the predictions and experiments will be possible.

Thus the analysis and computations include the following component prob-

lems:

- the calculation of the trajectory of freely-suspended particles in a laminar boundary layer.
- the prediction of the development of wave packets in a laminar boundary layer generated by disturbances at different locations.
- the calculation of the stability characteristics of a two-dimensional wake embedded in a laminar boundary layer with a full numerical and a perturbation analysis.
- The prediction of the stability of the wake of a sphere embedded in laminar boundary layer. and
- the development of wave packets generated by finite-size particles suspended in a laminar boundary layer.

The first two items above have been completed as has the numerical solution of the third item. These are described in this report. The remaining items are being completed as parts of the doctoral dissertation of Ms. Anupa Bajwa. The completion of this work is expected before December 1993. A copy of the thesis and any companion publications will be provided to the sponsor at that time. Thus the present report, though a final report for formal reporting purposes, does not represent the completion of our activities in this subject.

In the next section the particle trajectory calculations are presented. This is followed by a description of the wave-packet development from infinitesimally small particles suspended in a laminar boundary layer. The final section describes the stability characteristics of a wake embedded in a laminar boundary layer.

2. Particle Trajectory Calculations

A particle released into a fluid is acted on by various body and surface forces which result in the motion of the particle through the fluid. The trajectory of such particles is to be computed to determine the locations and velocities of spherical particles of various diameters, specific gravities and release velocities.

2.1. Second-order boundary layer theory

A freely suspended particle in a fluid is known to affect boundary layer transition. To determine the trajectory of such a particle, the basic flow-field (u, v) must be computed first. For a uniform freestream the first-order boundary layer theory gives a zero vertical velocity outside the boundary layer. Hence second-order boundary layer effects have to be taken into account, using the theory of matched asymptotic expansions (Van Dyke, 1975).

For a flat plate, the flow due to displacement thickness is given by the composite stream function $\psi(x, y; R)$:

$$\psi_{\text{composite}} = \frac{\sqrt{2x}}{\sqrt{R}} f_1 \left(\frac{\sqrt{Ry}}{\sqrt{2x}} \right) - \frac{\beta_1}{\sqrt{R}} \left[\Re \left\{ \sqrt{2(x + i y)} \right\} - \sqrt{2x} \right] \quad (1)$$

where R is the Reynolds number of the flow, and \Re denotes the real part of a complex function. Therefore the velocity components are given by

$$U = f_1' \left(\frac{\sqrt{Ry}}{\sqrt{2x}} \right) - \frac{\beta_1}{\sqrt{2R}} \Re \left\{ \frac{i}{\sqrt{x + i y}} \right\} \quad (2)$$

$$V = -\frac{1}{\sqrt{2Rx}} f_1 \left(\frac{\sqrt{Ry}}{\sqrt{2x}} \right) + \frac{y}{2x} f_1' \left(\frac{\sqrt{Ry}}{\sqrt{2x}} \right) + \frac{\beta_1}{\sqrt{2R}} \left[\Re \left\{ \frac{1}{\sqrt{x + i y}} \right\} - \frac{1}{\sqrt{x}} \right] \quad (3)$$

Hence the local shear components can be analytically obtained from,

$$\frac{\partial U}{\partial x} = -\frac{\sqrt{Ry}}{2x\sqrt{2x}} f_1'' \left(\frac{\sqrt{Ry}}{\sqrt{2x}} \right) + \frac{\beta_1}{2\sqrt{2R}} \Re \left\{ \frac{i}{(x + i y)^{3/2}} \right\} \quad (4)$$

$$\frac{\partial U}{\partial y} = \frac{\sqrt{Ry}}{\sqrt{2x}} f_1'' \left(\frac{\sqrt{Ry}}{\sqrt{2x}} \right) - \frac{\beta_1}{2\sqrt{2R}} \Re \left\{ \frac{i}{(x + i y)^{3/2}} \right\} \quad (5)$$

$$\begin{aligned} \frac{\partial V}{\partial x} = & -\frac{y}{4x^2} f_1' \left(\frac{\sqrt{Ry}}{\sqrt{2x}} \right) + \frac{1}{2x\sqrt{2xR}} f_1 \left(\frac{\sqrt{Ry}}{\sqrt{2x}} \right) - \frac{\sqrt{Ry}^2}{4x^2\sqrt{2x}} f_1'' \left(\frac{\sqrt{Ry}}{\sqrt{2x}} \right) \\ & + \frac{\beta_1}{\sqrt{R}} \left[\frac{1}{2x\sqrt{2x}} - \frac{1}{2\sqrt{2}} \Re \left\{ \frac{i}{(x + i y)^{3/2}} \right\} \right] \end{aligned} \quad (6)$$

From these equations, the convective derivatives for U and V are computed as

$$\frac{DU}{Dt} = U \frac{\partial U}{\partial x} + V \frac{\partial U}{\partial y} \quad \frac{DV}{Dt} = U \frac{\partial V}{\partial x} - V \frac{\partial U}{\partial x} \quad (7)$$

These quantities are required to compute the particle trajectory.

2.2. Trajectory calculations

Once the basic velocity field is computed, the particle trajectory can be determined as follows:

For a spherical particle p of radius a^* , the motion through a viscous fluid f is governed by the equation (Hoffman, 1988)

$$\begin{aligned} \rho_p^* V_p^* \frac{d\vec{V}_p^*}{dt^*} = & V_p^* (\rho_p^* - \rho_f^*) \vec{g}^* + \rho_f^* V_p^* \frac{d\vec{V}_p^*}{dt^*} + \frac{1}{2} \rho_f^* (\vec{V}^* - \vec{V}_p^*) |\vec{V}^* - \vec{V}_p^*| C_D A_p^* \\ & + \frac{1}{2} \rho_f^* [\vec{k} \times (\vec{V}^* - \vec{V}_p^*)] |\vec{V}^* - \vec{V}_p^*| \bar{C}_L A_p^* + \frac{1}{2} \rho_f^* V_p^* \left(\frac{d\vec{V}^*}{dt^*} - \frac{d\vec{V}_p^*}{dt^*} \right) + 6 A_p^* \sqrt{\frac{\rho_f^* \mu^*}{\pi}} \int_0^{t^*} \frac{\frac{d\vec{V}^*}{d\tau^*} - \frac{d\vec{V}_p^*}{d\tau^*}}{\sqrt{t^* - \tau^*}} d\tau^* \end{aligned} \quad (8)$$

where $V_p^* =$ particle volume $= \frac{4}{3} \pi a^{*3}$, $A_p^* =$ particle surface area $= 4 \pi a^{*2}$

The various terms in this equation represent:

LHS : Mass of the particle multiplied by its acceleration

RHS₁: Buoyant force on the particle

RHS₂: Force due to the pressure gradient in the fluid surrounding the particle

RHS₃: Drag force on the particle

RHS₄: Lift force on the particle

RHS₅: Force required to accelerate the added mass

RHS₆: Basset force on the particle, which dominates during the initial acceleration

The variables may be non-dimensionalized with respect to an arbitrary length scale L^* and the freestream velocity U_∞^* . Then, the particle trajectory equation becomes,

$$\frac{1}{2} + \frac{\rho_p}{\rho_f} \frac{d\vec{V}_p}{dt} = -\left(\frac{\rho_p}{\rho_f} - 1\right) \frac{1}{Fr} \vec{j} + \frac{3}{2} \frac{d\vec{V}}{dt} + \frac{3C_D}{8a} (\vec{V} - \vec{V}_p) |\vec{V} - \vec{V}_p| + \quad (9)$$

where Fr is the Froude number $= U_\infty^{*2}/g^* L^*$, R is the Reynolds number $= U_\infty^* L^* / \nu^*$, and \vec{I}_B is the Basset integral $= \int_0^t \left\{ \frac{d\vec{V}}{d\tau} - \frac{d\vec{V}_p}{d\tau} \right\} / \sqrt{t - \tau} d\tau$.

The system of equations for the trajectory is completed by specifying the position vector \vec{r}_p , where,

$$\frac{d\vec{r}_p}{dt} = \vec{V}_p \quad (10)$$

For flow along a horizontal flat plate the component equations are,

$$\frac{dx_p}{dt} = U_p \quad (11)$$

$$\frac{dy_p}{dt} = V_p \quad (12)$$

$$\left(\frac{1}{2} + \frac{\rho_p}{\rho_f}\right) \frac{dU_p}{dt} = \frac{3}{2} \frac{DU}{Dt} + \frac{3C_D}{8a}(U - U_p)\Delta q - \frac{3C_{Lx}}{8a}(V - V_p)\Delta q + \frac{9}{2a\sqrt{\pi}R} I_{Bx} \quad (13)$$

$$\begin{aligned} \left(\frac{1}{2} + \frac{\rho_p}{\rho_f}\right) \frac{dV_p}{dt} = & -\left(\frac{\rho_p}{\rho_f} - 1\right) \frac{1}{Fr} + \frac{3}{2} \frac{DV}{Dt} + \frac{3C_D}{8a}(V - V_p)\Delta q + \\ & + \frac{3C_{Ly}}{8a}(U - U_p)\Delta q + \frac{9}{2a\sqrt{\pi}R} I_{By} \end{aligned} \quad (14)$$

where

$$\Delta q = [(U - U_p)^2 + (V - V_p)^2]^{1/2} \quad (15)$$

$$I_{Bx} = \int_0^t \left[\frac{DU}{D\tau} - \frac{dU_p}{d\tau} \right] / \sqrt{t - \tau} d\tau \quad (16)$$

$$I_{By} = \int_0^t \left[\frac{DV}{D\tau} - \frac{dV_p}{d\tau} \right] / \sqrt{t - \tau} d\tau \quad (17)$$

For a given Reynolds number, radius, specific gravity, initial location and velocity of the particle, these equations may be integrated in time to determine its trajectory.

2.3. Lift and Drag Terms

It can be seen in Figure 1 that, for a typical case of a freely released particle, the lift and drag forces have parallel y -components and anti-parallel x -components. The drag coefficient depends on the particle Reynolds number $R_p = 2a\Delta q R$ as follows:

$$\log_{10} C_D = 1.6435 - 1.1242(\log_{10} R_p) + 0.1588(\log_{10} R_p)^2 \quad \text{where } 260 \leq R_p \leq 1500 \quad (18)$$

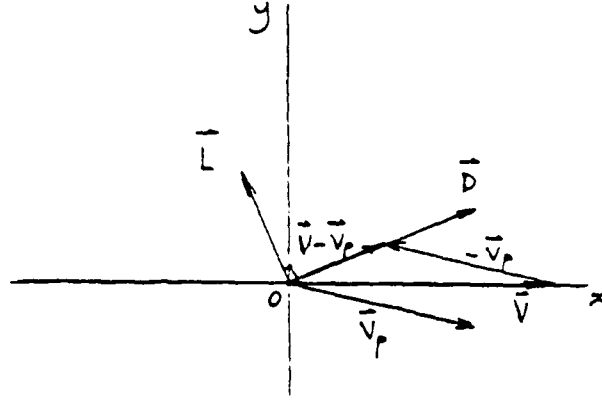


Figure 1: Lift and drag force vectors on a particle

This is the recommended drag correlation based on the standard drag curve (Clift, Grace and Weber, 1978). In the range of R_p expected in the present experiments, the lift coefficient depends only on the local fluid shear (Dandy and Dwyer, 1990). Since $\partial V/\partial x$ is very small throughout the flow regime, we set $C_{Lx} = 0$ and

$$C_{Ly} = 0.305 * (\partial U/\partial y)_p \quad \text{for } R_p \geq 50 \quad \text{where } (\partial U/\partial y)_p = \partial U/\partial y * a/\Delta y \quad (19)$$

2.4. The Basset Term

The final term on the right hand side of the equations of motion is the Basset history integral in which the past acceleration of the particle is included. The integrand of the Basset term is singular at the upper limit $t = \tau$. However, the Basset force can be included in the calculations using a method which eliminates the need to evaluate the integral explicitly. A change of variables, as suggested by Hoffman (1988), allows the trajectory equation to be written in a simple form as shown:

$$\tilde{A}_N = \tilde{B}_N + C_N \tilde{I}_{B_N} \quad \text{at time } t_N \quad (20)$$

where

$$\tilde{A} = \left\{ \frac{d\tilde{V}_p}{dt} - \frac{d\tilde{V}}{dt} \right\} \quad (21)$$

$$\vec{B} = - \left(\frac{\rho_p}{\rho_f} - 1 \right) \frac{2}{Fr} + 2 \frac{D\vec{V}}{Dt} + \frac{3C_D}{8a} (\vec{V} - \vec{V}_p) \Delta q + \frac{3C_L}{4a} [\vec{k} \times (\vec{V} - \vec{V}_p)] \Delta q \quad (22)$$

$$C = \frac{9}{a\sqrt{\pi R}} \quad (23)$$

$$\vec{I}_{B_N} = -\sqrt{t_N} \Delta\phi_2 \vec{A}_N - \sqrt{t_N} \vec{K} \quad (24)$$

and

$$\vec{K} = (\Delta\phi_2 + \Delta\phi_3) \vec{A}_{N-1} + (\Delta\phi_3 + \Delta\phi_4) \vec{A}_{N-1} + \dots + \Delta\phi_N \vec{A}_1 \quad (25)$$

with,

$$\Delta\phi = 1 - \frac{\tau}{t} \quad (26)$$

Thus \vec{I}_B can be eliminated and the particle acceleration at t_N can be found as follows:

$$\left(\frac{d\vec{V}_p}{dt} \right)_N = \vec{A}_N + \left(\frac{D\vec{V}}{Dt} \right)_N$$

where

$$\vec{A}_N = \frac{\vec{B}_N - C\sqrt{t_N}\vec{K}}{1 + C\sqrt{t_N}\Delta\phi_2} \quad (27)$$

We have used this trajectory formulation to conduct a parametric study of particle trajectories for a range of particle properties and release points to be considered in the experiments.

The (non-dimensional) parameters considered are

Reynolds number $R = 250,000$

Particle radius $a = 0.001, 0.002, 0.003, 0.004$

Density ratio $\rho_p/\rho_f = 1.05, 1.15, 1.25, 1.35$

Release location $x_p(1) = 0.1, \quad y_p(1) = 0.02, 0.1$

Release velocity $U_p(1) = 0.0, 0.5, 0.9, 1.2, \quad V_p(1) = 0.0$

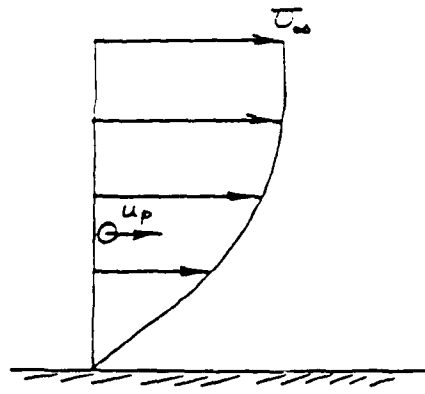
In the calculation of the trajectories for the various cases, it is observed that the buoyancy force and drag dominate the motion throughout the flow field, and the lift force is significant only in the boundary layer, where it reaches a maximum value of 8% of the drag. As expected from the analysis of Saffman (1965), for a particle moving slower than the fluid over a stationary wall the lift tends to push the particle away from the wall. In the case of plate moving through a stationary fluid, the situation could be reversed depending on the relative motion between the particle and the fluid (Fig. 2). This is best understood when viewed from the frame of reference of the particle. The added mass term and the Basset force are found to not be significant in the calculations, since the density ratio does not tend to zero for the case of solid spheres moving through a fluid. These forces would be quite significant, for example, in the calculation of a bubble trajectory. Hence, for the particle trajectories (Figs.3-6), the Basset term is omitted from the calculations in order to simplify them.

Fig. 3 shows the variation of the trajectories of freely released particles for different particle densities. Fig. 4 shows the variation with particle radius. Figures 5 and 6 show the corresponding time variation of the particles' vertical velocity. As expected, the smaller and lighter particles travel through a greater horizontal distance and impact the plate further downstream than the bigger and heavier ones. Fig. 5 shows that the lighter particle reaches a smaller terminal velocity and that it takes longer to reach it, implying that its acceleration vertically downwards is of a smaller magnitude. This is because its body force is smaller. When the particle radius is varied, as in Fig. 6, it is observed that the smaller particle reaches a lower terminal velocity and that it takes less time to do so than the bigger particles. This means that its drag force increases rapidly in time to balance its weight. This is because the drag coefficient C_D is higher for smaller particles, initially, and it increases in time as R_p decreases.

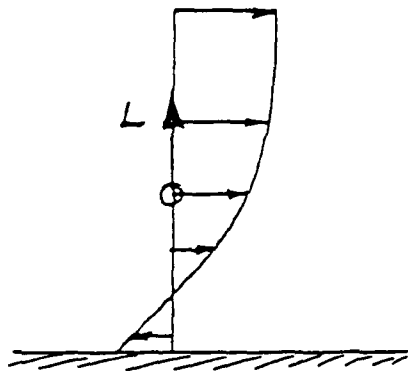
3. Development of wave packets in a laminar boundary layer

A particle disturbs the flow as it moves along its trajectory. So the next step is to compute the wave packet development from this particle point-source. To do this a linear, inviscid stability analysis is used, for a stationary particle to start with. There are two different ways to approach this problem — to follow the evolution of the disturbance in time or to compute the normal modes in the frequency domain and superimpose them.

a) Flow over a stationary wall

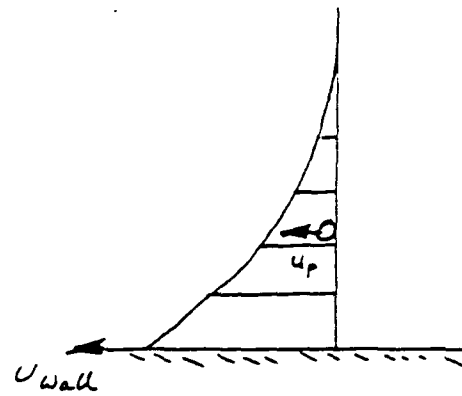


Laboratory frame of reference

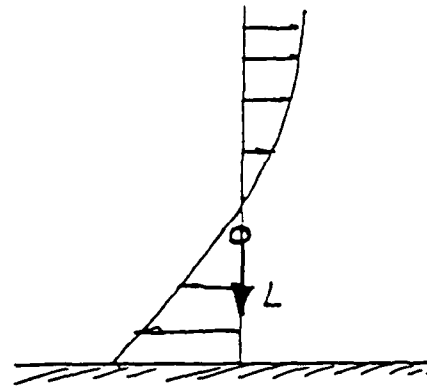


Particle frame of reference

b) Motion of wall through a still fluid



Laboratory frame of reference



Particle frame of reference

Figure 2: Lift force on a particle due to shear

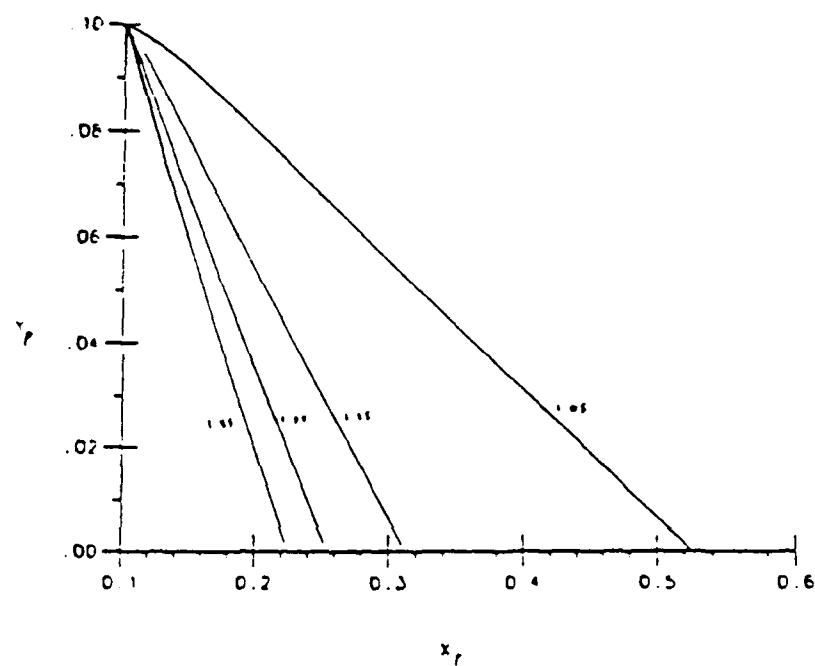


Figure 3: Trajectories of particles with different specific gravities released from rest

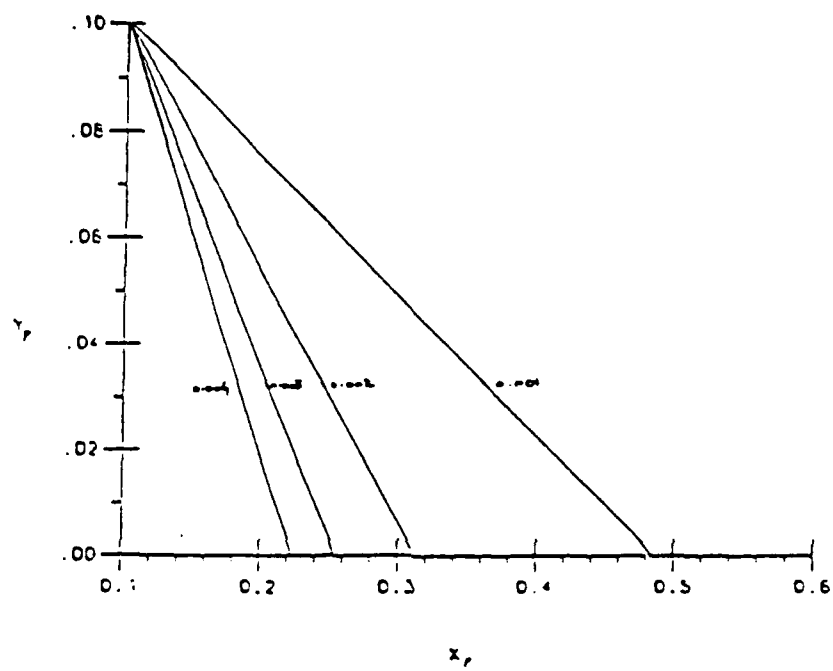


Figure 4: Trajectories of particles with different sizes released from rest

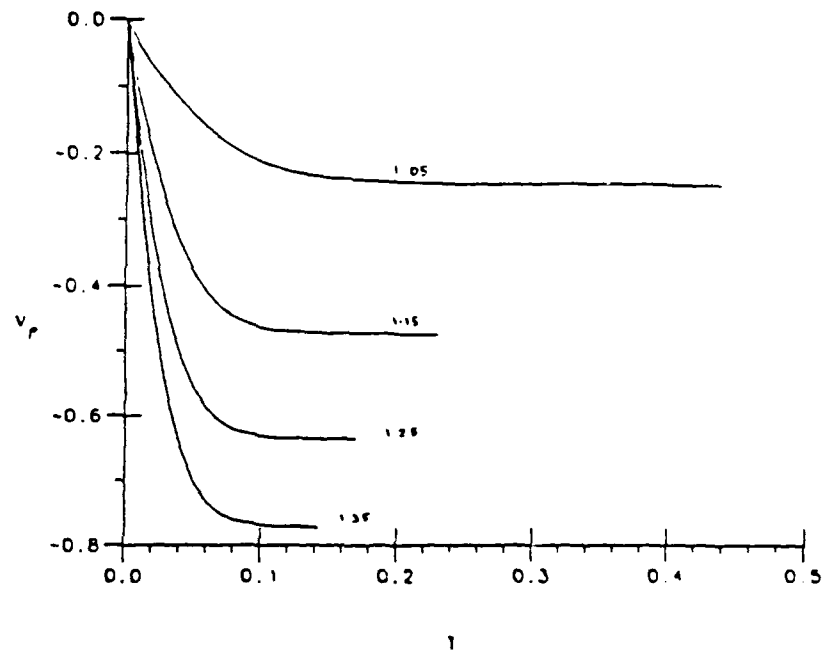


Figure 5: Time variation of the vertical velocity of particles with different specific gravities

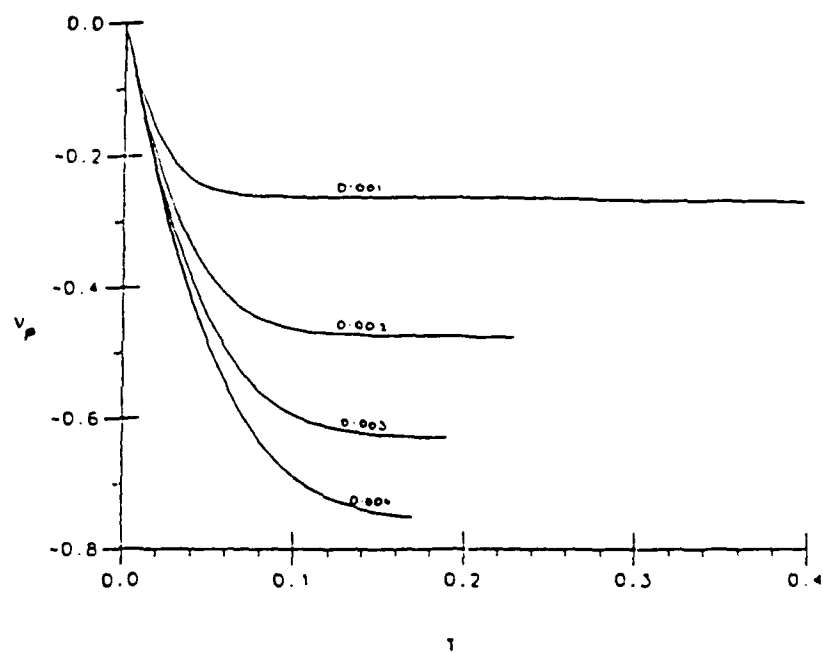


Figure 6: Time variation of vertical velocity of particles with different sizes

A wave packet generated by an impulse disturbance causes oscillations in the flow as it spreads out while travelling downstream (Gaster and Grant, 1975). This initial disturbance generates all possible modes and the wave packet forms through selective amplification and interference of the most unstable waves. This phenomenon can be simulated numerically using a linear stability analysis (Gaster, 1975). The wave packet is reproduced computationally by linearly combining spatially unstable modes and summing over all wavenumbers and frequencies.

To study the initial value problem for any general disturbance in a viscous flow, the Orr-Sommerfeld equation must be solved. The eigensolutions to this equation are discrete modes which form a complete system for bounded flows. However, for boundary layer flows with a semi-infinite domain, there is also a *viscous* continuous spectrum (Gustavsson, 1978). As the Reynolds number increases, one mode approaches the inviscid Rayleigh mode while the higher modes tend towards a neutrally stable inviscid continuum. For three-dimensional disturbances in a piecewise linear boundary layer the vertical velocity has two parts – one is a dispersive part which comes from the Rayleigh equation solution, and the other is a convected part from inviscid continuous spectrum. Also, there is a *permanent scar* caused by the fact that the streamwise velocity does not vanish at large times. It is advected at the local mean velocity. Most three-dimensional disturbances show a linear increase in energy with time. This behaviour is different from the one predicted by two-dimensional stability analysis that transient modes decay.

Time-evolution of a small disturbance can be computed using Fourier transform methods. Results show that transient modes do not decay as rapidly as dispersive modes (Henningson, 1988). This method is extended to the Blasius boundary layer by Breuer and Haritonidis (1990). Both numerical and experimental results indicate the formation of linearly unstable wave packets, and of dominant transients which, for weak initial disturbances, eventually decay due to viscous effects. For weak disturbances a linear stability analysis is applicable and this approach is discussed in detail in the next section. For strong disturbances direct numerical simulation is necessary. For these high-amplitude disturbances the transients do not decay. Non-linear effects lead to the direct breakdown of the disturbance to a turbulent spot, bypassing the wave packet stage.

For low-amplitude initial disturbances in a flat-plate boundary layer at moderate Reynolds numbers, the route to transition is through a wave packet breakdown which occurs over a broad spatial domain (Tso, Chang and Blackwelder, 1990). Since the growing wave packet moves significantly slower than the diminishing

transient, hump-like disturbance, there is little interaction between them and only the wave packets are responsible for transition. With strong initial disturbances however, the transition mechanism is via the growth of the *transients* into a turbulent spot. We will consider only weak disturbances in modeling the effect of the particles.

4. Numerical simulation of wave packets

Gaster's theoretical linear model successfully simulates his experimentally-observed wave packet excited by a localized pulse at the wall. While Gaster's simple linear model works well for calculations at a *fixed* height above the plate, it cannot account for a movement of the source in the vertical direction. A recent method developed by Breuer and Haritonidis (1990) employs a time-marching technique to compute the development of wave packets from small-amplitude disturbances. This approach does capture the dependence of the wave packet on the y -location of the source of the disturbance. This is exactly what is required to study the effect of a particle disturbing a boundary layer as it moves through it. We use Breuer's analysis in the development of our computational scheme. To verify the code we compare results for an initial disturbance consisting of a pair of counter-rotating vortices. This initial disturbance can then be modified to model the particle moving across the boundary layer.

The equation governing linear, inviscid, small disturbances for the vertical velocity is the Rayleigh equation

$$\left(\frac{\partial}{\partial t} + i\alpha U\right)\left(\frac{\partial^2}{\partial y^2} - k^2\right)\tilde{v} - i\alpha U'' \tilde{v} = 0 \quad (28)$$

where $k^2 = \alpha^2 + \beta^2$. Here α, β are the streamwise and spanwise wavenumbers respectively. \tilde{v} is the transformed vertical velocity perturbation obtained by taking a Fourier transform in x and z of the physical fluctuation quantity v :

$$\tilde{v}(y, t; \alpha, \beta) = \int_{-\infty}^{\infty} \int_{-\infty}^{\infty} v(x, y, z, t) \exp[-i(\alpha x + \beta z)] dx dz \quad (29)$$

The laminar boundary layer profile is used for the basic flow $U(y)$. The velocity fluctuations perpendicular to and along the wavefront, \tilde{u}_1 and \tilde{w}_1 respectively, are related to \tilde{v} by

$$\left(\frac{\partial}{\partial t} + i\alpha U\right)\tilde{u}_1 = \frac{i}{k}\left(\frac{\partial}{\partial t} + i\alpha U\right)\tilde{v}_y \quad (30)$$

$$\left(\frac{\partial}{\partial t} + i\alpha U\right)\hat{w}_1 = -\frac{\beta}{k}U''\hat{v} \quad (31)$$

The two physical velocity perturbations are retrieved from these by

$$\hat{u} = (\alpha\hat{u}_1 + \beta\hat{w}_1)/k \quad (32)$$

$$\hat{w} = (\beta\hat{u}_1 - \alpha\hat{w}_1)/k \quad (33)$$

The Rayleigh equation is rewritten as a system of two equations

$$\frac{\partial \nabla^2 \hat{v}}{\partial t} = i\alpha(U''\hat{v} - U\nabla^2 \hat{v}) \quad (34)$$

$$\nabla^2 \hat{v} = \left(\frac{\partial^2}{\partial y^2} - k^2\right)\hat{v} \quad (35)$$

These equations are marched forward in time using a Crank-Nicholson scheme and a second-order accurate finite difference for the y -derivative, for which the discretized equations are

$$\nabla^2 \tilde{v}_j^{n+1} - \nabla^2 \tilde{v}_j^n = \frac{i\alpha\Delta t}{2}(U_j''(\tilde{v}_j^{n+1} + \tilde{v}_j^n) - U_j(\nabla^2 \tilde{v}_j^{n+1} + \nabla^2 \tilde{v}_j^n)) \quad (36)$$

$$\nabla^2 \tilde{v}_j^n = \frac{\tilde{v}_{j+1}^n - 2\tilde{v}_j^n + \tilde{v}_{j-1}^n}{\Delta y^2} - k^2 \tilde{v}_j^n$$

where n refers to the current time-step and j refers to the vertical grid. In vector form, at time step n a matrix equation is obtained,

In vector form, at time step n a matrix equation is obtained

$$(\mathbf{I} + i\mathbf{R})\mathbf{D}\tilde{\mathbf{v}}^{n+1} = (\mathbf{I} - i\mathbf{R})\mathbf{D}\tilde{\mathbf{v}}^n + i\mathbf{S}(\tilde{\mathbf{v}}^{n+1} + \tilde{\mathbf{v}}^n) \quad (37)$$

where

$$\tilde{\mathbf{v}}^n = [\tilde{v}_j^n]^T \quad j = 1, 2, \dots, J \quad (38)$$

$$\mathbf{R} = \frac{\alpha\Delta t U_j}{2}\mathbf{I} \quad (39)$$

$$\mathbf{S} = \frac{\alpha\Delta t U_j''}{2}\mathbf{I} \quad (40)$$

\mathbf{I} is the identity matrix and \mathbf{D} is the tridiagonal matrix associated with the Laplacian derivative in the normal direction.

Therefore the explicit form for the velocity at the $(n + 1)$ th time-step is

$$\tilde{\mathbf{v}}^{n+1} = (\mathbf{D} + i(\mathbf{RD} - \mathbf{S}))^{-1}(\mathbf{D} - i(\mathbf{RD} - \mathbf{S}))\tilde{\mathbf{v}}^n \quad (41)$$

Similarly for \tilde{u}_1 the matrix equation is

$$(\mathbf{I} + i\mathbf{R})\tilde{\mathbf{w}}_1^{n+1} = (\mathbf{I} - i\mathbf{R})\tilde{\mathbf{w}}_1^n - \mathbf{T}(\tilde{\mathbf{v}}^{n+1} + \tilde{\mathbf{v}}^n) \quad (42)$$

where

$$\mathbf{T} = \frac{\Delta t \beta U'}{2k} \mathbf{I} \quad (43)$$

This is also integrated forward in time using the current values for $\tilde{\mathbf{v}}^n$ and $\tilde{\mathbf{v}}^{n+1}$. The quantity \tilde{u}_1 is obtained simply from

$$\tilde{u}_1 = \frac{i}{k} \tilde{v}_y \quad (44)$$

As a test case for our code, we use the initial conditions of Breuer et al which simulate a localized, impulsive disturbance in the form of two pairs of counter-rotating longitudinal vortices, represented by the (two-dimensional) stream function

$$\Psi = \bar{x}\bar{z}\bar{y}^2 \exp(-\bar{x}^2 - \bar{y}^2 - \bar{z}^2) \quad (45)$$

where $\bar{x}, \bar{y}, \bar{z}$ are the three Cartesian coordinates scaled by appropriate scaling factors

$$\bar{x} = x/l_x; \quad \bar{y} = y/l_y; \quad \bar{z} = z/l_z \quad (46)$$

From this stream function, the initial disturbance velocities are computed as

$$v = \frac{\partial \Psi}{\partial z}; \quad w = -\frac{\partial \Psi}{\partial y} \quad (47)$$

At $t = 0$ the center of the disturbance is located at $x = 0, z = 0$. Since all the matrices are tridiagonal, the system of two matrix equations is easily integrated forward in time. Furthermore, for fixed α, β and Δt the matrices need to be evaluated and combined only once. Hence time-marching for $\tilde{\mathbf{v}}$ at the next time-step reduces to a simple multiplication of a matrix by the vector $\tilde{\mathbf{v}}$ at the current time step. This speeds up the computations for each pair of (α, β) . 64 modes are used for α and 32 for β . These are sufficient to produce smooth contour plots for the various velocity fluctuations, obtained at any desired time t by taking the (inverse) fast Fourier transform of the transformed velocities to convert the

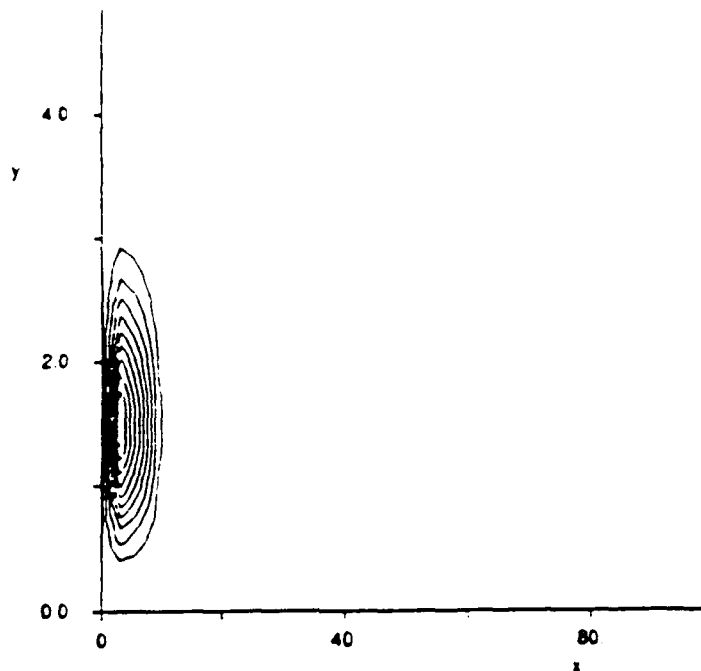


Figure 7: Contours of initial vertical velocity in the xy -plane at $z = 0$. Contour spacing is .1 of the maximum initial v -perturbation

fluctuations back to physical space. This is done at each y -location to get complete picture across the boundary layer. Considerable effort has been made to use optimal two-dimensional fast Fourier transform routines in the complex domain and efficient matrix inversion routines, since these are used at each y -location in the boundary layer. The routines are adapted from Press et al (1986).

The evolution of the vertical velocity disturbance is shown in Figs. 7-11. The initial disturbance of two counter-rotating streamwise vortices develops into one having a wave packet part and a transient part. The wave packet nature is seen in the xz plane and the transient part is clearly seen in the xy plane where the patch of low-speed fluid pulls ahead of the rest of the disturbance.

Thus wave packet development can be computed using linear stability theory. A simple, computationally-efficient time-marching scheme is sufficient to study evolution of fluctuation velocities in the spectral domain. Computations for weak

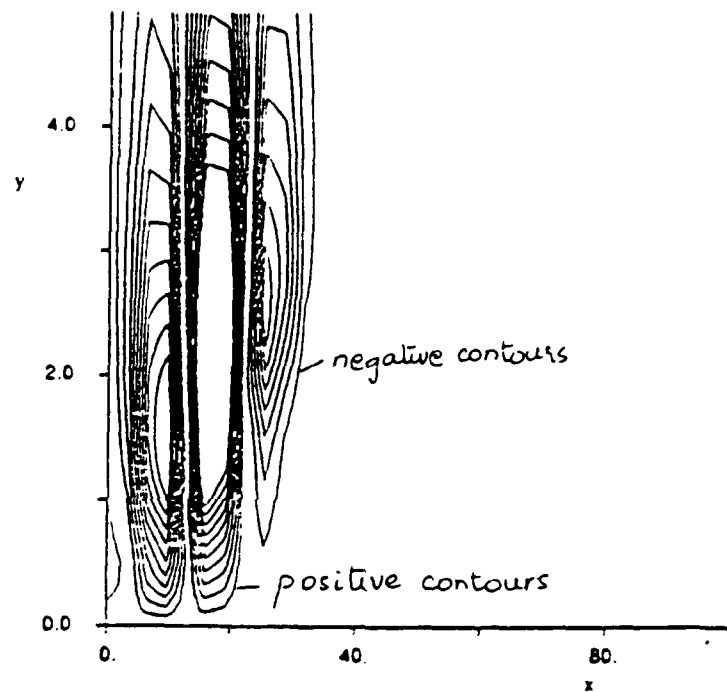


Figure 8: Contours of the vertical velocity in the xy -plane at $z = 0$ at time $t = 25$. Contour spacing is .1 of the maximum initial v -perturbation

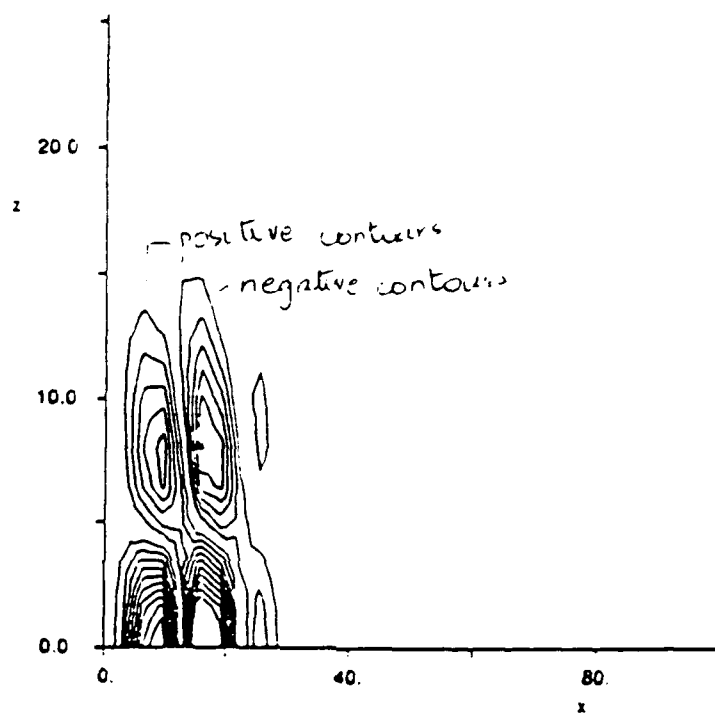


Figure 9: Contours of the vertical velocity in the xz -plane at $y = 1.478$ at time $t = 25$. Contour spacing is .1 of the maximum initial v -perturbation

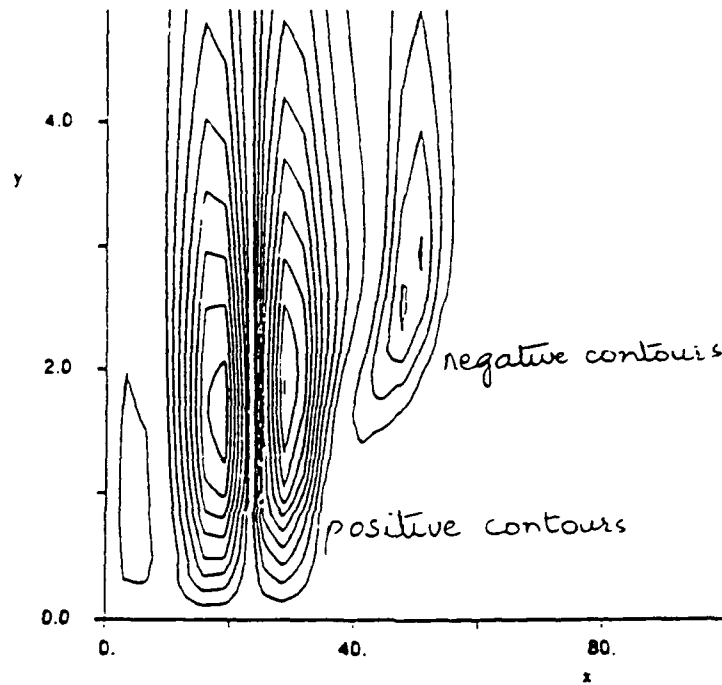


Figure 10: Contours of the vertical velocity in the xy -plane at $z = 0$ at time $t = 50$. Contour spacing is .1 of the maximum initial v -perturbation

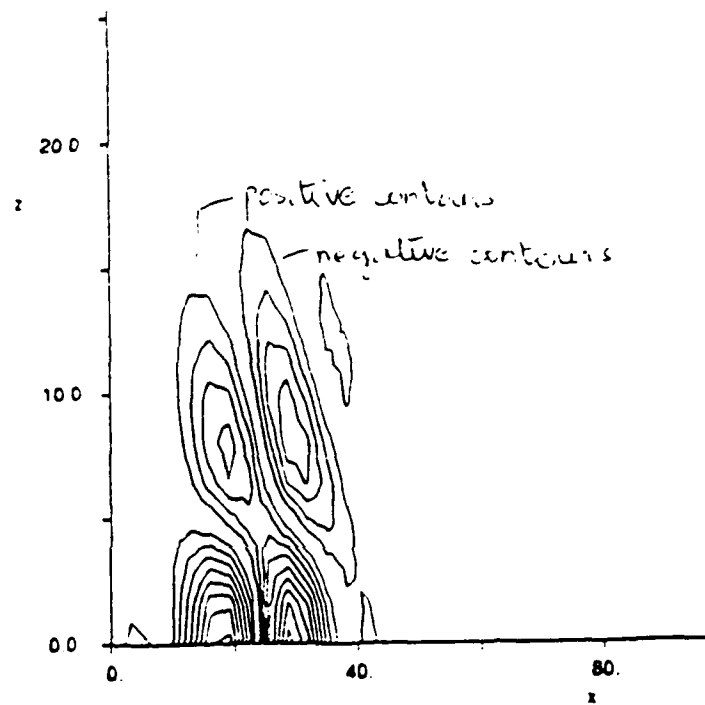


Figure 11: Contours of the vertical velocity in the xz -plane at $y = 1.478$ at time $t = 50$. Contour spacing is .1 of the maximum initial v -perturbation

initial disturbances can be extended to include moving sources, such as particles in a boundary layer. For a moving particle, the wave packets generated at each y -location can be computed individually and then superposed linearly to get the entire flow field, which is possibly a turbulent spot. Work is in progress on how exactly to model the particle as an initial disturbance. The model is based mostly on experimental results available in the literature.

4.1. Initial disturbance due to a particle

To model a freely-suspended particle as an initial disturbance, we must identify the flow pattern immediately downstream of the particle in the boundary layer flow. We model a spherical particle to start with. Vortices shed from spheres are basically of two types: vortex tubes and large-scale hairpin vortices. A recent experimental study by Sakamoto and Haniu (1990) concludes that which type of vortex is shed depends strongly on the Reynolds number of the flow. For our range of Reynolds numbers (based on particle diameter and freestream velocity) the primary vortex pattern is that of hairpin-like vortices of known Strouhal number. These are caused by the progressive wave motion of the wake and are shed periodically. The amplitude is irregular and the direction of shedding oscillates intermittently. This may be due to an imbalance in the supply, storage and emission of energy within the vortex formation region. The length scale of these vortices can be determined based on flow velocity and shedding frequency. For Reynolds numbers higher than 700 the hairpin vortices become turbulent and, in addition to these, small vortex loops are shed. Some of the loops move downstream and intertwine with the hairpin vortices.

To start with, we will model the hairpin vortices behind the sphere as a counter-rotating streamwise vortex pair. For a particle tethered to the wall, these vortices are generated periodically at the same location in space. So, in our linear stability calculation of the wave packet we can simply superpose the fluctuations due to several initial disturbances staggered in time. The calculations need to be performed only once, and thereafter we can simply shift the time-origin to include the periodically-shed vortices. The strength of the initial disturbance changes in time. However, the vertical velocity fluctuation can be scaled out in the spectral domain. So it is necessary to compute the evolution of only a known strength and a unit strength. Then for any other values of initial disturbance, the time-evolution of the fluctuation can be obtained by a simple scaling.

For a moving particle, the location of the initial disturbance changes in time. Hence the calculations have to be performed using each vortex shed as an initial

condition at a given point on the particle trajectory, and then the wave packets can be superposed. The computational box should be long enough to include the effects of the first few wave packets convected downstream while the next few are incipient near the particle.

The initial conditions due to vortex shedding are periodic in time. However, we cannot simply take a Laplace transform in time to include all the vortices because the particle itself is moving in the vertical direction - the direction of integration of the stability equation. Hence the computations will be carried out in the time-marching scheme outlined above.

4.2. Further work

Once the moving particle is modeled appropriately, the wave packet computations have to be interfaced with the trajectory calculations. The end result sought is an efficient algorithm for computing the disturbance due to a moving particle of any size and specific gravity. Disturbances due to two or more particles may also be computed and the various wave packets may be superposed to find the resulting disturbance. If necessary, the effect of nonspherical particles can also be studied. Since it uses a linear analysis, this computational method is limited in that it cannot handle nonlinear interactions between the particle and the boundary layer flow. To study such interactions of strong disturbances it may be necessary to use a direct numerical simulation technique, which is outside the scope of this project. In the next section we consider the stability of a wake in a two-dimensional boundary layer. This analysis, and its extension to three-dimensional wakes, will provide insight into the selection of initial conditions and the influence of the particle's wake on the development of the wave packet it triggers.

5. Stability of a Wake in a Boundary Layer

Hall (1967) performed an experiment to determine the mechanism of transition due to bluff bodies suspended in a boundary layer. Transition appeared to depend on the stability characteristics of the wake rather than on the stability characteristics of the boundary layer. For spheres at different heights from the wall the boundary layer responded differently. In this section we examine how the location of a wake in a boundary layer affects the stability of the entire flow. A spatial stability analysis is used. Three parameters that characterize the wake are considered: the wake velocity defect, the wake width and the wake height above the

wall.

5.1. Background

The earliest stability calculations for a two-dimensional wake were performed by Hollingdale (1940) and McKoen (1956). They used analytical methods to find the eigenfunctions for neutral disturbances for large Reynolds number wakes. Sato and Kuriki (1961) reported an experimental and a numerical study of an artificially-excited transition of a wake behind a thin flat plate. Based on their observations, they classified the transition zone into three subregions:

1. a linear region, where the two-dimensional, sinusoidal velocity fluctuations amplify exponentially downstream, and different frequencies are damped or amplified independently
2. a nonlinear region, where the growth rates deviate from being exponential due to nonlinear effects, and different spectral components may interact, and
3. a three-dimensional region, where the disturbance is no longer periodic, and spanwise fluctuations ultimately cause the wake to become turbulent.

In Sato and Kuriki's numerical approach, a parallel-flow approximation with a Gaussian mean velocity distribution was used to describe the wake. The Rayleigh equation was solved for temporally-amplified disturbances, to obtain the eigenvalues α and c . To compare the calculated amplification rates αc , with experimental observations, the temporal results were transformed into spatial growth rates $\alpha c/c_r$ using the phase velocity of the waves. Sato and Kuriki's calculations and experimental data agreed well in the linear region. This confirms that a linear stability analysis is indeed applicable to the wake when the disturbances are small.

Mattingly and Criminale (1972), noted that a *spatial* stability analysis gives a more realistic picture of flow stability. They performed a stability analysis, in which both frequency and wavenumber are complex, to study the near-wake region. They compared their calculations with experimental observations for the wake of a thin airfoil in a water tank. They studied both mode I (sinuous mode) with symmetrical vertical velocity disturbances and mode II (varicose mode) with anti-symmetrical ones. They found that mode I disturbances are predominant in the wake. They also found that the von Kármán vortex street formed behind streamlined bodies has its origins in the near-wake region. This is in contrast to

the proposal by Sato and Kuriki that the vortex street forms in the non-linear region when a single row of spanwise vortices breaks up into two rows away from the centerline. This may be connected to the absolute instability of wakes in the very near-wake region.

The terms absolute and convective instability describe the impulse response of a flow. If an impulsive small disturbance grows exponentially at the source location in time the flow is termed absolutely unstable. For a convectively unstable flow the transient is convected away from the source and leaves the flow ultimately undisturbed. Huerre and Monkewitz (1985) demonstrated the distinction between absolute and convective instability in inviscid, parallel shear flows by studying the branch-point singularities of the dispersion relation for complex frequencies and wavenumbers. According to the Briggs-Bers criterion, developed in the study of plasma instabilities, a flow is convectively unstable when the branch point singularities are in the lower half complex-frequency plane. Huerre and Monkewitz (1988) also numerically verified the Chomaz, Huerre and Redekopp (1988) model for the sequence of transition in the cylinder wake. The critical Reynolds number for transition from stability to convective instability (based on the cylinder diameter and freestream velocity) is 5, and the first local absolute instability appears at a Reynolds number of 25. As the Reynolds number is further increased to 47 a global temporal instability sets in and leads to the formation of the Kármán vortex street with a shedding frequency close to the linear global response frequency.

In the present study we consider the convective stability of a two-dimensional wake embedded in a boundary layer. The strength and location of the wake are varied. We examine whether the flow stability is controlled by the wake or the boundary layer as a function of changes in the wake properties.

5.2. Governing Equations

We assume the basic flow to be two-dimensional and a function of y only. The disturbance velocities \tilde{u} and \tilde{v} and kinematic pressure \tilde{p} are functions of x , y and t , and are small compared to the basic flow, so that the equations of motion can be linearized. On nondimensionalising the equations (using the freestream velocity U_∞ and a characteristic length such as the wake half-width), and subtracting the mean flow, we get the equations governing the disturbances

$$\tilde{u}_x + \tilde{v}_y = 0 \quad (48)$$

$$\hat{u}_t + U\hat{u}_x + U_y\hat{v} = -\hat{p}_x + \frac{1}{R}(\hat{u}_{xx} + \hat{u}_{yy}) \quad (49)$$

$$\hat{v}_t + U\hat{v}_x = -\hat{p}_y + \frac{1}{R}(\hat{v}_{xx} + \hat{v}_{yy}) \quad (50)$$

Following the conventional normal mode approach in hydrodynamic stability theory, we seek complex solutions of the form

$$\hat{u}(x, y, t) = u(y)e^{i(\alpha x - \omega t)} \quad (51)$$

$$\hat{v}(x, y, t) = v(y)e^{i(\alpha x - \omega t)} \quad (52)$$

$$\hat{p}(x, y, t) = p(y)e^{i(\alpha x - \omega t)} \quad (53)$$

where

$$\hat{u} = \frac{1}{2}(\hat{u} + \hat{u}^*) \quad \hat{v} = \frac{1}{2}(\hat{v} + \hat{v}^*) \quad \hat{p} = \frac{1}{2}(\hat{p} + \hat{p}^*) \quad (54)$$

and the superscript * denotes complex conjugate.

Eliminating the pressure term and using the continuity equation leads to a single differential equation for $v(y)$: the Orr-Sommerfeld equation.

$$[(i\alpha R)^{-1}(D^2 - \alpha^2)^2 - (U - \frac{\omega}{\alpha})(D^2 - \alpha^2) + D^2 U]v = 0 \quad (55)$$

where D denotes d/dy . If the viscous terms are neglected we obtain the Rayleigh equation

$$(U - \frac{\omega}{\alpha})(D^2 v - \alpha^2 v) - D^2 U v = 0 \quad (56)$$

with boundary conditions

$$v(0) = 0, \quad Dv(y) + \alpha v(y) \rightarrow 0, \text{ as } y \rightarrow \infty \quad (57)$$

where $\alpha = \alpha_r + i\alpha_i$ is the wave number and ω is the frequency of the disturbance.

For a two-dimensional Gaussian wake in a flat-plate boundary layer, the mean velocity distribution is the superposition of the two profiles

$$U(y) = U_b(y) - u_w \exp(-a_w(y - y_w)^2) \quad (58)$$

where $U_b(y)$ is the Blasius profile, u_w is the wake centerline defect, a_w is the wake width parameter and y_w is the wake centerline location.

5.3. Method of Solution

The Rayleigh equation and the boundary conditions constitute a homogeneous boundary value problem. To determine a solution we use a shooting technique. The mean profile is found by integrating the third-order Blasius equation as well as the second-order Rayleigh equation using an adaptive step-size Runge Kutta routine [Press et al (1986)]. For a spatial stability calculation, the frequency ω is real and the wavenumber α is complex.

For a given ω and a specified set of wake parameters, the system of five first-order, ordinary differential equations is integrated from the wall to the outer edge of the boundary layer for two guessed values of α . A (complex) secant method is used to obtain subsequent guesses for α till convergence [Press et al (1986)]. To obtain a reasonable initial guess for the eigenvalue α , we use the results of Sato and Kuriki with the wake outside the boundary layer ($u_w = 0.7$, $a_w = 0.693$, $y_w = 6.0$) and move the wake down, in small steps, to the desired wake parameters. Typical wake parameters used in this study are $u_w = 0.5$, $a_w = 3.243$, $y_w = 2.4$ (Figure 12).

Once eigenvalues α are obtained for a range of ω , a plot of the spatial growth rate α_i versus the frequency shows the most unstable frequency, that is, the frequency with the most negative α_i . For this mode, eigenfunctions $v(y)$ and $u(y)$ (from continuity) can be calculated. The energy production term μ_1 can be computed from the Reynolds stress term $-\overline{uv}$

$$\mu_1 = -\overline{uv}U_y = -\frac{1}{2}\Re(uv^*)U_y \quad (59)$$

This term is a measure of the energy transferred from the mean flow to the disturbances.

5.4. Results and Discussion

To study the effect of wake parameters on the stability characteristics we first consider Sato and Kuriki's wake added to the boundary layer profile far from the wall: $u_w = 0.7$, $a_w = 0.7$, $y_w = 6.0$. An inviscid analysis is performed first.

5.4.1. Wake Velocity Defect

For a fixed a_w and y_w , as the wake defect u_w is decreased from 0.7 to 0.5, the rates of amplification decrease for all frequencies, since, in the limit of no wake, the Blasius profile is stable in the inviscid analysis.

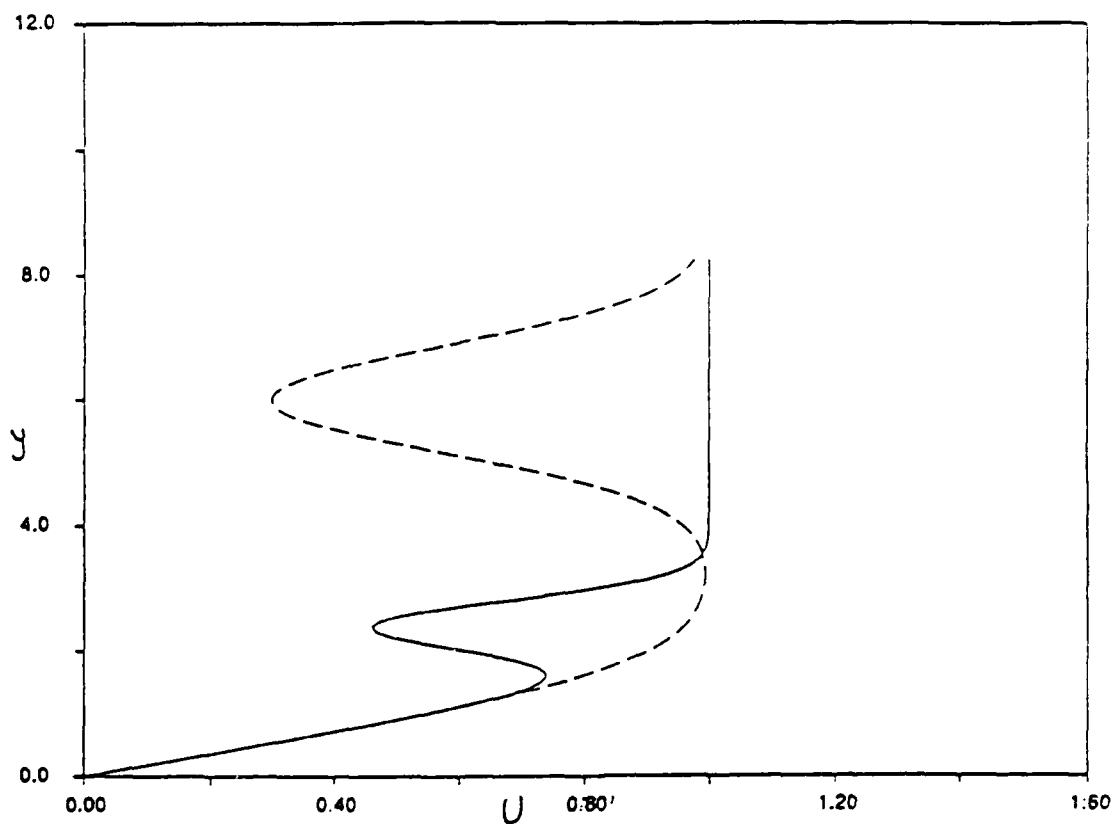


Figure 12: Mean velocity profiles. The solid line shows a typical wake at $y_w = 2.4$, and the dashed line is Sato and Kuriki's (1961) wake located outside the boundary layer at $y_w = 6.0$

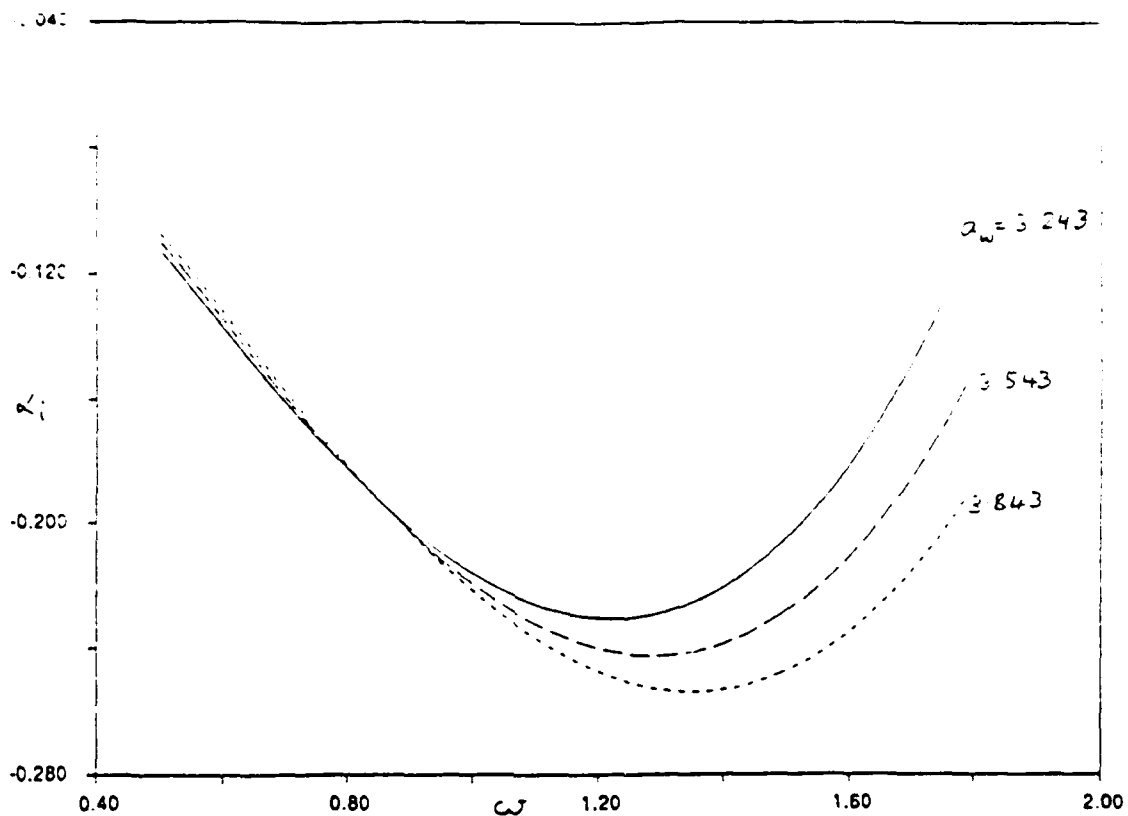


Figure 13: Variation of growth rates with change in wake-width in a boundary layer with $u_w = 0.5$, $y_w = 2.4$

5.4.2. Wake Width

For a fixed u_w and y_w , as the wake width parameter a_w is increased from 0.7 to 3.8, that is, as the wake becomes more slender, the growth rates increase for higher frequencies (Figure 13). This is because of the presence of steeper velocity gradients U_y in the flow, which results in a larger positive μ_1 in the vicinity of the wake. This means there is a net transfer of energy from the mean flow to the disturbance.

5.4.3. Wake Height in the Boundary Layer

For a fixed u_w and a_w , as the wake centerline location y_w is decreased from 6.0 to 2.4, the growth rates increase for lower frequencies, decrease for higher frequencies and so the most unstable frequency decreases (Figure 14). Now, as the wake

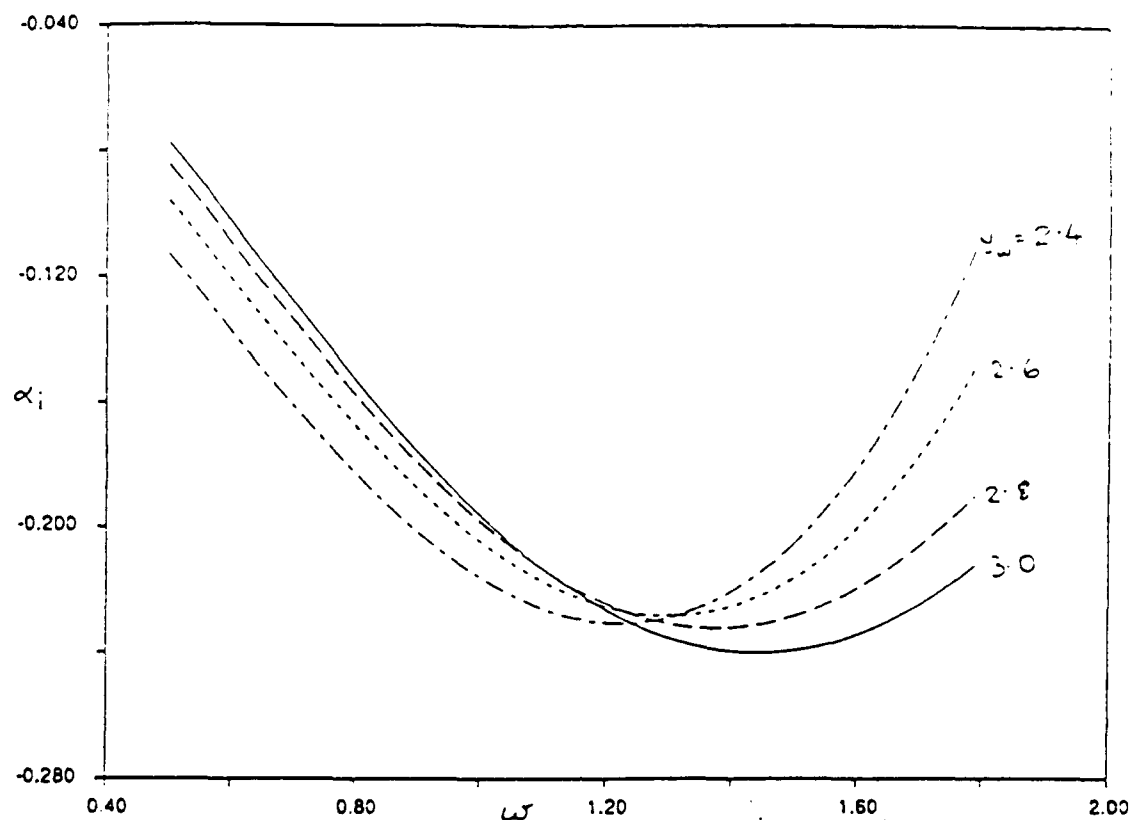


Figure 14: Variation of growth rates with change in wake-height in a boundary layer with $u_w = 0.5$, $a_w = 3.243$

approaches the wall, the “effective” wake defect decreases for a fixed u_w , since the local mean velocity for the boundary layer is lower near the wall. So the inflectional instability decreases.

5.4.4. Viscous Effects

A comparison of the inviscid Rayleigh equation solutions with the solutions to the Orr-Sommerfeld equation, we find that the addition of the viscous terms does not significantly affect the stability characteristics of the wake. This means that the dominant mechanism of instability is the inviscid mechanism due to the inflectional wake profile. The details of the boundary layer profile near the wall do not seem to affect the stability calculations. Thus, we can simply put the wake in any shear profile, such as the hyperbolic tangent profile, having the same slope at the wake

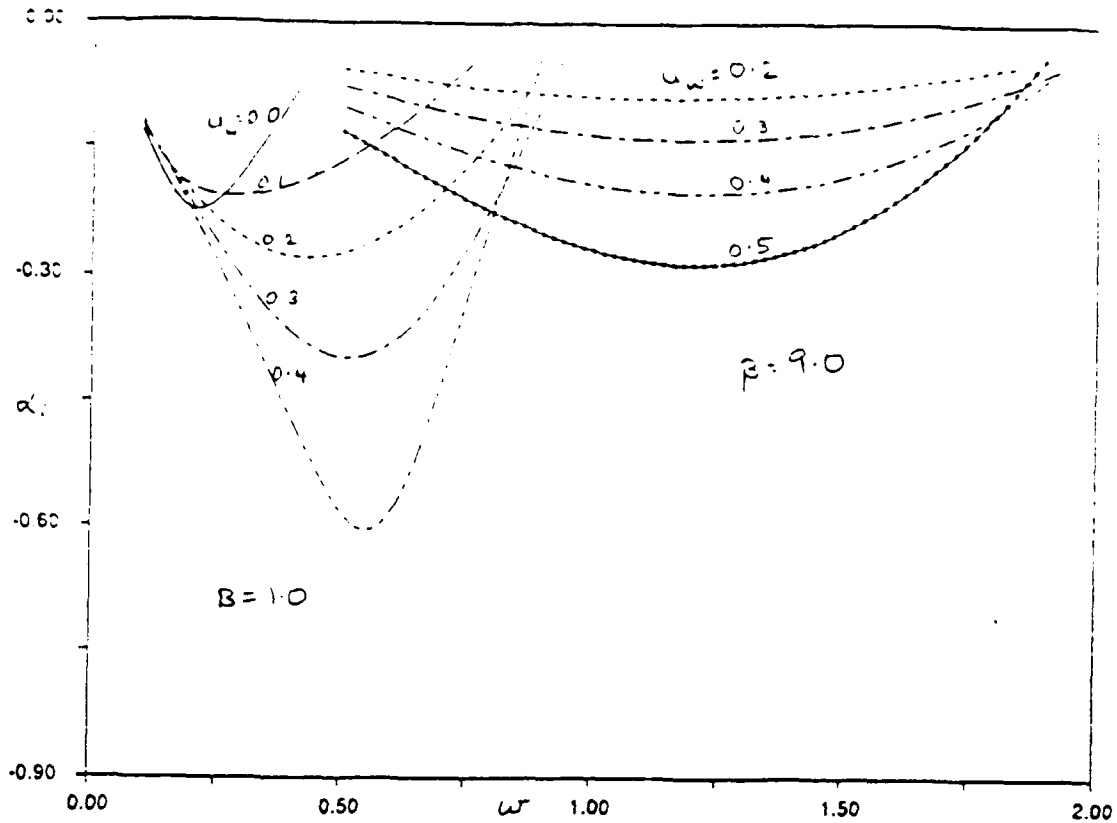


Figure 15: Variation of growth rates with change in wake-velocity defect in a hyperbolic tangent shear layer with $a_w = 3.243$ and $\beta = 1.0$ and 9.0

centerline as the boundary layer profile. We consider the basic flow to be

$$U(y) = \frac{1}{1+\beta}(\beta + \tanh(y)) - u_w \exp(-a_w(y)^2) \quad (60)$$

Here the parameter y_w for the location of the wake centerline is effectively replaced by the parameter β for the slope of the shear profile at the wake centerline. This has the added advantage of giving, in the two limits of β and u_w , the profiles studied by Michalke (1965) ($\beta = 1.0, u_w = 0.0$) and by Sato and Kuriki (1961) (large β , and $u_w = 0.5$). Figure 15 shows the spatial growth rates for the wake in a shear layer profile with a wake width parameter $a_w = 3.243$ and varying β and u_w .

5.5. Future Work

The problem of the stability of a wake in a shear flow can be solved analytically using a perturbation technique. The mean flow is regarded as a perturbation series in the shear parameter, that is, the shear flow is treated as a first-order correction to the basic wake flow. The eigenvalue (wavenumber) is also expanded in a perturbation series. When these expansions are substituted into the two-dimensional, inviscid equations of motion, we recover the Rayleigh equation for the unperturbed wake flow as the zeroth-order equation. The first-order equation is a non-homogeneous, self-adjoint equation with the same linear operator as the Rayleigh equation. This can be solved, using the solvability condition, to obtain a first-order correction to the eigenvalue due to the presence of shear. In the two-dimensional case, the results may be compared with the direct numerical calculations reported above. This technique may then be extended to the three-dimensional problem for a spherical wake in a two-dimensional boundary layer.

Barston(1991) has derived criteria for the instability of plane parallel profiles with multiple inflection points, which are an extensions of the Rayleigh and Fjørtoft criteria. Hence we can analytically examine the stability of a wake in a shear flow by looking at the relative positions of its two inflection points in a given profile.

5.6. Conclusions

The stability characteristics of a wake in a boundary layer have been determined as the wake approaches a wall. These calculations help provide some insight into the effect of particle-generated wakes in laminar boundary layers. The results of our present calculations will be compared with ongoing experiments to verify when a linear or weakly nonlinear stability analysis may be used to describe such wake flows.

6. References

Barston, E. M. (1991) On the linear stability of inviscid incompressible plane parallel flow , *J. Fluid Mechanics*, **233**, p. 157.

Breuer, K., Haritonidis, J., (1990) The evolution of a localized disturbance in a laminar boundary layer. Part I - Weak disturbances. *J. Fluid Mechanics* **220**, p. 569.

Clift, R., Grace, J., Weber, M., (1978) *Bubbles, Drops and Particles*, Academic Press.

Chomaz, J. M., Huerre, P., Redekopp, L. G. (1988) Bifurcations to local and global modes in spatially developing flows. *Phys. Rev. Lett.* **60**, p. 25.

Dandy, D., Dwyer, H., (1990) A sphere in a shear flow at finite Reynolds number: effect of shear on particle lift, drag and heat transfer. *J. Fluid Mechanics* **216**, p. 381.

Gaster, M., (1975) A theoretical model of a wave packet in the boundary layer of a flat plate. *Proc. Roy. Soc. Lond.* **A347**, p. 271.

Gaster, M., Grant, I., (1975) An experimental investigation of the formation and development of a wave packet in a laminar boundary layer. *Proc. Roy. Soc. Lond.* **A347**, p. 253.

Hall, G. R. (1967) Interaction of the wake from bluff bodies with an initially laminar boundary layer. *AIAA Journal* **5**(8), p. 1386.

Gustavsson, L., (1979) Initial value problem for boundary layer flows. *Physics of Fluids* **22**(9), p. 1602.

Henningson, D., (1988) The inviscid initial value problem for a piecewise linear mean flow. *Studies in Applied Math.* **78**, p. 31.

Hoffman, G., (1988) The trajectory of a gas bubble in an axisymmetric turbulent boundary layer. *Technical Memorandum 88-136*, Applied Research Laboratory, Pennsylvania State University.

Huerre, P., Monkewitz, P. A. (1985) Absolute and convective instabilities in free shear layers. *J. Fluid Mechanics* **159**, p. 151.

Huerre, P., Monkewitz, P. A. (1988) The absolute and convective nature of instability in two-dimensional wakes at low Reynolds numbers. *Physics of Fluids* **31**(5), p. 999.

Mattingly, G., Criminale, W. (1972) The stability of an incompressible two-dimensional wake. *J. Fluid Mechanics* **51**, p. 233.

McKoen, C. H. (1956) On the stability of a laminar wake. *Aero. Res. Coun Lond. Rep. no. 303*.

Michalke, A. (1965) On spatially growing disturbances in an inviscid shear layer. *J. Fluid Mechanics* **23**, p. 521.

Press, W., Flannery, B., Teukolsky, S., Vetterling, W. (1986) *Numerical Recipes*. Cambridge University Press.

Saffman, P., (1965) The lift on a small sphere in a slow shear flow. *J. Fluid Mechanics* **22**, p. 385.

Sakamoto, H., Haniu, H., (1990) A study on vortex shedding from spheres in a uniform flow. *Trans. of ASME - J. Fluids Engineering* **112**, p. 386.

Sato, H., Kuriki, K. (1961) The mechanism of transition in the wake of a thin flat plate placed parallel to a uniform flow. *J. Fluid Mechanics* **11**, p. 321.

Tso, J., Chang, S., Blackwelder, R., (1990) On the breakdown of a wave packet disturbance in a laminar boundary layer. submitted for publication.

Van Dyke, M., (1975) *Perturbation Methods in Fluid Mechanics*. Parabolic Press.